UNIVERSITÀ DEGLI STUDI DI PARMA

Dottorato di Ricerca in Tecnologie dell'Informazione

XXVIII Ciclo

Adaptive Signal Processing for Power Line Communications

Coordinatore:

Chiar.mo Prof. Marco Locatelli

Tutor:

Chiar.mo Prof. Riccardo Raheli

Dottorando: *Carlo Tripodi*

Gennaio 2016

Ai miei genitori Giancarlo e Clara

Contents

List of Acronyms

AWGN Additive White Gaussian Noise
ADC Analog-to-Digital Converter
BER Bit Error Rate
FEXT Far End CROSS-Talk
DAC Digital-to-Analog Converter
DFT Discrete Fourier Transform
DSP Digital Signal Processor
DVB-S2 Digital Video Broadcasting - Second Generation
FIR Finite Impulse Response
IDFT Inverse Discrete Fourier Transform
ISI Inter-Symbol Interference
LDPC Low Density Parity Check
LMS Least Mean Square
MLC Multi-Level Coding
MSB Most Significant Bit
MSE Mean Square Error
NEXT Near End CROSS-Talk
NLMS Normalized Least Mean Square
OFDM Orthogonally Frequency Division Multiplexing
PDF Probability Density Function
PLC Power Line Communications
QAM Quadrature Amplitude Modulation

SER Symbol Error Rate

SNR Signal-to-Noise Ratio

VSLMS Variable Step Least Mean Square

WiMAX Worldwide Interoperability for Microwave Access

WRL Weight Reset LMS

WRVSL Weight Reset VSLMS

Introduction

This thesis represents a significant part of the research activity conducted during the PhD program in Information Technologies, supported by Selta S.p.A, Cadeo, Italy, focused on the analysis and design of a Power Line Communications (PLC) system [1].

In recent times the PLC technologies have been considered for integration in Smart Grids architectures [2], as they are used to exploit the existing power line infrastructure for information transmission purposes [3] on low, medium and high voltage lines. The characterization of a reliable PLC system is a current object of research as well as it is the design of modems for communications over the power lines. In this thesis, the focus is on the analysis of a full-duplex PLC modem for communication over high-voltage lines, and, in particular, on the design of the echo canceller device and innovative channel coding schemes.

The first part of this thesis investigates the cancellation of the echo that occurs when, in a full-duplex communication system, the same bandwidth is used for bidirectional connection. As a consequence, the transmitted signal is reverberated through the physical environment and results in time-delayed, distorted, and attenuated images, which interfere with the desired received signal.

In Chapter 1, the general model of a full-duplex communication system, with particular attention to the echo canceller device, is described. Also, as the PLC environment is characterized by an interference which exhibits an impulsive nature, a review of the model of this interference is provided.

The echo canceller filter, which thanks to its capability of self adjustment is a good solution for the echo channel response identification, is described in Chapter 2, where adaptive algorithms for the update of the echo canceller filter are described. A performance analysis is provided for a singlecarrier PLC system. In Chapter 3, the analysis is extended to a multicarrier PLC system, suitable for the communication over frequency-selective and impulsive event-affected PLC channel.

The implementation of the adaptive algorithm in the modem Digital Signal Processor (DSP) requires a fixed-point implementation. In Chapter 4, the fixed-point implementation of a Finite Impulse Response (FIR) filter is discussed and possible causes of errors, due to a poor representation accuracy, which arise during the adaptive filter weight update, are described. A performance analysis is carried on for both the singlecarrier and multicarrier systems.

The PLC environment is typically affected by occasional (but not rare) abrupt channel variations, due to line impedance mismatches, related, for example, to the periodic maintenance operations on the power lines. The speed of the echo canceller adaptation to the new echo channel affects the communication system reliability, so that in Chapter 5 we investigate the beahavior of the adaptive algorithm in the presence of abrupt channel variations and propose a modification of the classical adaptive algorithm for echo cancellation, which allows a fast recovery from an abrupt variation of the channel conditions.

The second part of this thesis investigates channel coding schemes based on the use of Low Density Parity Check (LDPC) codes, for possible implementation in a PLC modem. As we take into account a constraint on the overall encoding and decoding latency, we are interested in evaluating the performance of LDPC codes with low latency, hence with short codeword length. For this reason, we use the LDPC codes adopted in IEEE 802.16e standard (WiMAX), which support short codewords. Their structure is defined on the use of the so-called exponent matrix to specify the code parity check matrix, so that this class of LDPC codes allows limited memory consumption for the storage of the parity check matrix in the DSP. In Chapter 6, the structure of the WiMAX LDPC codes is reviewed, different coding schemes are proposed and their performance, also in the PLC scenario, is analyzed.

Part I

Echo Cancellation in a PLC Modem

Chapter 1

PLC System Model

1.1 Introduction

In this chapter, we present the general model of a digital full-duplex Power Line Communication (PLC) system [1] . Particular attention is given to the echo canceller filter and realistic features of the analyzed scenario, such as attenuations acting over the system and the field measure of the echo response, are introduced. In order to characterize the PLC environment, we consider the presence of impulse noise, which affects the physical communication channel. In particular, we consider the "bursty impulse noise" model for a better characterization of the bursty nature of the impulsive events.

The structure of this chapter is the following. In Section 1.2, the general echo cancellation method of full-duplex transmission and the specific system model needed to investigate the echo canceller are presented. In Section 1.3 the bursty impulse noise model is reviewed.

1.2 General System Model

The general system model is shown in Figure 1.1. The transmission blocks, named Tx1 and Tx2, model the generation, modulation and interpolation

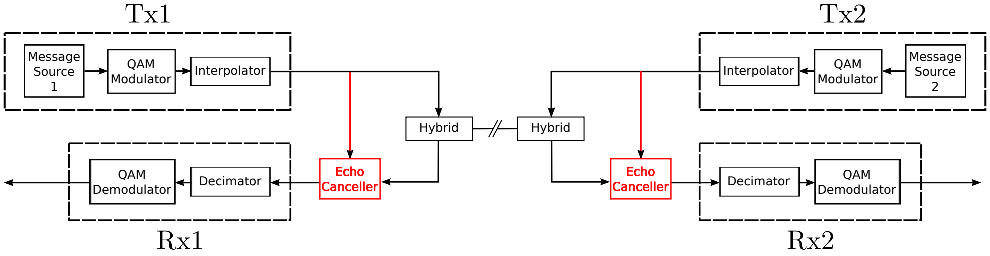

Figure 1.1: General system model.

of the transmitted signals. For both transmitters, the binary information sequence is generated at a bit rate equal to r_b. The binary information sequence can be associated with a sequence of symbols belonging to M-ary alphabet and generated at a rate equal to $f_{symb} = r_b / \log_2 M$. The information sequence is then modulated by means of a Quadrature Amplitude Modulation (QAM) format with constellation size M. Note that an uncoded symbol of an M-ary modulation is associated with a spectral efficiency equal to $b = \log_2 M$ bits per channel use (or b/s/Hz relative to a bandwidth equal to the signaling frequency).

The modulated sequence is in a one-to-one correspondence with the transmitted sequence. The interpolator block performs upsampling of the modulated sequence by a factor N_u, with a corresponding sampling frequency $f_s = N_u f_{symb}$, possibly by means of polyphase implementation of the transmitter filter [4, 5] with square-root raised-cosine Fourier transform, specified by the continuous-time impulse response:

$$p(t) = 4\beta \frac{\cos\left[(1+\beta)\pi\frac{t}{T}\right] + \frac{\sin\left[(1-\beta)\pi\frac{t}{T}\right]}{4\beta\frac{t}{T}}}{\pi\sqrt{T}\left[1-\left(4\beta\frac{t}{T}\right)^2\right]}$$

where the symbol interval T is equal to $1/f_{symb}$ and β is the roll-off factor, with $0 \leq \beta \leq 1$. Note that these filters are optimal in the sense that they guarantee the absence of Inter-Symbol Interference (ISI) at proper sampling intervals for transmissions over frequency-flat channels [6]. The receiver blocks, called Rx1 and Rx2, perform the decimation and the demodulation of the received signals. The decimator performs receiver filtering and downsampling of the signal by the factor N_u. As for the interpolator, a polyphase implementation of the decimator can be adopted as well. The choice of this kind of implementation for the interpolator and decimator is related to the complexity reduction with respect to a classical implementation [4], since the filtering operations can be performed at a rate f_{symb} rather than at f_s.

The communication in the system depicted in Figure 1.1 is full-duplex: two different communication acts take place simultaneously on the same channel bandwidth. In particular, the signal transmitted by Tx1 is received by Rx2 and the one transmitted by Tx2 is received by Rx1. The communication in both directions is allowed by a coupling device called “hybrid coupler” [7, 8, 9], or simply hybrid, at the link ends. This device is responsible of the Near-end crosstalk (NEXT), since for physical reasons it allows a transmitted signal to appear at the input of the receiver dedicated to the other communication path, e.g., the signal transmitted by Tx1 interferes with the signal transmitted from Tx2 and directed to Rx1. Far-end crosstalk (FEXT), also results because of line impedance mismatches and from the hybrid of the remote terminal. These effects can be modeled by means of an echo channel which generates an interfering signal.

The echo canceller is necessary to reduce, or, in particular conditions, to eliminate, the echo. The general echo canceller scheme is depicted in Figure 1.2. The adaptive filter algorithmically adapts its parameters in order to minimize a function of the difference between the desired output and its actual output (the cost function of the algorithm). The difference between the desired signal and the adaptive filter output is the error signal, that is fed back to the adaptive filter, whose coefficients are changed adaptively in order to minimize a function of this difference. In the case of echo cancellation, the optimal output of the adaptive filter is equal to the unwanted echoed signal, i.e., the impulse response of the adaptive filter is the same as the echo channel one. When the adaptive filter output is equal to the desired signal the error signal reduces to zero. In

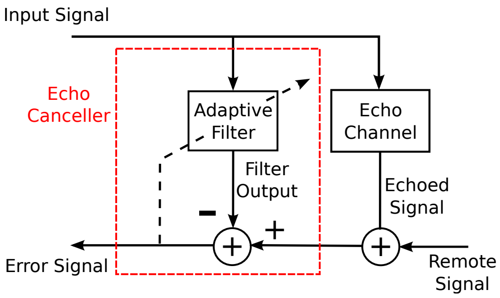

Figure 1.2: Echo canceller scheme.

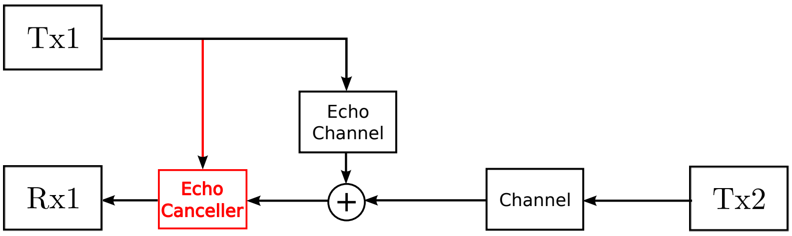

Figure 1.3: System model.

Chapter 2 the adaptive filter and its update algorithm are described.

1.2.1 Signal Dynamics and Echo Channel Impulse Response

Since we are interested in the echo canceller analysis and design of its algorithm, the system model of Figure 1.1 can be simplified considering just one communication path and the echoed interfering signal, obtaining the system model shown in Figure 1.3. The channel block represents the physical communication channel. The echo channel represents the crosstalk from the transmitter Tx1.

Considering that the transmission power is the same for both transmitters, it is clear that the received power of the intended signal is lower than that of the interfering signal, since the former passes through the physical communication channel while the latter does not. This power difference between the two signals cannot be neglected, as it can be foresaw that the quality of the filter adaptation depends also on the power of the signal at the input of the adaptive filter. Intuitively, if the signal power transmitted by Tx1 and the echoed signal power as well, are higher than that of the intended signal (transmitted by Tx2) at the receiver, it will be easier to recognize the echo channel response, since the adaptive filter will sense the intended signal as a “small disturbance” in the recognizing process.

Referring to Figure 1.4, the indicated numbers 1 to 5 correspond to the following realistic values of the transmission power and attenuation coefficient at the various blocks can be, for example, considered:

1. the transmit power is 40.5 dBm,
2. the overall attenuation, at the remote transmitter, is 0.5 dB,
3. the line loss is 40 dB, so that the desired signal power at the link end, before the echo canceller, is 0 dBm,
4. the hybrid loss is 21 dB, so that the desired signal power available at the echo canceller is -21 dBm,
5. the hybrid attenuates the local echo by 8 dB, that is summed to its loss of 21 dB: the local echo power is then $40.5 - (21 + 8) = 11.5$ dBm.

This means that the local echo power is about 32.5 dB over the desired signal. This can be modeled simply considering the normalization of the transmission power to 0 dBW, introducing a gain of 32.5 dB in the interfering transmission path and neglecting the physical channel attenuation, as shown in Figure 1.5.

A realistic impulse response, measured on a 110 km high-voltage power line at 380 kV, has been provided by Selta in order to make the investigation more accurate. Figure 1.6 shows the field measurement of the passband echo channel impulse response; the sampling frequency is ν_s, the carrier frequency is ν_c and the energy is normalized to 1. The impulse length, in terms of samples at ν_s, is set to $N = 1000$.

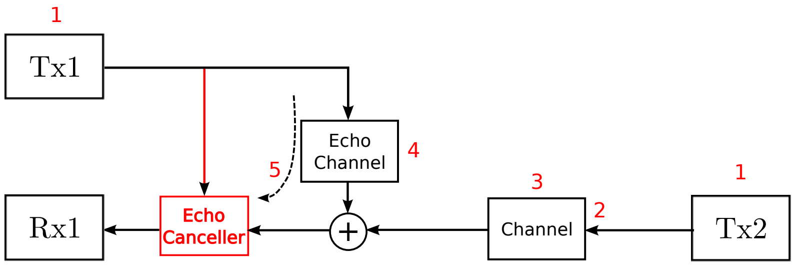

Figure 1.4: System model: transmit power and attenuation.

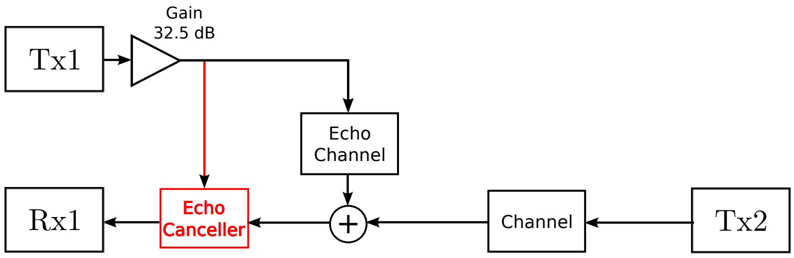

Figure 1.5: System model with normalized transmit power and channel attenuation and gain on the local transmit signal.

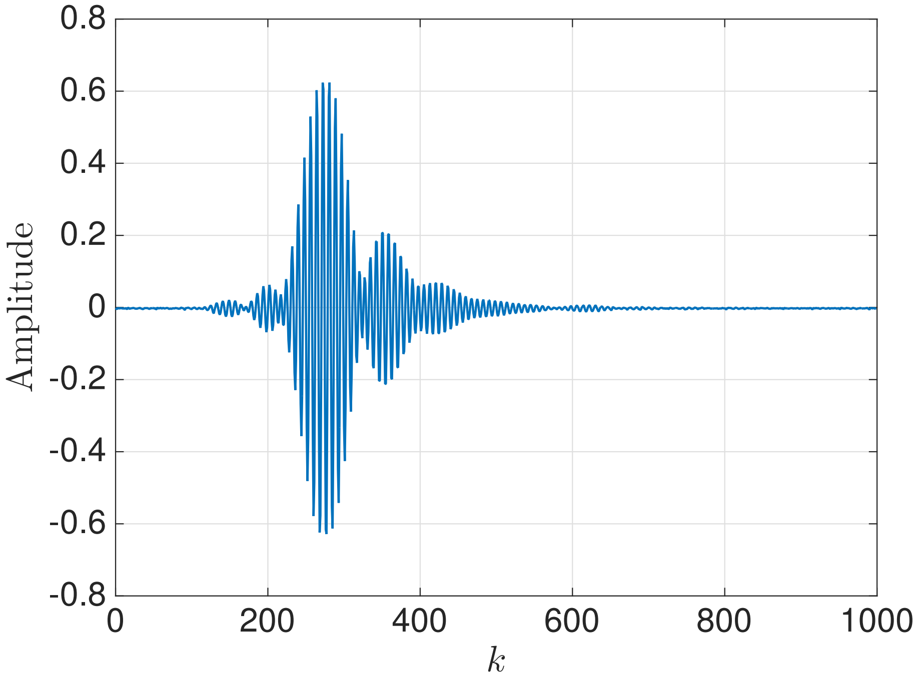

Figure 1.6: Passband echo channel impulse response.

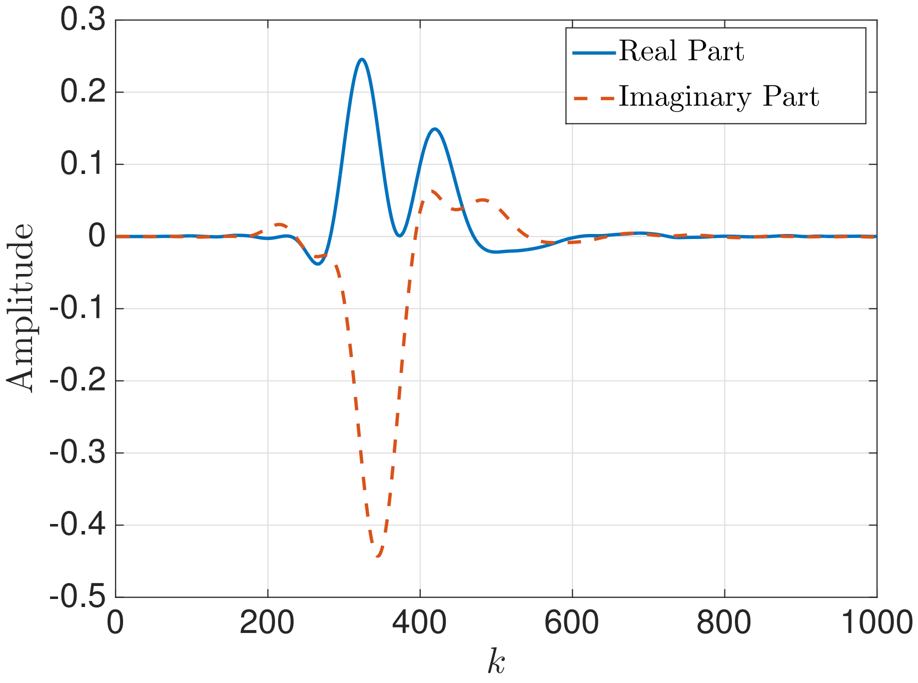

Figure 1.7: Baseband equivalent of echo channel impulse response.

Passband echo cancellation is considerably different from the baseband channel case and it is more complex, as explained in [9]. For this reason, the echo cancellation here investigated is performed in the case of baseband echo channel.

Denoting as $\{h_k^{PB}\}_{k=0}^{N-1}$ the passband echo response sampled at ν_s and as $\{h_k\}_{k=0}^{N-1}$ its baseband complex version, the element-by-element conversion can be obtained as follows [6] (neglecting the lowpass filtering operation):

$$h_k = h_k^{PB}\sqrt{2}e^{-j2\pi\frac{\nu_c}{\nu_s}k}.$$

The resulting complex-valued baseband echo response is shown in Figure 1.7.

1.3 Bursty Impulse Noise Model

A typical PLC environment interference is the impulse noise, which of course exhibits an impulsive nature [10, 11, 12]. Classical impulse noise models are the Bernoulli-Gaussian model [11] and the Class-A model [13]. These models are memoryless, i.e., they do not consider the bursty nature of this interference. However, the impulsive events duration is not negligible compared with the symbol interval. For a better characterization of the impulse noise process, the bursty impulse noise model can be adopted [10, 14].

Such a model is a modification of the Bernoulli-Gaussian model, which considers two channel states, the good and the bad state, characterized by a Bernoulli process. A two-state Markov process can be used in order to describe the bursty evolution of the channel state [15].

At each instant k, the impulse noise samples i_k are statistically specified by the channel state $s_k \in \{G, B\}$, where G stands for the good channel and B for the bad one. The noise samples i_k are assumed to be Gaussian random variables with zero mean and variance depending on s_k. Denoting by σ_G^2 and σ_B^2 the variance in the good and bad state respectively, the probability density functions of i_k, conditioned on s_k, are

$$\begin{aligned} p(i_k|s_k = G) &= \frac{1}{2\pi\sigma_G^2} e^{-\dfrac{|i_k|^2}{2\sigma_G^2}} \\ p(i_k|s_k = B) &= \frac{1}{2\pi\sigma_B^2} e^{-\dfrac{|i_k|^2}{2\sigma_B^2}}. \end{aligned}$$

Denoting by R the ratio between the variances in the bad and good states, one has

$$\sigma_B^2 = R\sigma_G^2. \tag{1.1}$$

Note that for $R = 1$ the impulse noise process becomes AWGN with variance σ_G^2 and the two states coincide.

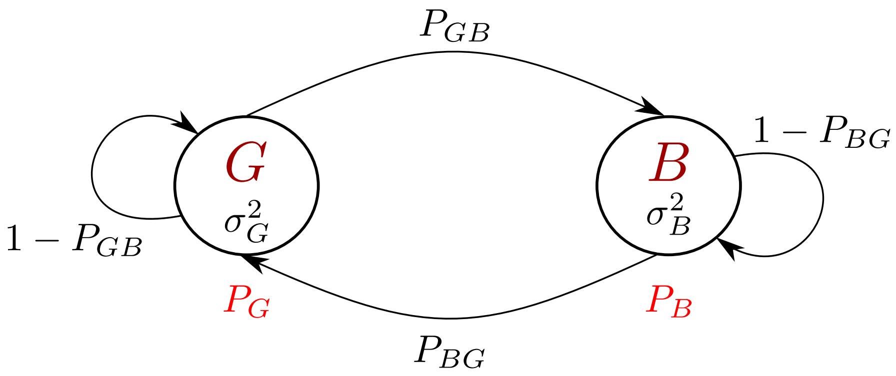

Figure 1.8: Channel states diagrams.

Figure 1.8 shows the channel state diagram, where the state probability is denoted as

$$P_J = P(s_k = J), \quad J \in \{G, B\}$$

and the transition probability is denoted as

$$P_{IJ} = P(s_{k+1} = J | s_k = I), \quad I, J \in \{G, B\}.$$

The state process S with realizations $\{s_k\}$ is then described by a stationary first-order Markov process [16], characterized by the multivariate mass probability

$$P(s_0^n) = P(s_0) \prod_{k=1}^{n} P(s_{k+1} | s_k)$$

where $s_0^n = (s_0, ..., s_n)$.

The probability of being in a given state can be obtained considering [16]

$$\begin{cases} P_G + P_B = 1 \\ P_G P_{GB} = P_B P_{BG} \end{cases}$$

where the second is the ‘balance equation” [16] for this case. Therefore, one obtains:

$$\begin{aligned} P_G &= \frac{P_{BG}}{P_{GB}+P_{BG}} && (1.2)\\ P_B &= \frac{P_{GB}}{P_{GB}+P_{BG}}. && (1.3)\end{aligned}$$

The average persistence in a given state T_J with $J \in \{G, B\}$, i.e., the average number of consecutive time indices of persistence in the state J [16], in terms of samples is

$$\begin{aligned} T_G &= \frac{1}{P_{GB}} && (1.4)\\ T_B &= \frac{1}{P_{BG}}. && (1.5)\end{aligned}$$

The channel memory can be quantified by the parameter

$$\gamma = \frac{1}{P_{GB}+P_{BG}} \tag{1.6}$$

which represents the ratio between the actual value of T_J and the value of T_J in the case of a memoryless channel [10], which may be denoted as T'_J, where the prime symbol is used to differentiate the notation from that of the original channel. In fact, for a memoryless channel, one has $P'_{GB} = P_B$ and $T'_G = 1/P_B$, so that

$$\begin{aligned} \frac{T_G}{T'_G} &= \frac{1}{P_{GB}} P'_{GB}\\ &= \frac{1}{P_{GB}} P_B\\ &= \frac{1}{P_{GB}} \frac{P_{GB}}{P_{GB}+P_{BG}}\\ &= \gamma.\end{aligned}$$

Similarly, one may find that $T_B/T'_B = \gamma$. Intuitively, the larger γ, the larger the persistence in a given state as the transition probabilities decrease. For $\gamma = 1$, $P_{GB} = P_B = P'_{GB}$ and a memoryless channel is obtained.

The bursty impulse noise process can be then completely defined by the pair (P_B, γ), that is in a one-to-one correspondence with the pair (P_{GB}, P_{BG}).

Figure 1.9 shows the magnitude of the noise samples for $\sigma_G^2 = 1$, $R = 100$, $P_B = 0.1$, and various values of γ, as obtained by simulation. One can note that the bursty nature of the impulse event can be described choosing $\gamma > 1$.

Let us now analytically evaluate the variance σ_i^2 of the impulse noise process. The impulse noise samples are not independent and identically distributed, however, each impulse noise sample is conditionally Gaussian with zero mean, and variance depending on the state. The impulse noise process variance σ_i^2 is the weighted average between σ_G^2 and σ_B^2, so that

$$\begin{aligned} \sigma_i^2 &= \sigma_G^2 P_G + \sigma_B^2 P_B \\ &= \sigma_G^2 (P_G + R P_B) \\ &= \sigma_G^2 (1 - P_B + R P_B) \\ &= \sigma_G^2 \left[1 + P_B (R - 1)\right]. \end{aligned} \tag{1.7}$$

One can obtain (1.7) also considering that for the time fraction $\dfrac{T_G}{T_G + T_B}$ the channel state is G while for a fraction $\dfrac{T_B}{T_G + T_B}$ the channel state is B, so that

$$\begin{aligned} \sigma_i^2 &= \frac{T_G}{T_G + T_B} \sigma_G^2 + \frac{T_B}{T_G + T_B} \sigma_B^2 \\ &= \frac{\sigma_G^2 T_G + \sigma_B^2 T_B}{T_G + T_B} \\ &= \sigma_G^2 \left(\frac{T_G}{T_G + T_B} + R \frac{T_B}{T_G + T_B} \right) \\ &= \sigma_G^2 \left(P_G + R P_B \right) \end{aligned}$$

Note that for $P_B = 0$ or $R = 1$ the noise process is independent and identically distributed Gaussian, with variance σ_G^2.

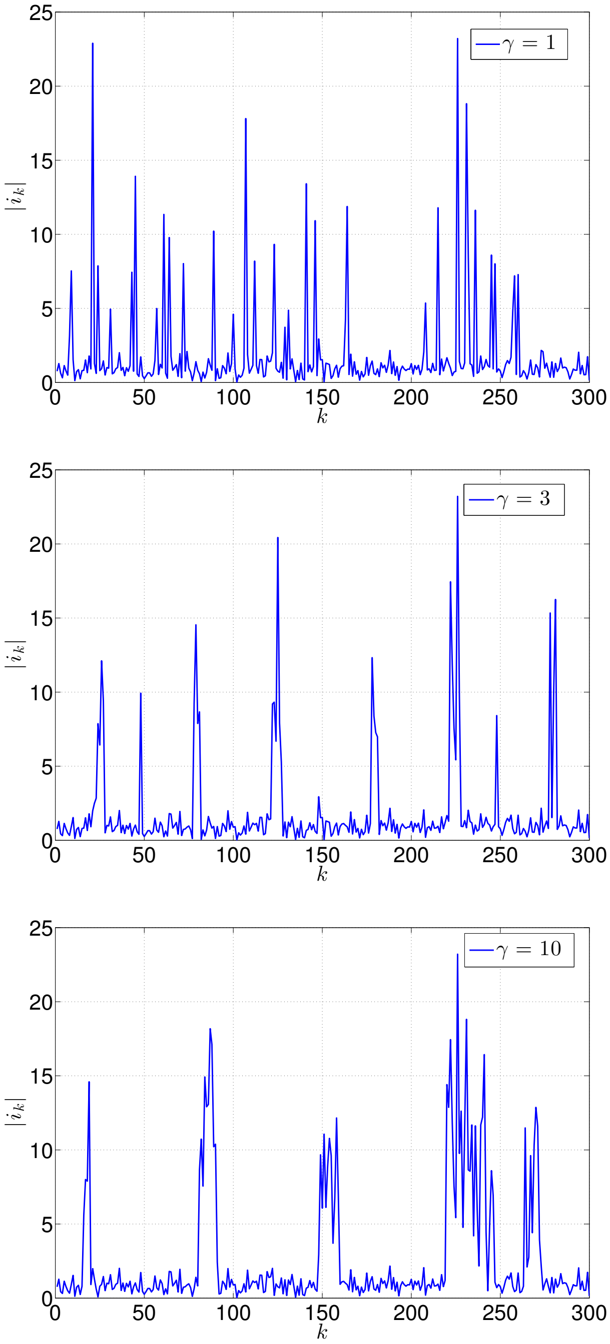

Figure 1.9: Magnitude of the noise samples i_k for $\sigma_G^2 = 1$, $R = 100$, $P_B = 0.1$, and various values of γ.

Chapter 2

Echo Cancellation

2.1 Introduction

A widely used adaptive algorithm for echo cancellation is the Least Mean Square (LMS) algorithm: a stochastic gradient-based algorithm [17, 18, 19, 20, 21, 22] for the update of the Finite Impulse Response (FIR) filter tap weights. Its popularity is due to its simplicity, robustness and low computational complexity. Many variants of the original LMS algorithm have been investigated in the literature and are suitable for different scenarios, see e.g. [23, 24, 25].

The basic idea of the LMS algorithm is to use the gradient vector of the Mean Square Error (MSE) between the input and output of the filter with respect to the FIR filter tap weights to converge to the optimal solution updating the weights by a steepest descent algorithm. If a specific component of the MSE gradient is positive, the error can be reduced by reducing the corresponding weight. The MSE, as we will see, is a quadratic function of the filter weight vector, so that it presents a unique minimum, which is the optimal weight solution.

The structure of this chapter is the following. In Section 2.2, the LMS algorithm for echo cancellation is discussed and its normalized version is presented.

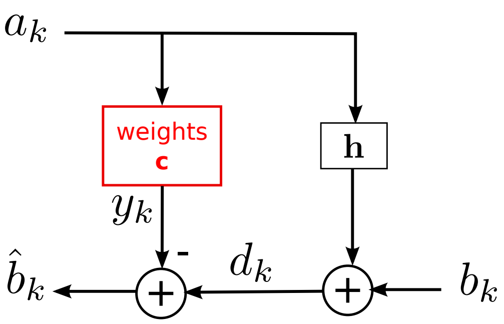

Figure 2.1: Echo canceller scheme.

In Section 2.3, the algorithm is derived, starting from the continuous-time model of a full-duplex communication system. In Section 2.4, the algorithm formulation in discrete time is discussed. In Section 2.5, simulation results are given. Section 2.7 is dedicated to final remarks.

2.2 LMS Algorithm for Echo Cancellation

We now review the LMS algorithm for symbol time echo cancellation, i.e., the case where the transmitted sequence is sampled at f_{symb}.

Consider the scheme shown in Figure 2.1, that describes the system shown in Figure 1.5 and where the gain block has been incorporated in the weight vector and the physical transmission channel has been considered ideal. Sequences $\{a_k\}$ and $\{b_k\}$ of modulated, complex symbols are transmitted simultaneously from Tx1 and Tx2, respectively. The echo channel response is denoted by $\mathbf{h} = (h_0, h_1, ..., h_{N-1})^\mathsf{T}$, where h_k are the symbol-time samples of the echo channel impulse response, represented by N samples, and $()^\mathsf{T}$ denotes the transpose operator. The adaptive filter weights are denoted by the vector $\mathbf{c} = (c_0, c_1, ..., c_{N-1})^\mathsf{T}$, whose length is set to N, as it will be clarified later. The input of the adaptive filter can be denoted in terms of the vector $\mathbf{a}_k = (a_k, a_{k-1,} ..., a_{k-N+1})^\mathsf{T}$. The signal $\{d_k\}$ consists of an echoed version of $\{a_k\}$ plus the desired signal $\{b_k\}$, i.e. $d_k = \mathbf{h}^\mathsf{T}\mathbf{a}_k + b_k$. The received sequence

$\{\hat{b}_k\}$ is equal to the transmitted $\{b_k\}$ if and only if the echo is totally cancelled, i.e., if the output of the adaptive filter $\{y_k\}$ is equal to the echo $\mathbf{h}^{\mathsf{T}}\mathbf{a}_k$. Since the filter output is $y_k = \mathbf{c}^{\mathsf{T}}\mathbf{a}_k$, it is equal to the echo if and only if $\mathbf{c} = \mathbf{h}$, i.e. if the adaptive filter reproduces exactly the echo channel response.

It is worth noting that, if the length of the adaptive filter is the same as the echo channel impulse response, one can have $\mathbf{c} = \mathbf{h}$. The echo can be cancelled also if the filter length is larger than that of the echo (although the processing duration increases). However, the opposite is not always true, since it depends on the echo impulse response shape and characteristics. For these reasons, one can assume that $\mathbf{c}$ and $\mathbf{h}$ have the same length (in terms of N samples).

In the literature, the cost function to be minimized by the LMS algorithm for echo cancellation is usually indicated as the MSE between the sequences $\{d_k\}$ and $\{y_k\}$ [23, 26], but we prefer the equivalent[1] and more intuitive formulation of the MSE that considers the difference between the transmitted intended signal and the received one, so that the MSE as a function of the filter weights is defined as

$$\begin{aligned}\mathcal{E}(\mathbf{c}) &= \mathbb{E}\{|\hat{b}_k - b_k|^2\} \\ &= \mathbb{E}\{\hat{b}_k\hat{b}_k^*\} + \mathbb{E}\{b_k b_k^*\} - 2\mathrm{Re}\left[\mathbb{E}\{b_k\hat{b}_k^*\}\right]. \end{aligned} \tag{2.1}$$

Since the transmitted symbols can be assumed identically distributed and zero mean, one has

$$\mathbb{E}\{b_k b_k^*\} = \mathbb{E}\{|b_k|^2\} = \sigma_b^2$$

which is the variance of symbols b_k. Note that, since the transmission power is normalized to 0 dBW as specified in Section 1.2.1, $\sigma_b^2 = 1$.

The other terms in (2.1) can be expanded as

$$\begin{aligned}\mathbb{E}\{b_k\hat{b}_k^*\} &= \mathbb{E}\{b_k d_k^*\} - \mathbb{E}\{b_k y_k^*\} \\ &= \mathbb{E}\{b_k d_k^*\} - \mathbb{E}\{b_k \mathbf{c}^H \mathbf{a}_k^*\}\end{aligned}$$

---

[1] It is later shown that both formulations of the MSE lead to similar cost functions and the same weight update algorithm.

where we used $\hat{b}_k = d_k - y_k$ and $()^H$ denotes the conjugate transpose (hermitian transpose) operator, and

$$\begin{aligned}\mathbb{E}\{\hat{b}_k\hat{b}_k^*\} &= \mathbb{E}\{|d_k|^2\} + \mathbb{E}\{|y_k|^2\} - 2\mathrm{Re}\left[\mathbb{E}\{d_k y_k^*\}\right] \\ &= \mathbb{E}\{|d_k|^2\} + \mathbb{E}\{\mathbf{c}^H\mathbf{a}_k^*\mathbf{a}_k^\intercal\mathbf{c}\} - 2\mathrm{Re}\left[\mathbb{E}\{d_k\mathbf{c}^H\mathbf{a}_k^*\}\right] \\ &= \mathbb{E}\{|d_k|^2\} + \mathbf{c}^H\mathbf{A}\mathbf{c} - 2\mathrm{Re}\left[\mathbf{c}^H\mathbf{t}\right] \qquad (2.2)\end{aligned}$$

in which we have defined the correlation matrix of the sequence $\{a_k\}$ as $\mathbf{A} = \mathbb{E}\{\mathbf{a}_k^*\mathbf{a}_k^\intercal\}$ and the vector

$$\begin{aligned}\mathbf{t} &= \mathbb{E}\{d_k\mathbf{a}_k^*\} \\ &= \mathbb{E}\{\mathbf{a}_k^*\mathbf{a}_k^\intercal\}\mathbf{h} + \mathbb{E}\{b_k\mathbf{a}_k^*\} \\ &= \mathbf{A}\mathbf{h}\end{aligned}$$

where we used the independence between b_k and a_k, so that $\mathbb{E}\{b_k\mathbf{a}_k^*\} = 0$. Note that since a_k are independent and identically distributed (i.i.d.) and zero mean, and $\sigma_a^2 = 1$, $\mathbf{A}$ is a $N \times N$ identity matrix.

Equation (2.1) therefore becomes

$$\begin{aligned}\mathcal{E}(\mathbf{c}) &= \mathbb{E}\{|d_k|^2\} + \mathbf{c}^H\mathbf{A}\mathbf{c} - 2\mathrm{Re}\left[\mathbf{c}^H\mathbf{t}\right] + \sigma_b^2 - 2\mathrm{Re}\left[\mathbb{E}\{b_k d_k^*\} - \mathbf{c}^H\mathbb{E}\{b_k\mathbf{a}_k^*\}\right] \\ &= \mathbb{E}\{|\mathbf{h}^\intercal\mathbf{a}_k + b_k|^2\} + \mathbf{c}^H\mathbf{A}\mathbf{c} - 2\mathrm{Re}\left[\mathbf{c}^H\mathbf{t}\right] + \sigma_b^2 - 2\mathrm{Re}\left[\mathbb{E}\{b_k(\mathbf{h}^\intercal\mathbf{a}_k + b_k)^*\}\right] \\ &= \mathbf{h}^H\mathbf{A}\mathbf{h} + \sigma_b^2 + 2\mathrm{Re}\left[\mathbf{h}^\intercal\mathbb{E}\{\mathbf{a}_k b_k^*\}\right] + \mathbf{c}^H\mathbf{A}\mathbf{c} - 2\mathrm{Re}\left[\mathbf{c}^H\mathbf{t}\right] + \sigma_b^2 - 2\sigma_b^2 \\ &= \mathbf{h}^H\mathbf{A}\mathbf{h} + \mathbf{c}^H\mathbf{A}\mathbf{c} - 2\mathrm{Re}\left[\mathbf{c}^H\mathbf{t}\right] \qquad (2.3)\end{aligned}$$

and its gradient with respect to the complex vector $\mathbf{c}$, as discussed in [27], is

$$\begin{aligned}\nabla_{\mathbf{c}}\mathcal{E}(\mathbf{c}) &= 2\mathbf{A}\mathbf{c} - 2\mathbf{t} \\ &= 2(\mathbf{A}\mathbf{c} - \mathbf{t}). \qquad (2.4)\end{aligned}$$

If the gradient (2.4) is zero, the optimum solution is reached and the optimum weight vector $\mathbf{c}^{opt}$ is

$$\begin{aligned}\mathbf{c}^{opt} &= \mathbf{A}^{-1}\mathbf{t}\\ &= \mathbf{A}^{-1}\mathbf{A}\mathbf{h}\\ &= \mathbf{h}. \end{aligned} \tag{2.5}$$

Equation (2.4) can be written as

$$\begin{aligned}\nabla_{\mathbf{c}}\mathcal{E}(\mathbf{c}) &= 2\mathbb{E}\{\mathbf{a}_k^*\mathbf{a}_k^{\intercal}\mathbf{c} - d_k\mathbf{a}_k^*\}\\ &= 2\mathbb{E}\{\mathbf{a}_k^*(y_k - d_k)\}.\end{aligned}$$

One can think to estimate the gradient, that is an average of stochastic quantities whose realizations are available at the receiver, simply performing a temporal average, therefore the stochastic gradient [18] is

$$\hat{\nabla}_{\mathbf{c}}\mathcal{E}(\mathbf{c}) = 2\mathbf{a}_k^*(y_k - d_k).$$

The stochastic gradient algorithm for weight update is then

$$\begin{aligned}\mathbf{c}_{k+1} &= \mathbf{c}_k - \frac{1}{2}\mu\hat{\nabla}_{\mathbf{c}}\mathcal{E}|_{\mathbf{c}=\mathbf{c}_k} \qquad (2.6)\\ &= \mathbf{c}_k + \mu\mathbf{a}_k^*(d_k - y_k)\end{aligned}$$

where μ is the step size, a proper update constant that plays a key-role in the algorithm stability and efficiency. The larger the step size, the faster the convergence to the optimal solution, but the algorithm stability, i.e. the fluctuation around the optimal solution, is smaller and viceversa. Many studies on the LMS algorithm convergence have been pursued [17, 20, 28], and it has been proved that the convergence is ensured for $0 < \mu < 2/(N\mathbb{E}\{|a_k|^2\})$, but the choice of a good value of μ is linked to the particular application of the algorithm and must be chosen empirically.

For the sake of completeness, one can note that, since $\hat{b}_k = d_k - y_k$, defining the MSE between the sequences $\{d_k\}$ and $\{y_k\}$, leads to (2.2), i.e.

$$\begin{aligned}\mathbb{E}\{|d_k - y_k|^2\} &= \mathbb{E}\{|d_k|^2\} + \mathbf{c}^H\mathbf{A}\mathbf{c} - 2\mathrm{Re}\left[\mathbf{c}^H\mathbf{t}\right] \\ &= \mathbf{h}^H\mathbf{A}\mathbf{h} + \sigma_b^2 + \mathbf{c}^H\mathbf{A}\mathbf{c} - 2\mathrm{Re}\left[\mathbf{c}^H\mathbf{t}\right] \qquad (2.7)\end{aligned}$$

which has the same form as (2.3) except for the term σ_b^2. It is clear that its gradient and, therefore, the optimal solution of (2.7), are identical to (2.4) and (2.5), respectively.

2.2.1 Normalized Least Mean Square Algorithm

Selecting a proper value of a fixed step size parameter for every iteration requires an understanding of the statistics of the input. The Normalized Least Mean Square (NLMS) algorithm [19, 22, 23, 26, 29] is an extension of the LMS algorithm which bypasses this issue by selecting a different step size value for each iteration of the algorithm. This step size is inversely proportional to the Euclidean norm of the signal at the input of the adaptive filter, i.e., $||\mathbf{a}_k||^2 = \mathbf{a}_k^H\mathbf{a}_k$. The weights update formula for the NLMS algorithm is thus

$$\mathbf{c}_{k+1} = \mathbf{c}_k + \mu_k\mathbf{a}_k^*(d_k - y_k) \qquad (2.8)$$

where the normalized step size is

$$\begin{aligned}\mu_k &= \frac{\mu}{p + \mathbf{a}_k^H\mathbf{a}_k} \\ &= \frac{\mu}{p + \sum_{i=0}^{N-1}|a_{k-i}|^2} \qquad (2.9)\end{aligned}$$

in which p is a positive parameter that is introduced to avoid that the denominator becomes too small. In this case, the convergence is guaranteed for $0 < \mu < 2$ [19].

If N is sufficiently large, it can be concluded that

$$\sum_{i=0}^{N-1} |a_{k-i}|^2 \simeq N\mathbb{E}\{|a_k|^2\}$$

so that (2.9) becomes

$$\mu_k \simeq \frac{\mu}{p + N\mathbb{E}\{|a_k|^2\}}$$

and the NLMS reduces to the LMS.

2.2.2 Variable-Step Least Mean Square Algorithm

The Variable-Step size Least Mean Square (VSLMS) algorithm allows the step size μ to be adaptively tuned. If the error signal $d_k - y_k$ is large, the weight vector is adapted faster by increasing the step size up to a certain user-defined value $\mu^{\max}$. If $d_k - y_k$ is small, that is, the MSE has converged to its steady-state value, the adaptation speed is reduced (and the algorithm stability increased consequently), by reducing μ down to a certain user-defined value $\mu^{\min}$.

The VSLMS parameter setting is tricky and strongly depends on the application scenario. The main issue of this algorithm is its instability, related to the fact that a small fluctuation of the error signal may entail a significant variation of the step size, which reflects in an overall instability of the algorithm.

The classical VSLMS weight update recursion is [19]

$$\mathbf{c}_{k+1} = \mathbf{c}_k + \mu_k \mathbf{x}_k^* (d_k - y_k) \tag{2.10}$$

where the time-varying step size update recursion, expressed in its signed version [19, Sect. 14.7.2] is

$$\mu_k = \mu_{k-1}\{1 + \rho[\text{sign}(\text{Re}[\mathbf{g}_k^H \mathbf{g}_{k-1}]) + \text{sign}(\text{Im}[\mathbf{g}_k^H \mathbf{g}_{k-1}])]\} \tag{2.11}$$

in which ρ is a step size parameter for the update of μ, sign$(\cdot)$ denotes the sign function, Re$[\cdot]$ and Im$[\cdot]$ denote the real and imaginary parts, respectively, and $\mathbf{g}_k$ is defined as

$$\mathbf{g}_k = \mathbf{x}_k^*(d_k - y_k).$$

In [19, Sect. 6.5], various modifications of the weight update recursion, with respect to (2.10), are given. The main advantages of the following versions are related to the simplification of the hardware implementation, as well as the improvement in the algorithm stability. The Signed-Regressor version of the weight update recursion is defined as

$$\mathbf{c}_{k+1}^{\mathrm{SR}} = \mathbf{c}_k + \mu_k \mathrm{sign}(\mathbf{x}_k^*)(d_k - y_k) \tag{2.12}$$

where the sign of a complex quantity z is defined as

$$\mathrm{sign}(z) = \mathrm{sign}(\mathrm{Re}[z]) + \jmath\,\mathrm{sign}(\mathrm{Im}[z]).$$

The Sign-Sign version is defined as

$$\mathbf{c}_{k+1}^{\mathrm{SS}} = \mathbf{c}_k + \mu_k \mathrm{sign}(\mathbf{x}_k^*)\mathrm{sign}(d_k - y_k) \tag{2.13}$$

We neglect the sign version described in [19, Sect. 6.5], in which only $d_k - y_k$ is replaced by its sign version, as the two versions above are commonly preferred to this version because of their improved performance.

2.3 Continuous-Time Model

We now derive the cost function for the LMS algorithm starting from the continuous-time model of the system of Figure 1.5 shown in Figure 2.2; again we incorporate the gain of the interfering echo in the weight vector and consider the ideal physical transmission channel. The impulse response $p(t)$ of the shaping filter has square root raised cosine Fourier transform and its energy is normalized to 1. The receiver filter matched to the transmit one has impulse

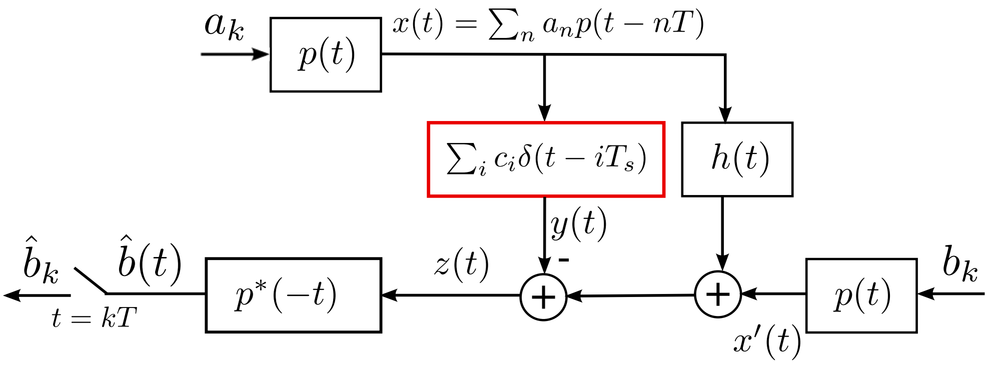

Figure 2.2: Continuous-time scheme for echo cancellation.

response $p^*(-t)$. The symbol period is $T = 1/f_{symb}$ and the sampling interval of the FIR filter is $T_s = T/N_u$. The transversal FIR filter, with impulse response given by $\sum_i c_i \delta(t - iT_s)$ and output $y(t)$, is shown in Figure 2.3.

The sequences $\{a_k\}$ and $\{b_k\}$ are modeled as described in Section 2.2. The echo channel response is $h(t)$, the continuous-time interfering signal is $x(t)$ and the transmitted and received signals are $x'(t)$ and $\hat{b}(t)$, respectively.

In order to define the MSE between $\hat{b}_k$ and b_k, we have to derive the discrete-time model of the system. The received symbol is $\hat{b}_k = \hat{b}(kT)$ and, denoting by $*$ the convolution operator, the received signal is

$$\begin{aligned}
\hat{b}(t) &= z(t) * p^*(-t) \\
&= \left[x(t) * h(t) + x'(t) - x(t) * \sum_{i=0}^{N-1} c_i \delta(t - iT_s) \right] * p^*(-t) \\
&= \left[x(t) * h(t) + x'(t) - \sum_{i=0}^{N-1} c_i x(t - iT_s) \right] * p^*(-t) \\
&= \left[\sum_n a_n p(t - nT) * h(t) + \sum_n b_n p(t - nT) - \right. \\
&\quad \left. + \sum_{i=0}^{N-1} c_i \sum_n a_n p(t - iT_s - nT) \right] * p^*(-t).
\end{aligned}$$

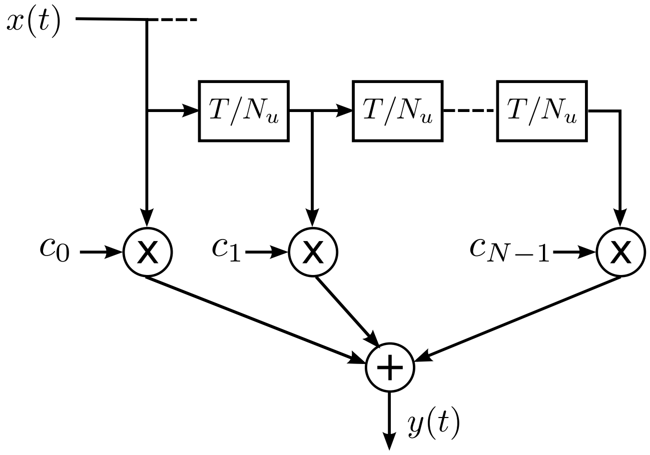

Figure 2.3: Transversal FIR filter.

Defining the overall pulse $g(t) = p(t) * p^*(-t)$ and its convolution with the echo channel impulse response $q(t) = g(t) * h(t)$, one can write

$$\begin{aligned}\hat{b}(t) &= \sum_n a_n q(t-nT) + \sum_n b_n g(t-nT) - \sum_{i=0}^{N-1} c_i \sum_n a_n g(t - iT_s - nT) \\ &= \sum_n a_n \left[q(t - nN_uT_s) - \sum_{i=0}^{N-1} c_i g(t - iT_s - nN_uT_s) \right] + \sum_n b_n g(t - nN_uT_s)\end{aligned} \tag{2.14}$$

where we used $T = N_uT_s$.

Sampling the received signal at $t = kT$, one has

$$\begin{aligned}\hat{b}_k &= \hat{b}(kT) \\ &= \sum_n a_n \left[q[(k-n)N_uT_s)] - \sum_{i=0}^{N-1} c_i g[(k-n)N_uT_s - iT_s] \right] + \sum_n b_n g[(k-n)N_uT_s] \\ &\overset{(a)}{=} \sum_n a_n \left[q_{(k-n)N_u} - \sum_{i=0}^{N-1} c_i g_{(k-n)N_u - i} \right] + b_k\end{aligned} \tag{2.15}$$

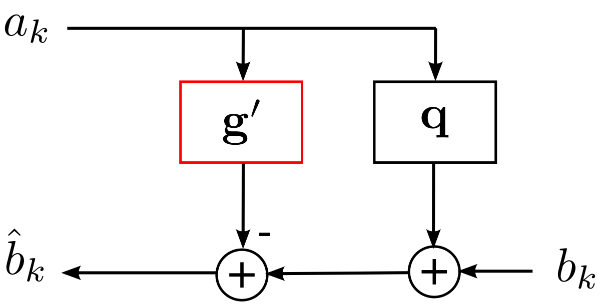

Figure 2.4: Discrete-time overall scheme for echo cancellation.

where $g_i = g(iT_s)$ and in (a) we have used the fact that

$$g_{iN_u} = \begin{cases} 1 & i = 0 \\ 0 & i \neq 0 \end{cases}.$$

The discrete-time model thus reduces to that shown in Figure 2.4, where we define $g'_j = \sum_{i=0}^{N-1} c_i g_{j-i}$ and $\hat{b}_k$ is given by (2.15).

If the echo impulse response band is less or equal to $f_s/2$, it can be sampled at f_s, that is

$$h(t) = \sum_m h(mT_s)\mathrm{sinc}\left(\frac{t - mT_s}{T_s}\right).$$

In (2.15) one can note that if $q_{nN_u} = \sum_{i=0}^{N-1} c_i g_{nN_u - i}$ for every n, the echo is totally cancelled and $\hat{b}_k = b_k$. From the definition of $q(t)$, one has

$$\begin{aligned} q_{nN_u} &= \int \sum_m h(mT_s)\mathrm{sinc}\left(\frac{\tau - mT_s}{T_s}\right) g[nT - \tau]\mathrm{d}\tau \\ &\overset{(a)}{=} \sum_m h(mT_s) \int \mathrm{sinc}\left(\frac{\tau'}{T_s}\right) g[nT - mT_s - \tau']\mathrm{d}\tau \\ &\overset{(b)}{=} \sum_m h(mT_s) g_{nN_u - m} \end{aligned} \tag{2.16}$$

where in (a) we set $\tau' = \tau - mT_s$ and in (b) we use $\mathrm{sinc}(\frac{t}{T_s}) * g(t) = g(t)$, since the band of the overall pulse $g(t)$, which has raised cosine Fourier transform, does not exceed the band $f_s/2$. Therefore, for $N_u \geq 2$, from (2.15) and (2.16) one can see that the echo can be totally cancelled if and only if $c_i = h(iT_s)$ for $i = 0, ..., N-1$, i.e. if the filter weights are equal to the echo channel impulse response samples.

The cost function to be minimized is the MSE between $\hat{b}_k$ and b_k, therefore recalling (2.1)

$$\begin{aligned}\mathcal{E}(\mathbf{c}) &= \mathbb{E}\{|\hat{b}_k - b_k|^2\} \\ &= \mathbb{E}\{\hat{b}_k\hat{b}_k^*\} + \mathbb{E}\{b_k b_k^*\} - 2\mathrm{Re}\left[\mathbb{E}\{b_k\hat{b}_k^*\}\right] \\ &= \mathbb{E}\{\hat{b}_k\hat{b}_k^*\} + \sigma_b^2 - 2\mathrm{Re}\left[\mathbb{E}\{b_k\hat{b}_k^*\}\right] \qquad (2.17)\end{aligned}$$

where now, for (2.15), one has

$$\begin{aligned}\mathbb{E}\{b_k\hat{b}_k^*\} &= \sum_n \mathbb{E}\{a_n^* b_k\}\left[q^*_{(k-n)N_u} - \sum_i c_i^* g^*_{(k-n)N_u-i}\right] + \sigma_b^2 \\ &= \sigma_b^2 \qquad (2.18)\end{aligned}$$

since $\mathbb{E}\{a_n^* b_k\} = 0$ as the symbols are uncorrelated and zero mean.

Defining $\hat{b'}_k = \sum_n a_n[q_{(k-n)N_u} - \sum_i c_i g_{(k-n)N_u-i}]$, the first term in the MSE (2.17) is

$$\begin{aligned}\mathbb{E}\{\hat{b}_k\hat{b}_k^*\} &= \mathbb{E}\{\hat{b'}_k\hat{b'}^*_k\} + \sigma_b^2 - 2\mathrm{Re}\left[\sum_n \mathbb{E}\{a_n^* b_k\}[q^*_{(k-n)N_u} - \sum_i c_i^* g^*_{(k-n)N_u-i}]\right] \\ &= \mathbb{E}\{\hat{b'}_k\hat{b'}^*_k\} + \sigma_b^2. \qquad (2.19)\end{aligned}$$

For (2.18) and (2.19), the MSE is then

$$\begin{aligned}\mathcal{E}(\mathbf{c}) &= \mathbb{E}\{\hat{b'}_k\hat{b'}^*_k\} + \sigma_b^2 + \sigma_b^2 - 2\sigma_b^2 \\ &= \mathbb{E}\{\hat{b'}_k\hat{b'}^*_k\}\end{aligned}$$

which can be expanded as

$$\begin{aligned}
\mathcal{E}(\mathbf{c}) &= \mathbb{E}\{\hat{b}'_k \hat{b}'^*_k\} \\
&= \mathbb{E}\left\{\sum_n a_n[q_{(k-n)N_u} - \sum_i c_i g_{(k-n)N_u-i}] \sum_m a^*_m[q^*_{(k-m)N_u} - \sum_j c^*_j g^*_{(k-m)N_u-j}]\right\} \\
&= \sum_n \sum_m \mathbb{E}\{a_n a^*_m\}[q_{(k-n)N_u} - \sum_i c_i g_{(k-n)N_u-i}][q^*_{(k-m)N_u} - \sum_j c^*_j g^*_{(k-m)N_u-j}] \\
&= \sigma_a^2 \sum_n [q_{(k-n)N_u} - \sum_i c_i g_{(k-n)N_u-i}][q^*_{(k-n)N_u} - \sum_j c^*_j g^*_{(k-n)N_u-j}] \\
&= \sigma_a^2 \left\{\sum_i \sum_j c_i c^*_j \sum_n g_{(k-n)N_u-i} \overset{*}{g}_{(k-n)N_u-j} + \right. \\
&\quad - \sum_i c_i \sum_n q^*{}_{(k-n)N_u} g_{(k-n)N_u-i} - \sum_j c^*_j \sum_n q_{(k-n)N_u} g^*_{(k-n)N_u-j} + \\
&\quad \left. + \sum_n q_{(k-n)N_u} q^*{}_{(k-n)N_u} \right\} \\
&\overset{(a)}{=} \sigma_a^2 \left\{\sum_i \sum_j c_i c^*_j \sum_n g_{nN_u-i} \overset{*}{g}_{nN_u-j} - 2\mathrm{Re}\left[\sum_i c_i \sum_n q^*_{nN_u} g_{nN_u-i}\right] + \right. \\
&\quad \left. + \sum_n |q_{nN_u}|^2 \right\}
\end{aligned}$$

where in (a) we have changed the summation index n, since the sum on n goes from $-\infty$ to ∞ and is invariant to the index k, and we have recognized the real part of a complex number λ as $\mathrm{Re}[\lambda] = (\lambda + \lambda^*)/2$.

The quadratic form of the MSE can be recognized defining

$$\begin{aligned}
A_{ij} &= \sum_n g_{nN_u-i} g^*_{nN_u-j} \quad \text{for } i, j = 0, ..., N-1 \\
v_i &= \sum_n g_{nN_u-i} q^*_{nN_u} \quad \text{for } i = 0, ..., N-1
\end{aligned}$$

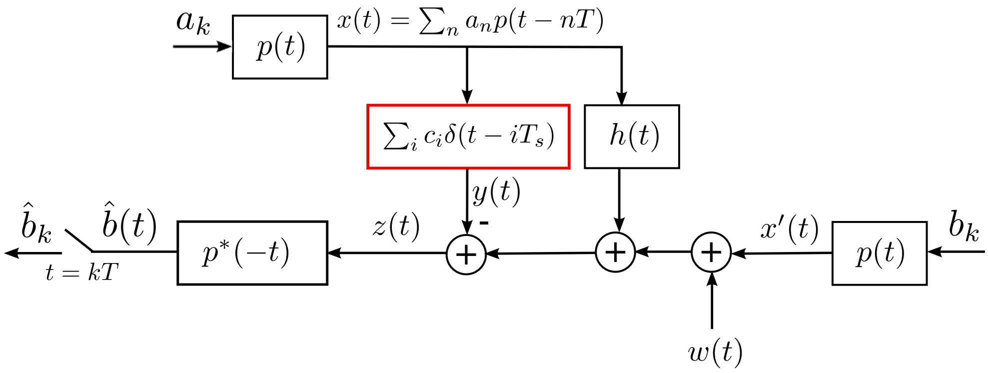

Figure 2.5: Continuous-time scheme for echo cancellation in the presence of AWGN.

so that

$$\mathcal{E}(\mathbf{c}) = \sigma_a^2(\mathbf{c}^H\mathbf{A}\mathbf{c} - 2\mathrm{Re}[\mathbf{c}^H\mathbf{v}] + \sum_n |q_{nN_u}|^2). \qquad (2.20)$$

The gradient of (2.20) has the same form of (2.4), i.e.,

$$\nabla\mathcal{E}(\mathbf{c}) = 2\sigma_a^2(\mathbf{A}\mathbf{c} - \mathbf{v})$$

and the optimum weight vector is

$$\mathbf{c}^{opt} = \mathbf{A}^{-1}\mathbf{v}. \qquad (2.21)$$

As expected, note that $\mathcal{E}(\mathbf{c}^{opt}) = 0$.

Considering now the scheme in Figure 2.5, in which complex additive white gaussian noise $w(t)$, with zero mean and power spectral density $S_w(f) = N_0$, is taken into account, (2.14) becomes

$$\begin{aligned} \hat{b}(t) &= \sum_n a_n \left[q(t - nN_uT_s) - \sum_{i=0}^{N-1} c_i g(t - iT_s - nN_uT_s) \right] + \\ &\quad + \sum_n b_n g(t - nN_uT_s) + n(t) \end{aligned}$$

and we can define the filtered version of $w(t)$, which has still gaussian distribution and zero mean, as $n(t) = w(t) * p^*(-t)$. The power spectral density of the filtered noise is the Fourier transform of the autocorrelation function of $n(t)$, given by $R_n(\tau) = \mathbb{E}\{n(t+\tau)n^*(t)\}$, and it is given by [6]

$$S_n(f) \quad = \quad S_w(f)\,|P(f)|^2\,.$$

Therefore, the variance of $n(t)$ is

$$\begin{aligned} \sigma_n^2 &= \mathbb{E}\{n(t+\tau)n^*(t)\}|_{\tau=0} \\ &= R_n(0) \end{aligned}$$

where

$$\begin{aligned} R_n(0) &= \int S_n(f)\mathrm{d}f \\ &= \int S_w(f)\left|P(f)^2\right|\mathrm{d}f \\ &= N_0 \int \left|P(f)^2\right|\mathrm{d}f \\ &= N_0 \end{aligned}$$

where, since $p(t)$ has unit energy, we used $\int \left|P(f)^2\right| \mathrm{d}f = 1$.

The discrete-time output (2.15) then becomes

$$\hat{b}_k = \sum_n a_n \left[q_{(k-n)N_u} - \sum_{i=0}^{N-1} c_i g_{(k-n)N_u - i} \right] + b_k + n_k \tag{2.22}$$

where

$$n_k \quad = \quad \int w(\tau)p^*(\tau - kT)\mathrm{d}\tau$$

and

$$\begin{aligned}\mathbb{E}\{n_k n_m^*\} &= \begin{cases} N_0 & n = m \\ 0 & n \neq m \end{cases} \\ &= \sigma_n^2 \end{aligned} \tag{2.23}$$

Using the independence between n_k and the transmitted symbols a_k and b_k, it is straightforward to show that (2.20) in the presence of AWGN becomes

$$\mathcal{E}(\mathbf{c}) = \sigma_a^2(\mathbf{c}^H \mathbf{A}\mathbf{c} - 2\mathrm{Re}[\mathbf{c}^H \mathbf{v}] + \sum_n |q_{nN_u}|^2) + \sigma_n^2 \tag{2.24}$$

while the gradient function and the optimal weights remain the same as in the case of the absence of AWGN. This is an important result since it shows that the optimal LMS solution is not influenced by the AWGN, i.e. the weight update algorithm has to converge to the same optimal solution, represented by the echo channel impulse response samples, even in the presence of AWGN and independently of the value of σ_n^2. Note that using (2.22), the MSE is

$$\begin{aligned}\mathcal{E}(\mathbf{c}) &= \mathbb{E}\{|\hat{b}_k - b_k|^2\} \\ &= \mathbb{E}\left\{\left|\sum_n a_n \left[q_{(k-n)N_u} - \sum_{i=0}^{N-1} c_i g_{(k-n)N_u-i}\right] + b_k + n_k - b_k\right|^2\right\} \\ &= \mathbb{E}\left\{\left|\sum_n a_n \left[q_{(k-n)N_u} - \sum_{i=0}^{N-1} c_i g_{(k-n)N_u-i}\right] + n_k\right|^2\right\}.\end{aligned}$$

If the echo is totally cancelled by $q_{nN_u} = \sum_{i=0}^{N-1} c_i g_{nN_u-i}$, one has

$$\begin{aligned}\mathcal{E}(\mathbf{c}^{opt}) &= \mathbb{E}\{|n_k|^2\} \\ &= \sigma_n^2\end{aligned} \tag{2.25}$$

2.3.1 MSE Formulation in the Presence of Impulse Noise

In the presence of impulse noise, the MSE $\mathcal{E}^I(\mathbf{c})$, given by (2.24), can be modified as

$$\mathcal{E}^I(\mathbf{c}) = \sigma_a^2(\mathbf{c}^H\mathbf{A}\mathbf{c} - 2\mathrm{Re}[\mathbf{c}^H\mathbf{v}] + \sum_n |q_{nN_u}|^2) + \sigma_i^2 \tag{2.26}$$

where σ_i^2 is given by (1.7). We can evaluate the difference, in terms of theoretical MSE, between the MSE for AWGN with variance σ_G^2 and that for bursty impulse noise with overall variance σ_i^2. Defining

$$\Delta\mathcal{E} = \mathcal{E}^I(\mathbf{c}) - \mathcal{E}(\mathbf{c}), \tag{2.27}$$

using (2.24) in the form

$$\mathcal{E}(\mathbf{c}) = \sigma_a^2(\mathbf{c}^H\mathbf{A}\mathbf{c} - 2\mathrm{Re}[\mathbf{c}^H\mathbf{v}] + \sum_n |q_{nN_u}|^2) + \sigma_G^2$$

and using (1.7), one has

$$\Delta\mathcal{E} = \sigma_G^2 P_B(R-1). \tag{2.28}$$

that is non zero for $P_B \neq 0$ or $R \neq 1$. Note that, since, as discussed in Chapter 2, the optimal solution of the algorithm does not depend on the noise, $\Delta\mathcal{E}$ does not depend on $\mathbf{c}$ and the performance degradation is due only to the different average noise power at the receiver.

2.4 LMS Algorithm Formulation at Sampling Frequency

In the previous Section, we have analyzed the echo cancellation at the sampling frequency $1/T_s$ defining the MSE at symbol time. The cancellation could be equally performed at symbol time T, decreasing the computational load, but

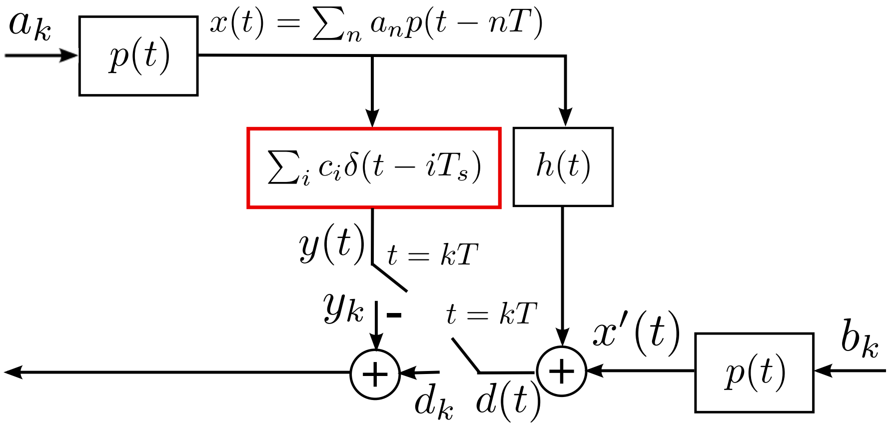

Figure 2.6: Continuous-time scheme for echo cancellation without receiver.

because of the different time scale of the local interfering signal and the desired remote one, in a real system this would require an additional synchronization between the signals. This makes the echo cancellation at symbol time less suitable for real systems. For this reason one can also define a cost function to be minimized in terms of quantities sampled with period T_s.

Considering the scheme in Figure 2.6, in which again we start by neglecting the AWGN, we initially define the MSE at discrete times, multiple of T, between the output of the adaptive filter and the intended signal plus the echoed one that, as mentioned in Section 2.2, is an equivalent formulation for the cost function for the echo cancellation. One has

$$\begin{aligned} y(t) &= x(t) * \sum_i c_i \delta(t - iT_s) \\ &= \sum_i c_i \sum_n a_n p(t - iT_s - nT) \end{aligned} \tag{2.29}$$

and

$$d(t) = x(t) * h(t) + x'(t)$$

$$= \sum_n a_n q'(t-nT) + \sum_n b_n p(t-nT) \tag{2.30}$$

where we define $q'(t) = p(t) * h(t)$. Sampling the signals with period $T = N_u T_s$ one has

$$\begin{aligned} y_k &= \sum_n a_n \sum_i c_i p_{(k-n)N_u-i} \\ d_k &= \sum_n a_n q'_{(k-n)N_u} + \sum_n b_n p_{(k-n)N_u}. \end{aligned}$$

One can see that if $q'_{nN_u} = \sum_i c_i p_{nN_u-i}$ the echo is totally cancelled and $y_k - d_k = \sum_n b_n p_{(k-n)N_u}$, which, after receiver filtering and sampling, is the intended signal b_k. Note that

$$\begin{aligned} q'_{nN_u} &= \int \sum_m h(mT_s)\mathrm{sinc}\left(\frac{\tau - mT_s}{T_s}\right) p[nT-\tau]\mathrm{d}\tau \\ &= \sum_m h(mT_s) p_{nN_u-m} \end{aligned}$$

Defining the MSE between d_k and y_k, with similar manipulations as in Section 2.3, one has

$$\begin{aligned} \mathcal{E}'(\mathbf{c}) &= \mathbb{E}\{|d_k - y_k|^2\} \\ &= \sigma_a^2(\mathbf{c}^H\mathbf{A}'\mathbf{c} - 2\mathrm{Re}[\mathbf{c}^H\mathbf{v}'] + \sum_n |q'_{nN_u}|^2) + \sigma_b^2 \end{aligned} \tag{2.31}$$

where

$$\begin{aligned} A'_{ij} &= \sum_n p_{nN_u-i} p^*_{nN_u-j} \quad \text{for } i,j = 0,...,N-1 \\ v'_i &= \sum_n p^*_{nN_u-i} q'_{nN_u} \quad \text{for } i = 0,...,N-1 \end{aligned}$$

and the optimal solution is $\mathbf{c}^{opt} = \mathbf{A}'^{-1}\mathbf{v}'$.

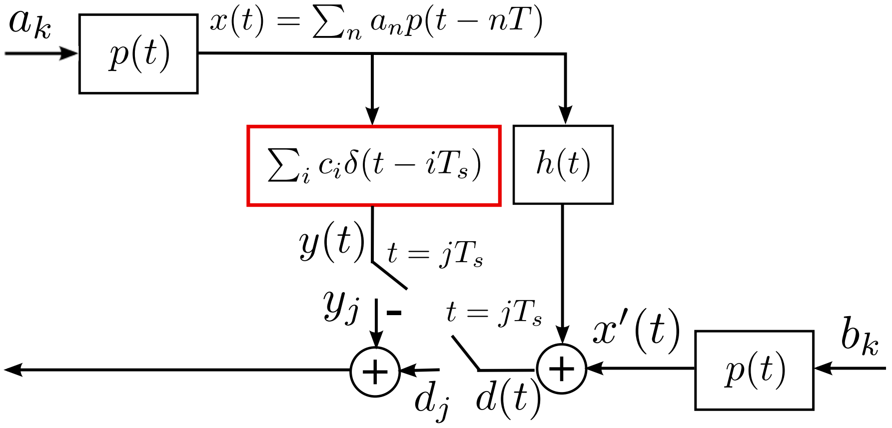

Figure 2.7: Continuous-time scheme for echo cancellation without receiver and sampling at T_s.

With reference to the scheme in Figure 2.7, let us now consider sampling with period $T_s = T/N_u$. Accordingly, we have $y_j = y(jT_s)$ and $d_j = d(jT_s)$, so that

$$\begin{aligned} y_j &= \sum_n a_n \sum_i c_i p_{j-i-nN_u} \\ d_j &= \sum_n a_n q'_{j-nN_u} + \sum_n b_n p_{j-nN_u}. \end{aligned}$$

One can see that if $q'_{j-nN_u} = \sum_i c_i p_{j-i-nN_u}$ the echo is totally cancelled. If the bandwidth of $h(t)$ is limited to $f_s/2$, one has

$$\begin{aligned} q'_{j-nN_u} &= \int \sum_m h(mT_s)\mathrm{sinc}\left(\frac{\tau - mT_s}{T_s}\right) p[jT_s - nT - \tau]\mathrm{d}\tau \\ &= \sum_m h(mT_s) p_{j-m-nN_u} \end{aligned}$$

The MSE defined at T_s is

$$\mathcal{E}''(\mathbf{c}) = \mathbb{E}\{|d_j - y_j|^2\} \tag{2.32}$$

$$= \mathbb{E}\{|d_j|^2\} + \mathbb{E}\{|y_j|^2\} - 2\mathrm{Re}[\mathbb{E}\{|d_j y_j^*|\}].$$

With some manipulations one has

$$\begin{aligned}
\mathbb{E}\{|d_j|^2\} &= \sigma_a^2 \sum_n |q'_{j-nN_u}|^2 + \sigma_b^2 \sum_n |p_{j-nN_u}|^2 \\
\mathbb{E}\{|y_j|^2\} &= \sigma_a^2 \sum_l \sum_i c_i c_l^* \sum_n p_{j-i-nN_u} p^*_{j-l-nN_u} \\
\mathbb{E}\{|d_j y_j^*|\} &= \sigma_a^2 \sum_i c_i^* \sum_n p^*_{j-i-nN_u} q^{'}_{j-nN_u}.
\end{aligned}$$

Defining $j = kN_u + j'$, where $j' = 0, ..., N_u - 1$ is the sampling index within the k-th symbol time, one obtains

$$\begin{aligned}
\mathbb{E}\{|d_j|^2\} &= \sigma_a^2 \sum_n |q'_{(k-n)N_u+j'}|^2 + \sigma_b^2 \sum_n |p_{(k-n)N_u+j'}|^2 \\
\mathbb{E}\{|y_j|^2\} &= \sigma_a^2 \sum_l \sum_i c_i c_l^* \sum_n p_{(k-n)N_u-i+j'} p^*_{(k-n)N_u-l+j'} \\
\mathbb{E}\{|d_j y_j^*|\} &= \sigma_a^2 \sum_i c_i^* \sum_n p^*_{(k-n)N_u-i+j'} q^{'}_{(k-n)N_u+j'}.
\end{aligned}$$

Defining $n' = k - n$ and renaming n' as n for ease of presentation, one can define

$$A^{''}_{il}(j') = \sum_n p_{nN_u-i+j'} p^*_{nN_u-l+j'} \quad \text{for } i, l = 0, ..., N-1 \text{ and } j' = 0, ..., N_u - 1 \tag{2.33}$$

$$v^{''}_i(j') = \sum_n p^*_{nN_u-i+j'} q^{'}_{nN_u+j'} \quad \text{for } i = 0, ..., N-1 \text{ and } j' = 0, ..., N_u - 1 \tag{2.34}$$

and the quadratic form of the MSE is

$$\mathcal{E}''(\mathbf{c}, j') = \sigma_a^2(\mathbf{c}^H \mathbf{A}''(j')\mathbf{c} - 2\mathrm{Re}[\mathbf{c}^H \mathbf{v}''(j')] + \sum_n |{q'}_{nN_u+j'}|^2) + \sigma_b^2 \qquad (2.35)$$

The optimum weight vector is therefore

$$\mathbf{c}^{opt}(j') = \mathbf{A}''^{-1}(j')\mathbf{v}''(j') \quad \text{for } j' = 0, ..., N_u - 1.$$

This means that there are N_u optimum solutions, one for each value of j', i.e., there are N_u optimum weight vectors, as it will be shown numerically later. However, the algorithm is expected to converge to a unique optimal solution, represented by the samples of the echo channel impulse response, i.e., the optimum weight vectors are expected to be independent on j', that is

$$c_i^{opt}(j') = c_i^{opt} = h(iT_s) \quad \forall j' \in [0, ..., N_u - 1]$$

and $\mathcal{E}''(\mathbf{c}^{opt}(j'), j') = \sigma_b^2 \quad \forall j' \in [0, ..., N_u - 1]$.

This phenomenon is caused by the cyclostationary nature of the various signals over one symbol period. To circumvent this issue, the following time average of the MSE can be adopted as the cost function:

$$\mathcal{E}''(\mathbf{c}) = \frac{1}{N_u} \sum_{j'=0}^{N_u-1} \mathcal{E}''(\mathbf{c}, j')$$

The LMS algorithm for the weight update, given by (2.6) in its symbol time version, for echo cancellation at sampling rate f_s is

$$\mathbf{c}_{j+1} = \mathbf{c}_j - \frac{1}{2}\mu \hat{\nabla}_{\mathbf{c}} \mathcal{E}''|_{\mathbf{c}=\mathbf{c}_j} \qquad (2.36)$$

where the stochastic gradient can now be derived as follows. Defining the gradient of $\mathcal{E}''(\mathbf{c})$, one has

$$\nabla_{\mathbf{c}} \mathcal{E}'' \;=\; \nabla_{\mathbf{c}} \mathbb{E}\{|d_j - y_j|^2\}$$

$$= \quad \mathbb{E}\{\nabla_{\mathbf{c}}|d_j - y_j|^2\}. \qquad (2.37)$$

Since $\{d_j\}$ do not depend on $\mathbf{c}$ and $\{y_j\}$ are complex quantities, (2.37) can be expressed as [27]

$$\nabla_{\mathbf{c}}\mathcal{E}'' \quad = \quad = \mathbb{E}\{-2\nabla_{\mathbf{c}} y_j^*(d_j - y_j)\}. \qquad (2.38)$$

Recalling that $x(jT_s) = \sum_n a_n p_{j-nN_u}$, the gradient of y_j^* with respect to the m-th element of the vector $\mathbf{c}$ is

$$\begin{aligned} \frac{\partial y_j^*}{\partial c_m} &= \frac{\partial}{\partial c_m} \sum c_i^* \sum_n a_n^* p_{j-i-nN_u}^* \\ &= \sum_n a_n^* p_{j-m-nN_u}^* \\ &= x_{j-m}^* \end{aligned}$$

for $m = 0, ..., N-1$, so that,

$$\nabla_{\mathbf{c}} y_j^* = \mathbf{x}_j^*$$

where $\mathbf{x}_j = (x_{j-N+1}, x_{j-N+2}, ..., x_j)^\intercal$. The gradient (2.38) can be then expressed as

$$\nabla_{\mathbf{c}}\mathcal{E}'' \quad = \quad \mathbb{E}\{-2\mathbf{x}_j^*(d_j - y_j)\}$$

and the stochastic gradient, as explained in Section 2.2, is an estimate of the gradient by means of a temporal average, i.e.,

$$\hat{\nabla}_{\mathbf{c}}\mathcal{E}'' \quad = \quad -2\mathbf{x}_j^*(d_j - y_j).$$

The weight update algorithm (2.36) is therefore

$$\mathbf{c}_{j+1} = \mathbf{c}_j + \mu\mathbf{x}_j^*(d_j - y_j). \qquad (2.39)$$

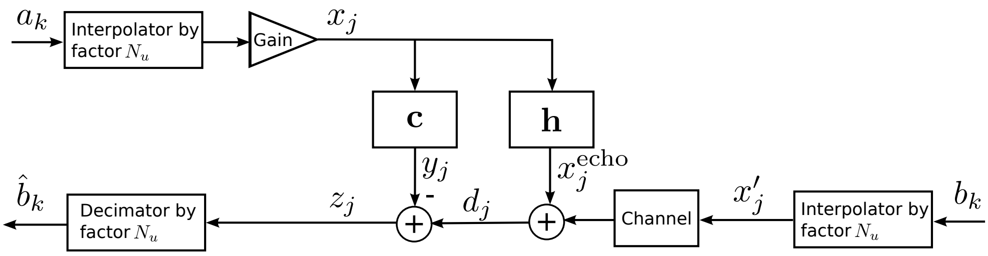

Figure 2.8: Discrete-time model for simulation.

2.5 Performance Analysis

The discrete-time model for simulation of the system depicted in Figure 2.5, is shown in Figure 2.8 where the gain of 32.5 dB discussed in Section 1.2.1 is considered. As specified in Section 1.2, the transmitted symbols $\{a_k\}$ and $\{b_k\}$ are complex QAM symbols, with constellation size $M = 16$. In fact, numerical results of our tests show that the echo cancellation process is not influenced at all by the size of the constellation M. As a representative case study, the symbol frequency is set as $f_{symb} = \nu_s/90$, where ν_s is the sampling frequency of the passband echo response, discussed in Section 1.2.1 and the interpolation factor is $N_u = 2$, i.e. $f_s = \nu_s/45$.

As mentioned in Section 1.2, interpolation and decimation are performed by means of a polyphase implementation of a filter with square-root raised-cosine Fourier transform. The roll-off factor β is set to 0.25. The discrete-time implementation of the filter allows to set its length, in terms of samples, also fixing the group delay D of the filter, defined as the number of symbol periods between the start of the impulse response and its peak. The length of the filter impulse response, assumed symmetric with respect to its peak, is thus set to $2N_uD + 1$. The value of D should be chosen as a tradeoff between the quality of the discrete-time representation of the objective frequency response and the reception delay. In particular, the delay in the sequence at the output of a matched receiver filter, with respect to the transmitted one, is equal to $2D$. The group delay is set to 32 symbols. An example impulse response of a

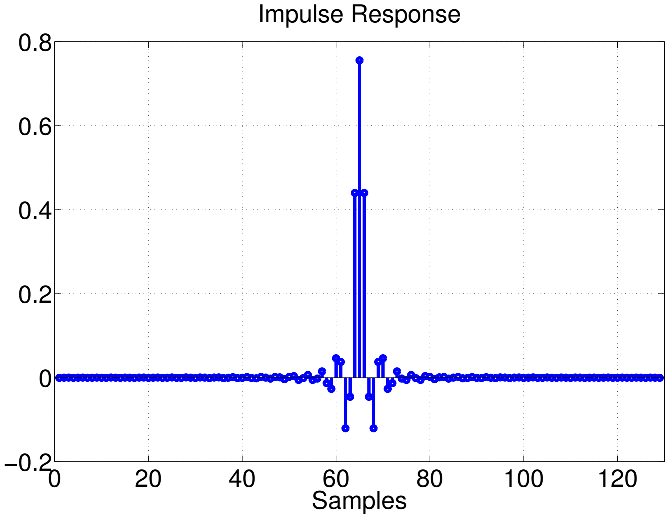

Figure 2.9: Truncated impulse response of the filter with square-root raised-cosine transform for $D = 32$, $Nu = 2$, and $\beta = 0.25$.

filter with square-root raised-cosine transform, with time-domain symmetric truncation, is shown in Figure 2.9 for $D = 32$, $N_u = 2$, and $\beta = 0.25$.

Since the baseband echo cancellation is performed at f_s and the available echo impulse response presented in Section 1.2.1 is sampled at ν_s MHz, such a response must be decimated down to $f_s = \nu_s/45$. The decimated echo impulse response is shown in Figure 2.10. The echo channel can be implemented in the system as a complex FIR filter, that consists of four real FIR filters [6]. The impulse response energy is normalized to 1. Since, as mentioned in Section 1.2.1, its duration, in terms of samples at ν_s, is $N = 1000$, the filter length (in terms of samples at f_s) is thus set to $\lfloor 1000/45 \rfloor = 22$.

The echo canceller adaptive filter weight update is performed by the LMS algorithm, with step size set to $\mu = 10^{-7}$, as we observed that this value allows an acceptable compromise between stability and convergence speed for the considered scenario and specified signal dynamics. The signal-to-noise-ratio

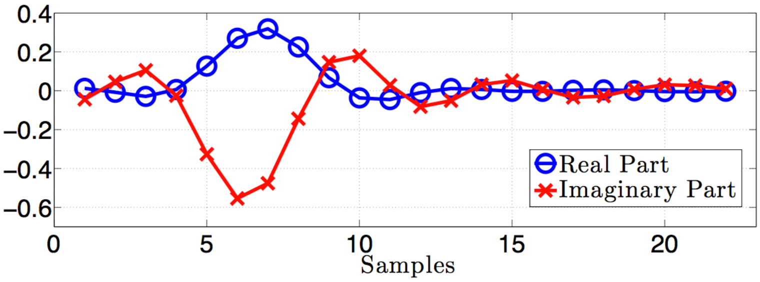

Figure 2.10: Baseband echo channel impulse response, sampled at f_s.

(SNR) is defined as

$$\mathrm{SNR} = \frac{E_s}{N_0}$$

where E_s is the signal energy per symbol. The transmission power is 0 dBW, so that $E_s = 1$ and one has

$$\mathrm{SNR} = \frac{1}{N_0}.$$

Therefore, according to (2.23) the variance of the filtered complex noise samples n_k at the receiver can be indicated as

$$\sigma_n^2 = \frac{1}{\mathrm{SNR}}. \tag{2.40}$$

2.5.1 AWGN Channel

Figure 2.11 shows the echo channel impulse response of Figure 2.10 and the adaptive filter weight vector obtained when the LMS algorithm has reached its convergence. One can appreciate that, as explained in Section 2.2, when the algorithm converges to its optimal solution, the adaptive filter replicates the echo impulse response. Also, one can note that the presence of AWGN does not affect the optimal solution to which the algorithm converges.

In Figure 2.12 the magnitude of the adaptive filter output and the echo channel output are shown in the absence of AWGN. One can appreciate how the signals are very similar, demonstrating that the echo can be cancelled.

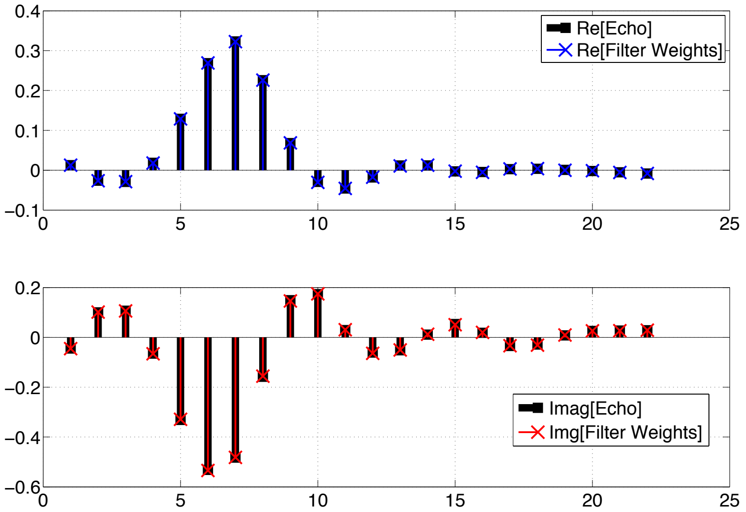

(a) No AWGN

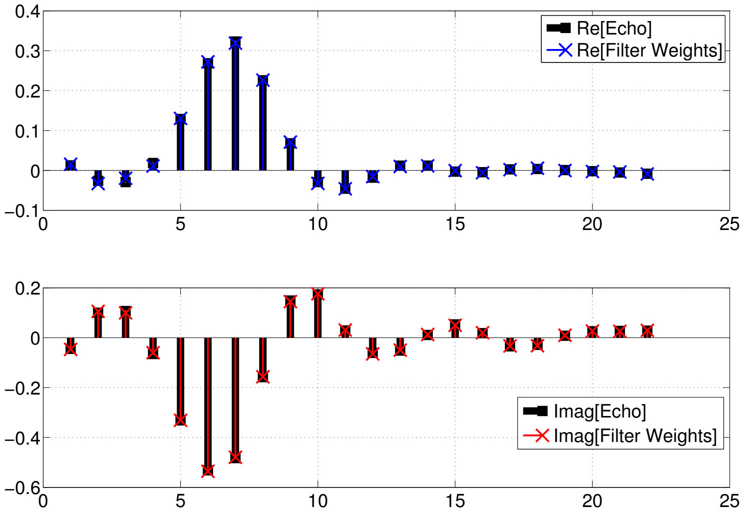

(b) SNR = 15 dB

Figure 2.11: Filter weights and echo impulse response.

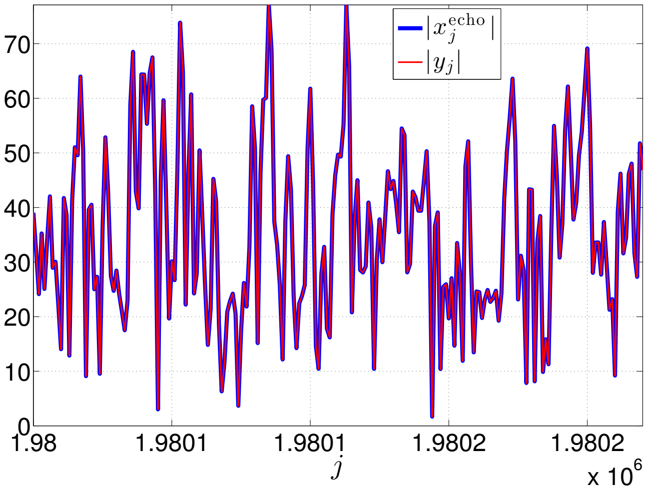

Figure 2.12: Magnitude of the LMS filter output and the echo channel output in the absence of AWGN.

Note that these signals are at rate f_s and the time index is therefore j.

In Section 2.2 we mentioned that it is not recommended to increase or decrease the adaptive filter length N with respect to the echo impulse response length, since in the first case the echo may not be completely cancelled, and in the second case the complexity increases. In order to analyze the performance of the echo canceller for different values of N, we consider the Symbol Error Rate (SER) as a performance metric. In Figure 2.13 the SER as a function of the adaptive filter tap number for SNR $= 15$ dB is shown. Recalling that the echo impulse response length is 22 samples, one can appreciate that for $N < 22$ the echo cannot be cancelled and the SER is very large, because the adaptive filter cannot reproduce the entire echo impulse response, as it is shown in part (a) of Figure 2.14. For $N > 22$ the SER falls sharply to low values compatible with the considered SNR (for the 16-QAM format). However, one may also notice that the SER slightly increases with N, as it is possible to see in part (b), since the adaptive filter does not reproduce exactly

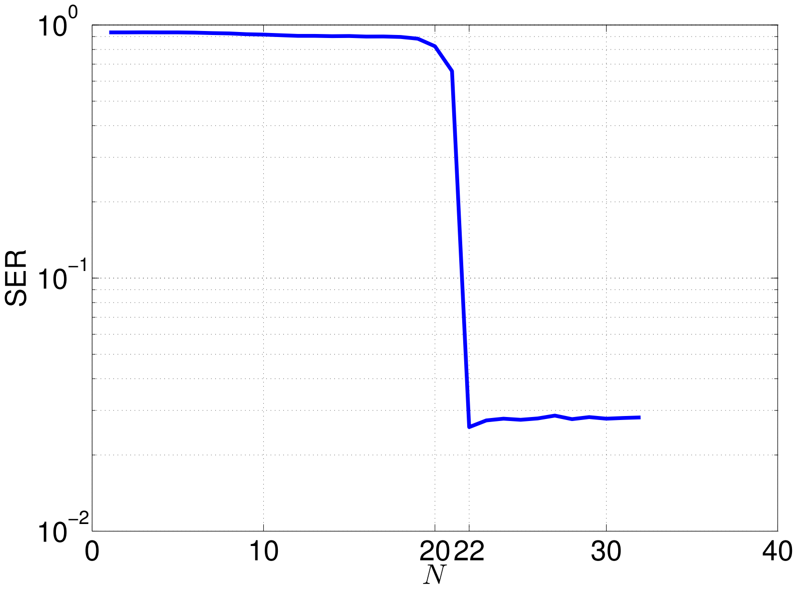

(a)

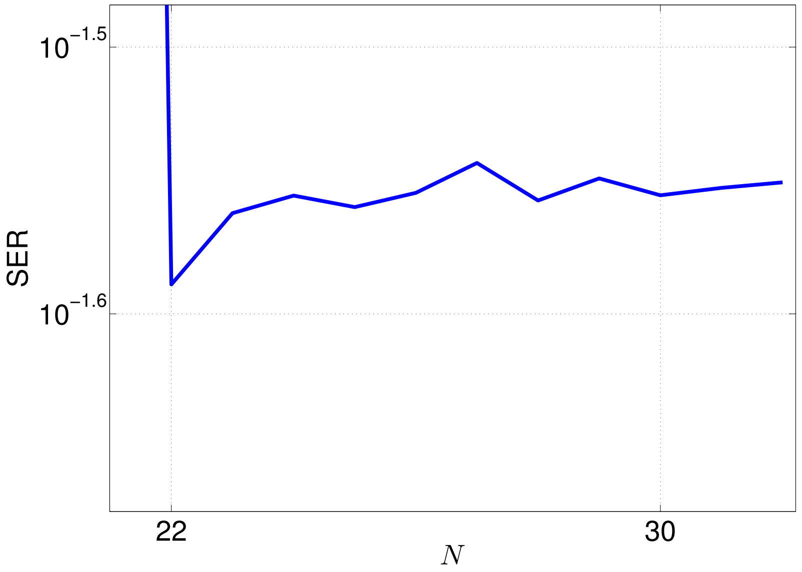

(b) Enlargement of (a)

Figure 2.13: SER as a function of the number N of the adaptive filter taps for SNR $= 15$ dB.

the echo, but something very similar to it, as it is shown in part (b) of Figure 2.14. The minimum of the SER, i.e., in this case, the value of the SER for a 16-QAM at SNR=15 dB, is therefore reached when the adaptive filter length is the same as the echo impulse response one.

For completeness, we finally show in Figure 2.15 the theoretical MSE, given by (2.24), and the empirical MSE, defined as

$$\hat{\mathcal{E}}(k) = |\hat{b}_k - b_k|^2 \tag{2.41}$$

in the absence of AWGN.

In Figure 2.16 the theoretical MSE for SNR = 15 dB is shown. One can note that in the presence of AWGN the theoretical MSE fluctuates around its minimum, given by (2.25).

2.5.2 Impulse Noise Channel

Figure 2.17 shows the empirical MSE given by (2.41) and the theoretical MSE given by (2.24), where

$$\mathcal{E}^I(\mathbf{c}|s_k) = \sigma_a^2(\mathbf{c}^H\mathbf{A}\mathbf{c} - 2\mathrm{Re}[\mathbf{c}^H\mathbf{v}] + \sum_n |q_{nN_u}|^2) + \sigma_{s_k}^2$$

and

$$\sigma_{s_k}^2 = \begin{cases} \sigma_G^2 & \text{if } s_k = G \\ R\sigma_G^2 & \text{if } s_k = B \end{cases}.$$

The impulse noise process is characterized by $P_B = 0.1$, $\gamma = 10$, and $R = 100$. Since in a realistic scenario $P_G \gg P_B$, the choice of P_B in this case represents a worst case. The signal-to-noise-ratio is SNR = 20 dB, meaning that, for (2.40), $\sigma_G^2 = \frac{1}{10^{\mathrm{SNR}_{\mathrm{dB}}/10}}$. Figure 2.18 shows the theoretical MSE in the presence of AWGN and bursty impulse noise for SNR = 20 dB, $P_B = 0.1$, $R = 100$, and various values of γ. For comparison, the minimum theoretical MSE values are also shown. First, one can note that the theoretical MSE in the presence of bursty impulse noise does not depend on the value of γ, as expected since σ_i^2

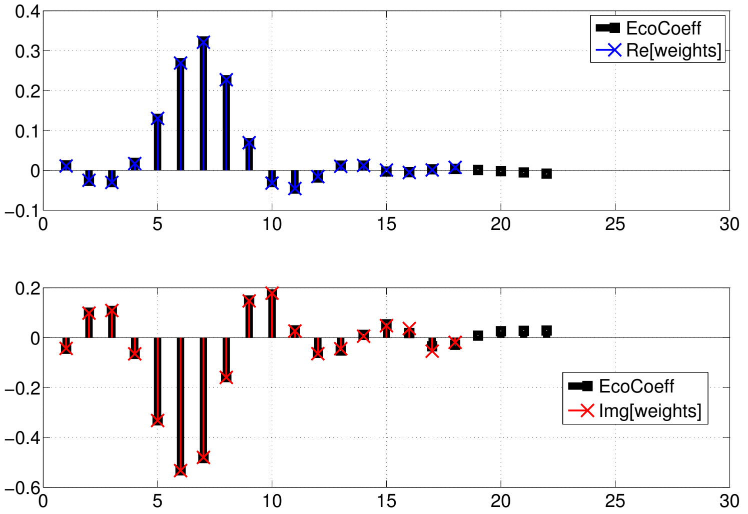

(a) $N = 18$

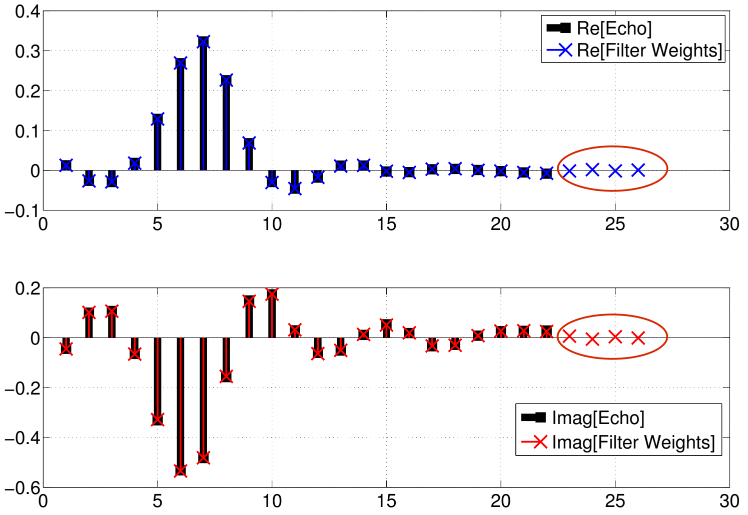

(b) $N = 26$

Figure 2.14: Filter weights and echo impulse response in the absence of AWGN; in (a) $N = 18$ and in (b) $N = 26$.

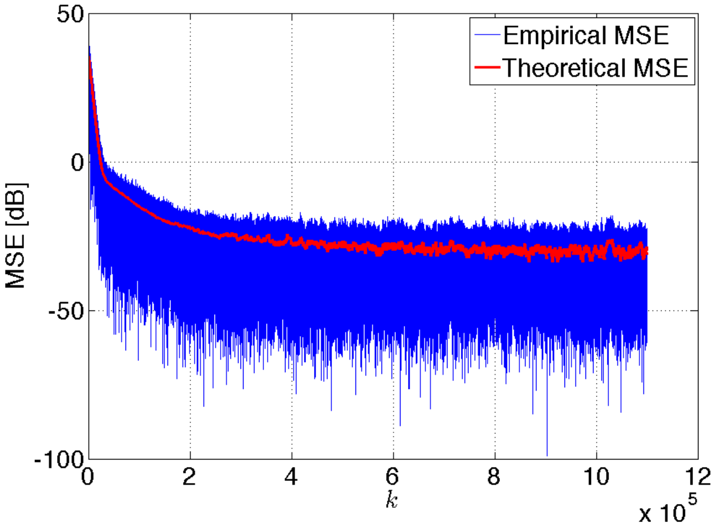

Figure 2.15: Theoretical MSE and empirical MSE in the absence of AWGN.

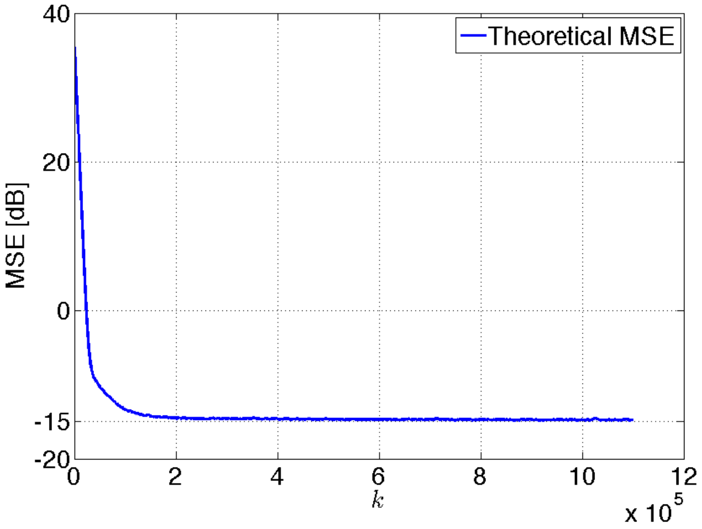

Figure 2.16: Theoretical MSE for SNR = 15 dB.

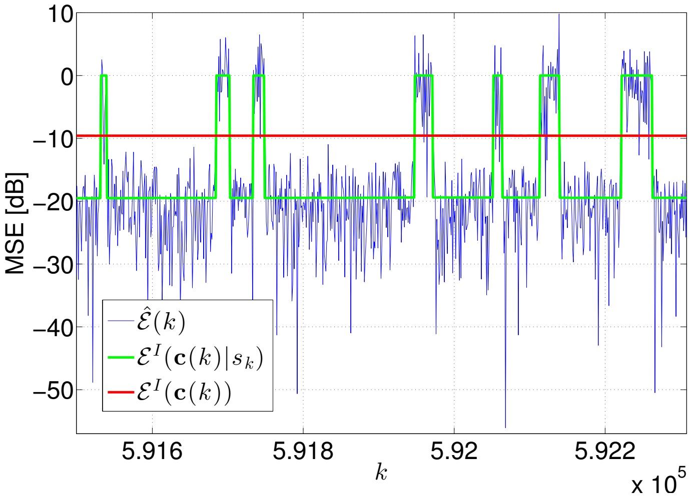

Figure 2.17: Empirical an theoretical MSE as a function of time in the presence of bursty impulse noise; SNR $= 20$ dB, $P_B = 10^{-1}$, $\gamma = 10$, and $R = 100$.

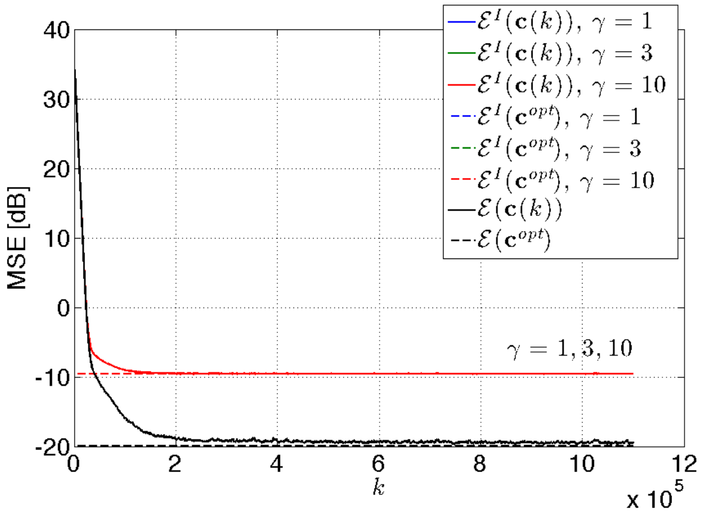

Figure 2.18: Theoretical MSE as a function of time in the presence of AWGN and bursty impulse noise; SNR $= 20$ dB, $P_B = 10^{-1}$, $R = 100$ and various values of γ.

does not depend on γ, and so it is for the minimum theoretical MSE obtained with the optimal weights. One can also appreciate that, from (2.28), one has

$$\begin{aligned}\Delta\mathcal{E} &= \frac{1}{10^{20/10}}0.1(100-1)\\ &= 0.099\\ &= -10.043\,\text{dB}\end{aligned}$$

that is, the impulse noise deteriorates the MSE about 10 dB with respect to the MSE evaluated for the AWGN channel, due to the increased average noise power.

2.6 Numerical Results on the Optimal Solution at Sampling Frequency

In Section 2.4 we defined the LMS cost function to be minimized as the MSE at sampling rate. We conjectured that the optimal solution does not depend on j', thus it is unique and consists of the echo channel impulse response samples at T_s, i.e.,

$$\mathbf{c}^{opt}(j') = \mathbf{c}^{opt} = h(iT_s) \quad \forall j' \in [0, ..., N_u - 1].$$

Here we numerically verify this behavior computing and exemplifying $\mathbf{A}^{''}(j')$, $\mathbf{v}^{'}(j')$ and the obtained optimal weight vectors $\mathbf{c}^{opt}(j')$ for $N_u = 2$, i.e., $j' = 0, 1$.

The time-domain symmetric truncation of $p(t)$ is shown in Figure 2.9, for $D = 32$, $N_u = 2$, and $\beta = 0.25$. We recall that the pulse energy is normalized to unit. The samples $\{h_m\}_{m=1}^{N}$ at f_s of an example echo channel impulse response are shown in Figure 2.19 for $N = 8$.

The 8×8 matrices $\mathbf{A}^{''}(0)$ and $\mathbf{A}^{''}(1)$, given by (2.33), are shown in Figure 2.20. One can note that $\mathbf{A}^{''}(1)$ is a circular shifted version of $\mathbf{A}^{''}(0)$ down and right along the main diagonal. Despite the determinants of $\mathbf{A}^{''}(0)$ and $\mathbf{A}^{''}(1)$ are very small (the order is about 10^{-11}), the inverse matrix could be computed for both matrices; they are shown in Figure 2.21. By direct inspection, it can

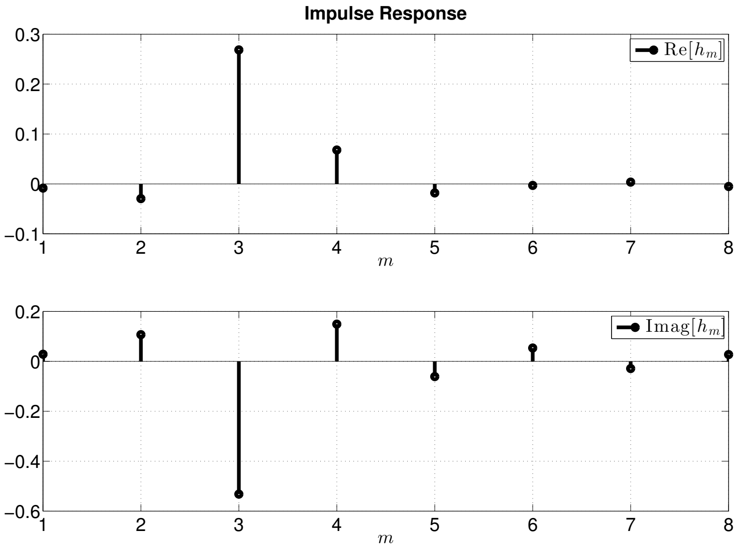

Figure 2.19: Example of echo channel impulse response $\{h_m\}_{m=1}^{8}$.

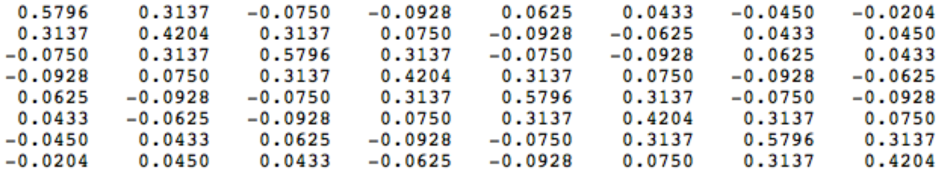

```
   0.5796    0.3137   -0.0750   -0.0928    0.0625    0.0433   -0.0450   -0.0204
   0.3137    0.4204    0.3137    0.0750   -0.0928   -0.0625    0.0433    0.0450
  -0.0750    0.3137    0.5796    0.3137   -0.0750   -0.0928    0.0625    0.0433
  -0.0928    0.0750    0.3137    0.4204    0.3137    0.0750   -0.0928   -0.0625
   0.0625   -0.0928   -0.0750    0.3137    0.5796    0.3137   -0.0750   -0.0928
   0.0433   -0.0625   -0.0928    0.0750    0.3137    0.4204    0.3137    0.0750
  -0.0450    0.0433    0.0625   -0.0928   -0.0750    0.3137    0.5796    0.3137
  -0.0204    0.0450    0.0433   -0.0625   -0.0928    0.0750    0.3137    0.4204
```

(a) $\mathbf{A}^{''}(0)$

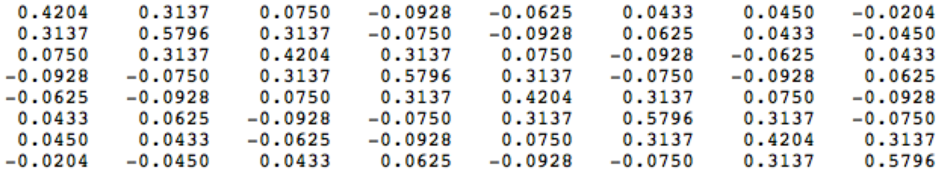

```
   0.4204    0.3137    0.0750   -0.0928   -0.0625    0.0433    0.0450   -0.0204
   0.3137    0.5796    0.3137   -0.0750   -0.0928    0.0625    0.0433   -0.0450
   0.0750    0.3137    0.4204    0.3137    0.0750   -0.0928   -0.0625    0.0433
  -0.0928   -0.0750    0.3137    0.5796    0.3137   -0.0750   -0.0928    0.0625
  -0.0625   -0.0928    0.0750    0.3137    0.4204    0.3137    0.0750   -0.0928
   0.0433    0.0625   -0.0928   -0.0750    0.3137    0.5796    0.3137   -0.0750
   0.0450    0.0433   -0.0625   -0.0928    0.0750    0.3137    0.4204    0.3137
  -0.0204   -0.0450    0.0433    0.0625   -0.0928   -0.0750    0.3137    0.5796
```

(b) $\mathbf{A}^{''}(1)$

Figure 2.20: Matrices $\mathbf{A}^{''}(j')$ for $j' = 0, 1$.

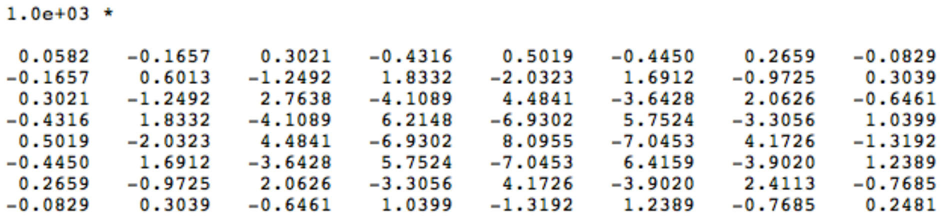

```
1.0e+03 *

  0.0582   -0.1657    0.3021   -0.4316    0.5019   -0.4450    0.2659   -0.0829
 -0.1657    0.6013   -1.2492    1.8332   -2.0323    1.6912   -0.9725    0.3039
  0.3021   -1.2492    2.7638   -4.1089    4.4841   -3.6428    2.0626   -0.6461
 -0.4316    1.8332   -4.1089    6.2148   -6.9302    5.7524   -3.3056    1.0399
  0.5019   -2.0323    4.4841   -6.9302    8.0955   -7.0453    4.1726   -1.3192
 -0.4450    1.6912   -3.6428    5.7524   -7.0453    6.4159   -3.9020    1.2389
  0.2659   -0.9725    2.0626   -3.3056    4.1726   -3.9020    2.4113   -0.7685
 -0.0829    0.3039   -0.6461    1.0399   -1.3192    1.2389   -0.7685    0.2481
```

(a) $\mathbf{A}''^{-1}(0)$

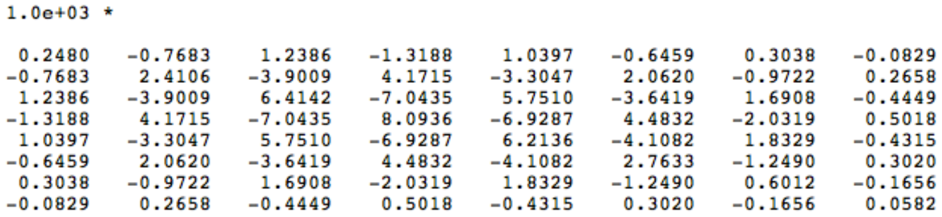

```
1.0e+03 *

  0.2480   -0.7683    1.2386   -1.3188    1.0397   -0.6459    0.3038   -0.0829
 -0.7683    2.4106   -3.9009    4.1715   -3.3047    2.0620   -0.9722    0.2658
  1.2386   -3.9009    6.4142   -7.0435    5.7510   -3.6419    1.6908   -0.4449
 -1.3188    4.1715   -7.0435    8.0936   -6.9287    4.4832   -2.0319    0.5018
  1.0397   -3.3047    5.7510   -6.9287    6.2136   -4.1082    1.8329   -0.4315
 -0.6459    2.0620   -3.6419    4.4832   -4.1082    2.7633   -1.2490    0.3020
  0.3038   -0.9722    1.6908   -2.0319    1.8329   -1.2490    0.6012   -0.1656
 -0.0829    0.2658   -0.4449    0.5018   -0.4315    0.3020   -0.1656    0.0582
```

(b) $\mathbf{A}''^{-1}(1)$

Figure 2.21: Inverse of matrices $\mathbf{A}''(j')$ for $j' = 0, 1$.

be verified that one is the symmetric matrix of the other with respect to their antidiagonal, as one can see also in Figure 2.22, where the rows of $\mathbf{A}''^{-1}(0)$ are plotted as solid lines and the rows of $\mathbf{A}''^{-1}(1)$ are plotted as dotted lines.

In Figure 2.23, $\mathbf{v}''(j')$, given by (2.34), is shown for $j' = 0, 1$. As it is more clear in Figure 2.24, where the magnitude of $\mathbf{v}''(j')$ is shown for $j' = 0, 1$, $\mathbf{v}''(0)$ and $\mathbf{v}''(1)$ are roughly similar.

The optimum weight vectors are given by

$$\mathbf{c}^{opt}(j') = \mathbf{A}''^{-1}(j')\mathbf{v}''(j') \quad \text{for } j' = 0, 1$$

and are shown in Figure 2.25. One can see that $\mathbf{c}^{opt}(0)$ is equal[2] to $\mathbf{c}^{opt}(1)$ and they coincide with the echo channel impulse response samples $\{h_m\}_{m=1}^{8}$, as it is more clear in Figure 2.26.

---

[2] Strictly speaking, $\mathbf{c}^{opt}(0) \simeq \mathbf{c}^{opt}(1)$, but the numerical error between the two weight vectors is on the order of 10^{-8}.

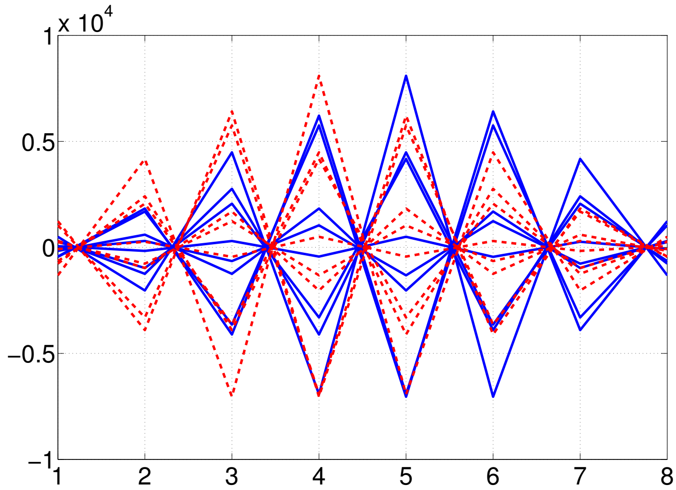

Figure 2.22: Rows of $\mathbf{A}''^{-1}(j')$. Solid lines are the rows for $j' = 0$ and dotted lines are the rows for $j' = 1$.

```
  0.0174 - 0.0107i
 -0.0271 + 0.0339i
 -0.0381 + 0.0469i
  0.0369 - 0.0184i
  0.1204 - 0.1098i
  0.1228 - 0.1476i
  0.0614 - 0.1005i
  0.0024 - 0.0039i
```

(a) $\mathbf{v}''(0)$

```
  0.0066 - 0.0161i
  0.0105 - 0.0306i
 -0.0245 + 0.0514i
 -0.0079 + 0.0596i
  0.1054 - 0.1129i
  0.1699 - 0.2310i
  0.0761 - 0.0994i
 -0.0418 + 0.0754i
```

(b) $\mathbf{v}''(1)$

Figure 2.23: Vectors $\mathbf{v}''(j')$ for $j' = 0, 1$.

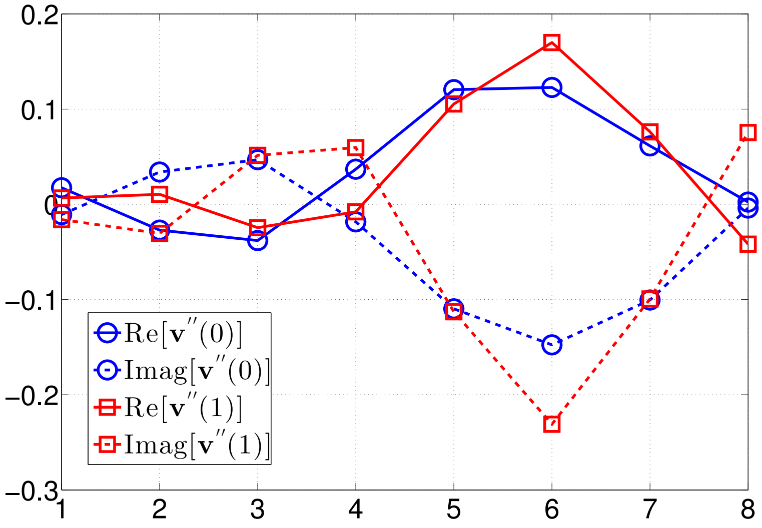

Figure 2.24: Real and imaginary parts of $\mathbf{v}''(j')$ for $j' = 0, 1$.

```
-0.0083 + 0.0285i
-0.0294 + 0.1071i
 0.2685 - 0.5318i
 0.0679 + 0.1491i
-0.0181 - 0.0609i
-0.0029 + 0.0533i
 0.0036 - 0.0287i
-0.0052 + 0.0272i
```

(a) $\mathbf{c}^{opt}(0)$

```
-0.0083 + 0.0285i
-0.0294 + 0.1071i
 0.2685 - 0.5318i
 0.0679 + 0.1491i
-0.0181 - 0.0609i
-0.0029 + 0.0533i
 0.0036 - 0.0287i
-0.0052 + 0.0272i
```

(b) $\mathbf{c}^{opt}(1)$

Figure 2.25: Optimum weight vectors $\mathbf{c}^{opt}(j')$ for $j' = 0, 1$.

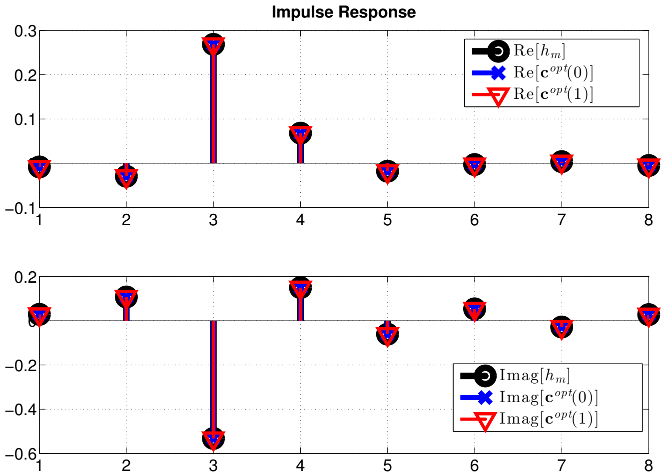

Figure 2.26: Echo channel impulse response $\{h_m\}_{m=1}^{8}$ and $\mathbf{c}^{opt}(j')$ for $j' = 0, 1$.

2.7 Conclusions

In this chapter, we presented the LMS algorithm used by the adaptive filter of the echo canceller and we described the echo cancellation for a full-duplex communication system. We discussed its normalized variant, the NLMS, and its variable-step variant, the VSLMS. We also derived the cost function of the algorithm, the MSE, in the case of the echo cancellation starting from a continuous-time model of the analyzed system. We showed that the AWGN channel does not influence the optimal solution, which consists in the echo channel impulse response samples. Since the echo cancellation is performed at the sampling frequency f_s, we also discussed the LMS algorithm formulation at sampling time $T_s = T/N_u$. We provided simulation results for both the cases of AWGN channel and impulse noise channel, demonstrating that the additive noise does not affect the echo cancellation process, except for the possibly increased steady-state value of the MSE, which depends on the noise power.

Chapter 3

Echo Cancellation in Multi-carrier Systems

3.1 Introduction

In a multi-carrier system, the available bandwidth is divided in a number of channels with equally-spaced carriers which are modulated independently [30]. multi-carrier systems are suitable for the communication over frequency-selective channels, as they are able to convert them into an equivalent set of parallel frequency-flat channels. Such a modulation technique is called Orthogonally Frequency Division Multiplexing (OFDM) [31, 32, 33] and it has been widely adopted in PLC system [1, 12, 34, 35, 36].

In this Chapter we discuss the echo cancellation in a full-duplex communication system in which the OFDM modulation format is adopted. Various echo cancellation frameworks have been proposed for multi-carrier communication systems operating in either time or frequency domains, aiming at reducing the computational complexity, rather than improving the echo canceller performance [37, 38, 39, 40, 41]. Since we are interested in a performance comparison between the previously described single-carrier system and the multi-carrier one, we focus on one echo cancellation scheme, in particular, the time-domain one.

The structure of this chapter is as follows. Section 3.2 provides an overview on the implementation of a multi-carrier communication system. In Section 3.3 the echo cancellation process in the multi-carrier system is discussed. In Section 3.4 the system performance is discussed. Finally, in Section 3.5 concluding remarks are given.

3.2 Multi-carrier System Overview

For consistence with the current literature, in this chapter a different notation for the number of the adaptive filter tap weights is adopted, with respect to the one used in the rest of the thesis, in order to use N to indicate the number of OFDM subcarriers. In particular, the following notation has been here adopted:

- C: number of the echo canceller adaptive FIR filter tap weights.
- N: number of independent subcarriers of a multiple carrier system.

The implementation of the OFDM modulator and demodulator by means of the Discrete Fourier Transform (DFT) pairs [31] is shown in Figure 3.1. The sequence $\{A_k[n]\}_{n=0}^{N-1}$ denotes the k-th block of transmitted symbols, each one with symbol period T and modulated, for example, by means of an M-ary Quadrature Amplitude Modulation (QAM) format and associated to the n-th subchannel. The N time-domain symbols of the multi-carrier signal in the k-th OFDM symbol, with period T/N are the Inverse DFT (IDFT) of $\{A_k[n]\}_{n=0}^{N-1}$

$$\begin{aligned} a_k[i] &= \text{IDFT}\{A_k[n]\} \\ &= \frac{1}{\sqrt{N}} \sum_{n=0}^{N-1} A_k[n] W_N^{ni} \qquad i = 0, .., N-1 \end{aligned} \tag{3.1}$$

where $W_N = e^{j2\pi/N}$ [4]. Because of the presented structure of the modulator, it is customary to refer to the domain inside the IDFT-DFT blocks as the

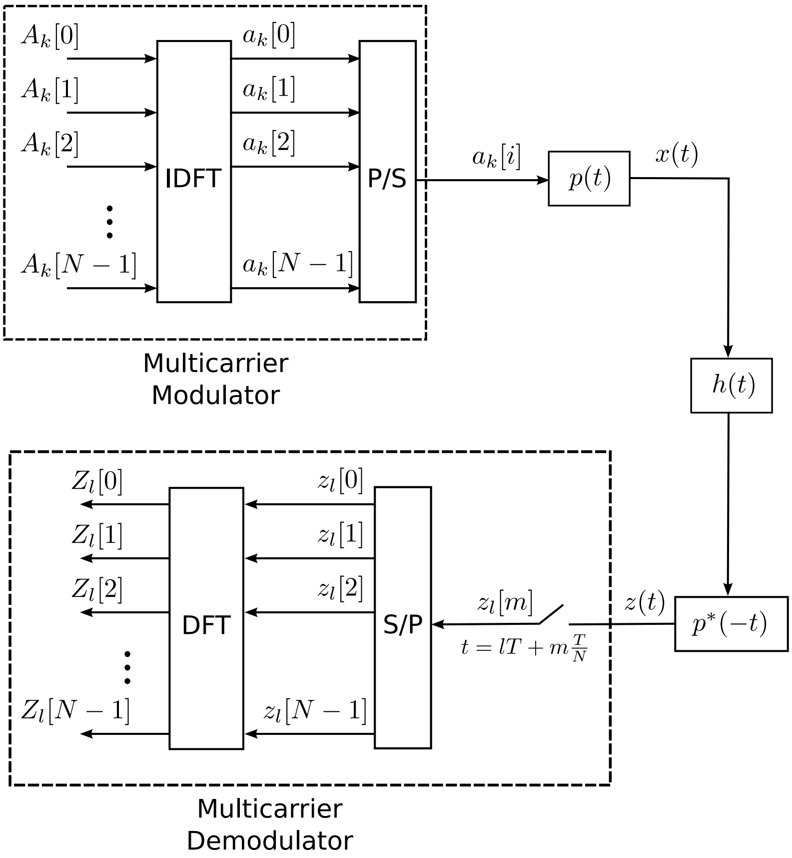

Figure 3.1: OFDM modulator and demodulator implemented by a DFT pair.

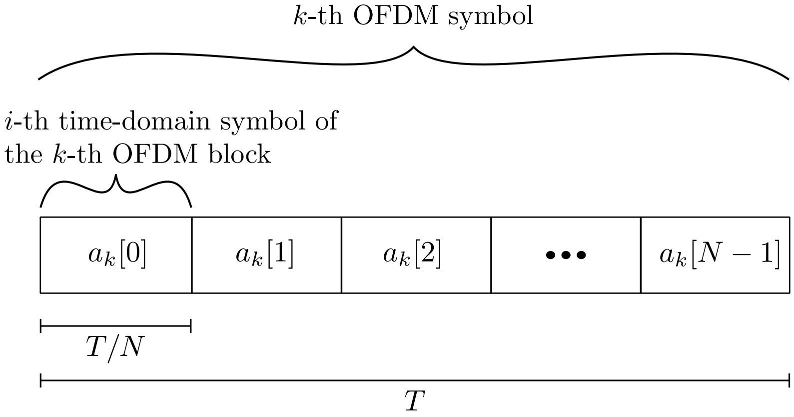

Figure 3.2: Structure of the k-th time-domain OFDM symbol.

frequency domain, while to the domain inside the IDFT-DFT blocks as the time domain, so that the symbols $A_k[n]$ are the frequency-domain versions of the time-domain symbols $a_k[i]$. Note that the index k specifies the k-th OFDM block, whereas the index n specifies the frequency-domain symbol, and the index i specifies the time-domain symbol inside of the OFDM block. Figure 3.2, shows the time-domain symbol block duration.

The sequence $\{a_k[i]\}_{i=0}^{N-1}$ is then serialized and pulse shaped, so that the transmitted signal is

$$x(t) = \sum_k \sum_{i=0}^{N-1} a_k[i] p(t - kT - i\frac{T}{N}) \tag{3.2}$$

where $p(t)$ denotes the impulse response of the pulse shaping filter. The received signal can be similarly expressed as

$$z(t) = \sum_k \sum_{i=0}^{N-1} a_k[i] q(t - kT - i\frac{T}{N}) \tag{3.3}$$

where the overall impulse response is denoted by $q(t) = p(t) * h(t) * p^*(-t)$, in which $h(t)$ denotes the channel impulse response and $p^*(-t)$ is the receive filter matched to the transmit one; we assume that the cascade of $p(t)$ and $p^*(-t)$ satisfies the Nyquist criterion for the absence of Inter Symbol Interference (ISI) at the proper sampling time instants with period T/N.

Sampling the received signal at $t = lT + mT/N$ the received samples are obtained. Omitting the noise terms for simplicity, we obtain:

$$\begin{aligned}
z_l[m] &= z\left(lT + m\frac{T}{N}\right) \\
&= \sum_k \sum_{i=0}^{N-1} a_k[i] q(lT + m\frac{T}{N} - kT - i\frac{T}{N}) \\
&= \sum_k \sum_{i=0}^{N-1} a_k[i] q\left([(l-k)N + (m-i)]\frac{T}{N}\right) \\
&= \sum_k \sum_{i=0}^{N-1} a_k[i] q[(l-k)N + m - i] \qquad i = 0, .., N-1 \qquad (3.4)
\end{aligned}$$

where the samples of $q(t)$ at T/N are denoted as $q[j] = q(j\frac{T}{N})$. Note that, considering an ideal channel, i.e., $q[j] = \delta[j]$, (3.4) presents only one term different from zero for $k = l$ and $m = i$, so that the received sample is $z_k[i] = a_k[i]$ and ideal communication is performed. In this case, perfect recovery of the modulation symbols can be achieved, i.e.,

$$\begin{aligned}
Z_l[m] &= \mathrm{DFT}\{z_l[i]\} \\
&= \frac{1}{\sqrt{N}} \sum_{n=0}^{N-1} a_l[i] W_N^{-ni} \\
&= A_l[i] \qquad i = 0, .., N-1.
\end{aligned}$$

3.3 Time-Domain Echo Cancellation

In Chapter 2, the Least Mean Square (LMS) algorithm for the echo cancellation in a single carrier powerline modem is discussed and the cost function

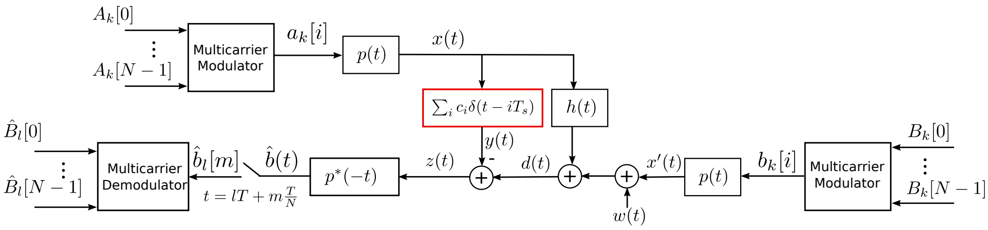

Figure 3.3: Continuous-time scheme for echo cancellation in a multi-carrier system.

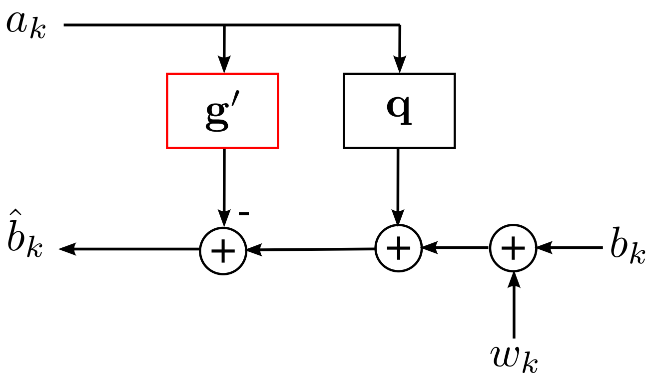

Figure 3.4: Discrete-time scheme for time-domain echo cancellation.

to be minimized is derived, starting from a continuous-time model of the analyzed system, which is depicted in Figure 2.2. Considering a multi-carrier system, the time-domain echo cancellation can be analyzed referring to the continuous-time model in Figure 3.3. The sampling time of the FIR filter is $T_s = T/(NN_u)$, where T/N is the period of the OFDM time-domain symbols and N_u is the oversampling factor.

The uncorrelation between the symbols inside the k-th OFDM block holds as long as the OFDM guard interval is not considered and the symbols $\{A_k[n]\}_{n=0}^{N-1}$ are uncorrelated and have the same power for $i = 0, ..., N-1$. The presence of a guard interval, inserted to avoid the ISI between OFDM symbols for transmission over a finite dispersion channel, introduces a correlation between some of the k-th OFDM block symbols. This aspect will be the subject of further investigations. One can see that, if the OFDM symbols $a_k[i]$ are assumed as uncorrelated (for every $k \in \mathbb{N}$ and $i \in [0, N-1]$), the formulation of the LMS algorithm and its cost function are the same as those derived in Section 2.3 for the single carrier powerline modem. In fact, the discrete-time version of the scheme in Figure 3.3, for the time-domain echo cancellation analysis, is the same as the one derived in Section 2.3 and depicted in Figure 3.4, where w_k denotes the complex AWGN samples, $\mathbf{g}'$ contains the samples of the filtered version of the cascade of the transmit and receive filters, i.e., $g'_j = \sum_{i=0}^{C-1} c_i g_{j-i}$, and $\mathbf{q}$ contains the samples of the overall impulse $q(t)$.

Let us abandon the double-index notation used in (3.1) and (3.4), as we are now considering OFDM symbols in place of OFDM blocks. We denote the transmitted samples $a_k[i]$, represented in Figure 3.2, as a_k where the index k is now the symbol index. Note that the sampling period of the samples a_k is T/N. Similarly, we denote by b_k the symbols of OFDM blocks transmitted by the remote modem. The adaptation algorithm is then given by (2.39).

3.4 Performance Analysis

The sequences $\{a_k\}$ and $\{b_k\}$ are obtained as the output of a multi-carrier modulator described in Section 3.2, which generates 16-QAM independent symbols over $N = 64$ carriers. Numerical results show that the echo cancellation process, for the proposed system, is not influenced by the number N of independently modulated carriers. The sampling period of the symbols $\{a_k\}$ and $\{b_k\}$ is $T/N = 1/f$, as depicted in Figure 3.2, and f is set, for example, to 12.8 kHz, in order to compare the multi-carrier system performance with a single carrier system which transmits the information symbols at a rate equal to $f_{symb} = 12.8$ kHz. Note that, considering $f = 12.8$ kHz and $N = 64$, the 16-QAM symbols at the input of each sub-carrier of the multi-carrier modulator are provided at a rate equal to $1/T = f/N = 200$ Hz. The energy per time-domain symbol E_s is set to unity. The LMS algorithm is implemented for the adaptive FIR filter of the echo canceller with $\mu = 10^{-7}$.

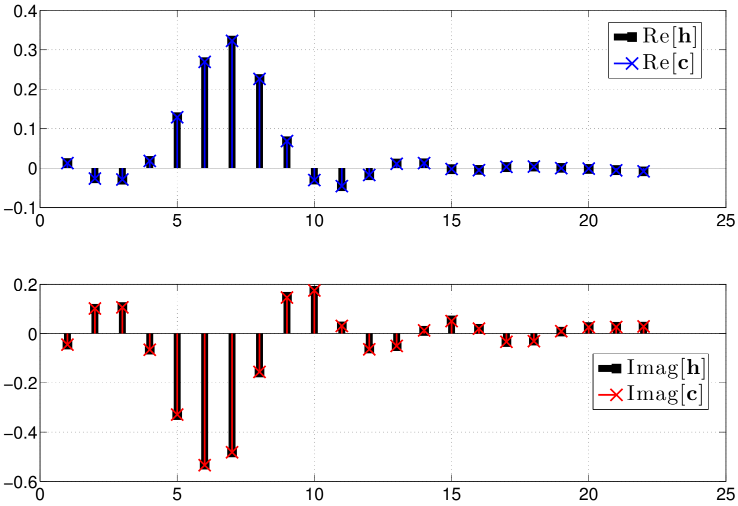

Figure 3.5: Echo channel response and filter weights for SNR = 10 dB.

Figure 3.5 shows the echo channel impulse response **h** and the weight vector **c**, at convergence, for a Signal-to-Noise-Ratio (SNR) equal to 10 dB. One can note that the adaptive filter reproduces exactly the echo response, as the LMS optimal solution is represented by the echo response. The time-domain echo cancellation process in the analyzed multi-carrier system is then confirmed to be the same as that discussed in the case of the single carrier system in Chapter 2.

Echo cancellation performance is also analyzed in terms of Bit Error Rate (BER) and Symbol Error Rate (SER), shown in Figure 3.6 and Figure 3.7, respectively, for the single carrier and the multi-carrier systems. The energy per transmitted bit is denoted by E_b and the curve tagged as “AWGN” is relative to the performance of a point-to-point communication system over AWGN channel for a 16-QAM modulation format. As expected, the system reliability is also equal for both single carrier and multi-carrier systems.

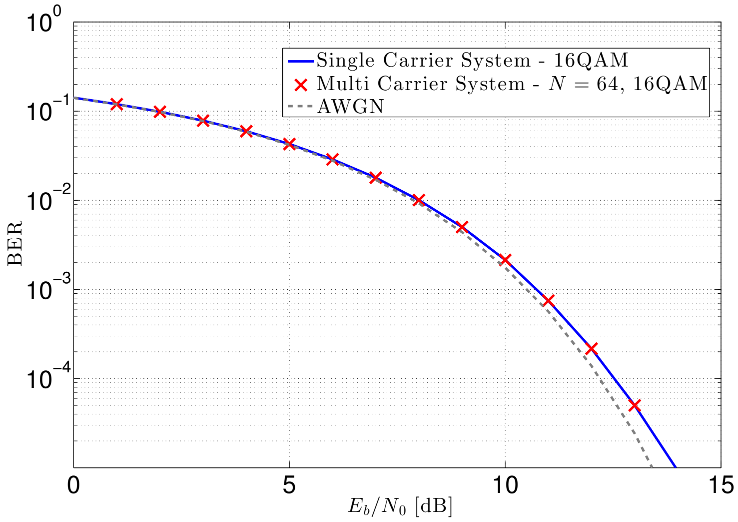

Figure 3.6: BER for a single carrier system and the analyzed multi-carrier system.

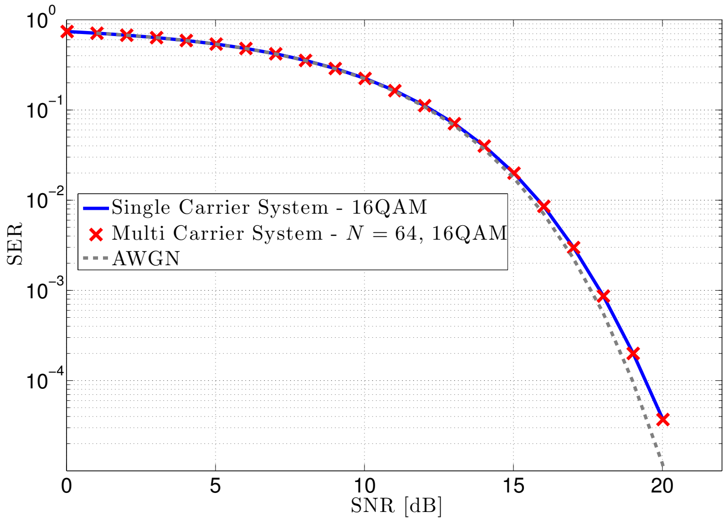

Figure 3.7: SER for a single carrier system and the analyzed multi-carrier system.

3.5 Conclusions

In this Chapter we described the DFT-based implementation of a multi-carrier system in which N independent M-QAM symbols are modulated over N independent carriers. We discussed the possibility to perform the echo cancellation in the PLC system described in Chapter 2 considering the OFDM modulation format. As long as the transmitted symbols are uncorrelated, the time-domain echo cancellation can be performed, operating in the time domain, in the same manner as it is performed in a single carrier system.

Simulation results on the system reliability show that there is no difference, in terms of echo cancellation performance, of the proposed multi-carrier system with respect to the single carrier one.

Chapter 4

Fixed-point LMS Algorithm for Echo Cancellation

4.1 Introduction

A Digital Signal Processor (DSP) [42] has a limited number of bits available to represent floating-point numbers, so that the accuracy of the performed operations is related to the finite representation precision. Numbers in DSP are usually represented by means of the fixed-point format, which is less computationally demanding with respect to the floating-point representation. Also, most processors do not have the unit, which manages floating-point operations. Because of their recursive nature, adaptive algorithms, such as the Least Mean Square (LMS) algorithm adopted for echo cancellation, may significantly suffer from a poor representation accuracy, which may lead to a poor coefficient updating.

In this chapter, we discuss the fixed-point representation adopted for the real world implementation of digital signal processing algorithms in a DSP. In particular, we discuss the fixed-point implementation of a Finite Impulse Response (FIR) filter and its application in the echo canceller discussed in Chapter 2, based on an adaptive FIR filter. We then analyze the performance of the fixed point echo canceller for both the single-carrier and multi-carrier PLC systems discussed in Chapters 2 and 3, respectively.

This chapter is organized as follows. In Section 4.2, we discuss the method adopted to represent numbers as fixed-point quantities in a DSP. In Section 4.3, the implementation of a generic FIR filter in the fixed-point domain is described and possible causes of error, related to the limited number of bits at the DSP disposal, are discussed. In Section 4.4, we describe the fixed-point implementation of the Least Mean Square (LMS) algorithm for echo cancellation purposes. In Section 4.5, simulation results are presented and the problems related with the fixed-point implementation of the algorithm are analyzed and discussed. Finally, in Section 4.6, final remarks are given.

4.2 Fixed-point Representation

Fixed-point notation is used to represent numbers in DSP, which have a finite number of bits available to perform operations [5, 43, 44, 45]. Denoting as B the wordlength adopted for the fixed-point representation, i.e. the available number of bits, the meaning of a B-bit binary word depends entirely on its interpretation. A B-bit fixed-point number can be interpreted as either an integer number or a fractional number, according to the position of the point.

A common interpretation of fixed-point numbers in digital signal processing, is the fractional representation, also known as Q-format [5, Chap. 13]. In Q-format, the Most Significant Bit (MSB) is the sign bit and each representable number belongs to the range $[-1, 1)$ or, more precisely, $[-1, 1 - 2^{-(B-1)}]$. The quantity $2^{-(B-1)}$ is the resolution of the represented fractional number. The larger B, the smaller the resolution and, indeed, the better the fixed-point representation. For a 16 bit DSP, it is customary to use the Q15 representation, which uses 15 bits for the fractional representation of the number and 1 sign bit. For example, with 16 bits, in Q15 representation, it is possible to represent fractional numbers in the range $[-1, 0.999969482421875]$ with a resolution of $3.0517578125 \cdot 10^{-5}$.

Conversion of a number in the range $[-1, 1-2^{-(B-1)}]$ to its Q-format version can be performed by scaling the number by the factor $1/2^{-(B-1)} = 2^{(B-1)}$ and approximating it to an integer number. The approximation is referred to as quantization, since the number is actually being quantized in amplitude just as an Analog to Digital Converter (ADC) quantizes an analog input. The approximation can be performed by truncation or rounding of the fractional number scaled by $2^{(B-1)}$. A popular technique is to round the scaled result to the nearest integer, as such an operation does not introduce any downward or upward biases, minimizing the approximation error. On the contrary, truncation (floor) or round up (ceil) approximations may introduce biases.

The fixed-point version of a number x, in the range $[-1, 1-2^{-(B-1)}]$, denoted as x^{Q}, is then obtained as

$$x^{\mathrm{Q}} = \mathrm{round}(x \cdot 2^{(B-1)}) \tag{4.1}$$

where round() denotes the rounding to the nearest integer operation, performed as

$$\mathrm{round}(\alpha) = \begin{cases} \lfloor \alpha + 0.5 \rfloor & \text{for } \alpha \geq 0 \\ \lceil \alpha - 0.5 \rceil & \text{for } \alpha < 0. \end{cases}$$

where $\lfloor \cdot \rfloor$ denotes the floor operation and $\lceil \cdot \rceil$ denotes the ceil operation. This definition of rounding to the nearest integer function allows positive elements with a fractional part of 0.5 to get rounded up to the nearest positive integer, while negative elements with a fractional part of -0.5 get rounded down to the nearest negative integer. For example, 23.5 is rounded up to 24, while -23.5 is rounded down to -24.

In the case of complex values, the conversion is performed independently on the real and the imaginary parts, i.e. if $z \in \mathbb{C}$

$$\begin{aligned} z^{\mathrm{Q}} &= \mathrm{round}(z \cdot 2^{(B-1)}) \\ &= \mathrm{round}[\mathrm{Re}(z) \cdot 2^{(B-1)}] + j \cdot \mathrm{round}[\mathrm{Im}(z) \cdot 2^{(B-1)}] \end{aligned}$$

where j denotes the imaginary unit.

The analog reconversion to the interval $[-1, 1)$ can be obtained as

$$\tilde{x} = x^{\mathrm{Q}}/2^{(B-1)} \tag{4.2}$$

where the reconverted analog value is denoted as $\tilde{x}$ since the rounding operation introduces an approximation. This approximation is known as the quantization error,[1] and depends on the resolution of the representation, i.e. it depends on B.

Hereafter, we adopt the Q-format fixed-point representation with rounding to the nearest integer approximation and various values of B for the representation of the various numbers. Also, as it is customary for fixed-point implementation of algorithms in some DSPs, we use $2^{(B-1)} - 1$ instead of $2^{(B-1)}$ as conversion scaling factor [46]. This choice can be justified by the following argument. Consider the format Q15 ($B = 16$), so that fixed-point numbers are representable by integers in the range $[-2^{(B-1)}, 2^{(B-1)} - 1]$, namely $[-32768, 32767]$. Setting, for example, $x = 0.999$, according to (4.1) one has $x^{\mathrm{Q}} = \mathrm{round}(0.999 \cdot 32767) = 32735$ which can be represented by 16 bits in Q15, but if x is still in the range $[-1, 1)$, but exceeds the representable range $[-1, 0.999969482421875]$ allowed by Q15 format, e.g., $x = 0.99999$, the resulting fixed-point representation in Q15 is $x^{\mathrm{Q}} = 32768$ which results in an overflow, since the Q15 format allows to represent signed integers between -32768 and 32767. An overflow is an unwanted phenomenon which occurs when the maximum wordlength admitted by a chosen arithmetic precision in a DSP for the representation of fractional numbers, i.e., the maximum number of bits at the processor disposal, is exceeded. Overflows may have catastrophic effects on an algorithm execution and must be avoided. Setting $2^{(B-1)} - 1$ as the scale factor, permits to avoid overflows, due to the attempt to represent out-of-range fractional numbers in $[-1, 1)$ and it does not represent a significant loss in representation resolution, as it just reduces the fixed-point range

---

[1] For a detailed discussion and quantification on the quantization error, we refer to [5, Chap. 13].

from $[-32768, 32767]$ to $[-32767, 32767]$.

Defining the conversion scale factor as

$$\triangle = 2^{(B-1)} - 1 \tag{4.3}$$

Equations (4.1) and (4.2) can be expressed as

$$x^{\mathrm{Q}} = \mathrm{round}(x \cdot \triangle) \tag{4.4}$$

and

$$\tilde{x} = x^{\mathrm{Q}} / \triangle. \tag{4.5}$$

4.3 Fixed-point FIR Filter Implementation

We now discuss the fixed-point implementation of an FIR filter. It is a common and basic type of filter in digital signal processing and understanding its fixed-point implementation and possible overflow causes is useful for the echo canceller fixed-point implementation hereinafter discussed, as the latter consists of an adaptive FIR filter.

Figure 4.1 depicts the FIR structure, where $\{x_k\}$ is the generic exact input sequence and $\{y_k\}$ is the output sequence. The N filter weights are denoted by $\mathbf{c} = \{c_i\}_{i=0}^{N-1}$. In order to implement the Q-format fixed-point FIR filter with B bits, its coefficients $\mathbf{c}$ and the input signal can be represented in Q-format. The output of the filter will be representable in Q-format with a larger number of bits, then it will be truncated to B.

As explained in Section 4.2, the Q-format allows to represent numbers in the range $[-1, 1)$, so that before the fixed-point conversion, the input and the coefficients must be scaled by a proper factor. Considering $|c_i| < c_{\max}$ $\forall i$, scaling the FIR weights as $\{c'_i\} = \{c_i / c_{\max}\}$ ensures they are in the proper range. For ease of presentation, the sum of the absolute values of the coefficients is considered to be normalized to 1, so that $c_{\max} < 1$ and the FIR weights do not require to be scaled. For the same reason, considering $|x_k| < x_{\max}$, the input

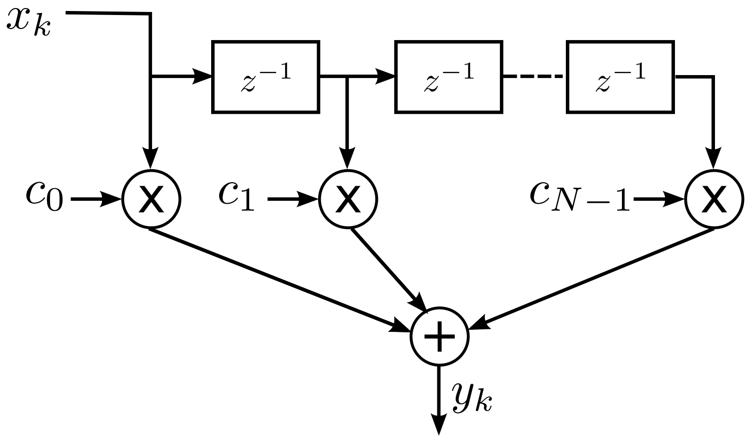

Figure 4.1: FIR structure.

must be $\{x'_k\} = \{x_k/x_{\max}\}$ in order to fit in the assigned range. Note that fixed-point conversion of the input can be interpreted as an analog to digital conversion operation and $(-x_{\max}, x_{\max})$ can be interpreted as the operating ADC dynamic range.

The Q-format representation of the input and the FIR tap, according to (4.4), are

$$\begin{aligned} x_k^{\mathrm{Q}} &= \mathrm{round}(x'_k \cdot \triangle) \\ c_i^{\mathrm{Q}} &= \mathrm{round}(c_i \cdot \triangle). \end{aligned}$$

The output $\{y_k\}$ of the FIR filter is given by the discrete-time convolution

$$y_k = \sum_{i=0}^{N-1} c_i x_{k-i} = \mathbf{c}^{\mathsf{T}} \mathbf{x}_k, \tag{4.6}$$

where $\mathbf{c} = (c_0, c_1, ..., c_{N-1})^{\mathsf{T}}$ and $\mathbf{x}_k = (x_k, x_{k-1}, ..., x_{k-N+1})^{\mathsf{T}}$.

The multiplication between two fixed-point numbers represented by B bits result in a number represented by $2B$ bits. This result must be temporarily stored in an accumulator with a proper capacity in terms of bits (at least

$2B$) in order to avoid overflows. A common size of the accumulator when Q15 format is adopted is 40 bits, that is 32 bits plus 8 "guard bits", to accomodate for the carries of the various adders. However, for $N < 100$ it appears that an accumulator of 32 bits is sufficient to store the multiplication result of two 16 bits numbers [5, Section 10.4.2.3].

The discrete convolution result represented by $2B$ bits must be brought back to the B bit representation by means of a right shift. Such an operation can be performed on the fixed-point number by scaling it by the factor $1/\triangle$ and is worth a numerical example. Setting $x = 0.72$ and $y = 0.35$, the product between the two analog numbers is $x \cdot y = 0.252$. Choosing the Q7 format, so that $B = 8$ bits are used for the fixed-point representation, the conversion scale factor given by (4.3) is $\triangle = 2^{(B-1)} - 1 = 127$. The fixed-point representation of x and y is then

$$\begin{aligned} x^{\mathrm{Q}} &= \mathrm{round}(x \cdot \triangle) = \mathrm{round}(0.72 \cdot 127) = 91 \\ y^{\mathrm{Q}} &= \mathrm{round}(y \cdot \triangle) = \mathrm{round}(0.35 \cdot 127) = 44. \end{aligned}$$

Both numbers x^{Q} and y^{Q} can be represented with 8 bits, since they are in the range representable by the Q7 format $[-127, 127]$. Their product is $91 \cdot 44 = 4004$, which exceeds the range and can be represented by 16 bits. Performing the right-shift in the fixed-point domain, one obtains

$$\mathrm{round}(x^{\mathrm{Q}} y^{\mathrm{Q}} / \triangle) = \mathrm{round}(4004/127) = 32$$

which can be again represented in Q7. The analog conversion (4.5) of the result is $32/127 \simeq 0.252$, meaning that 8 bits allow an accurate multiplication operation between 0.72 and 0.35. Note that adopting a Q3 format would have provided an analog reconversion of the result equal to about 0.2667, reflecting the presence of a quantization error due to the small number of bits available ($B = 4$).

The fixed-point output y_k^{Q} of the FIR implemented in the DSP is then

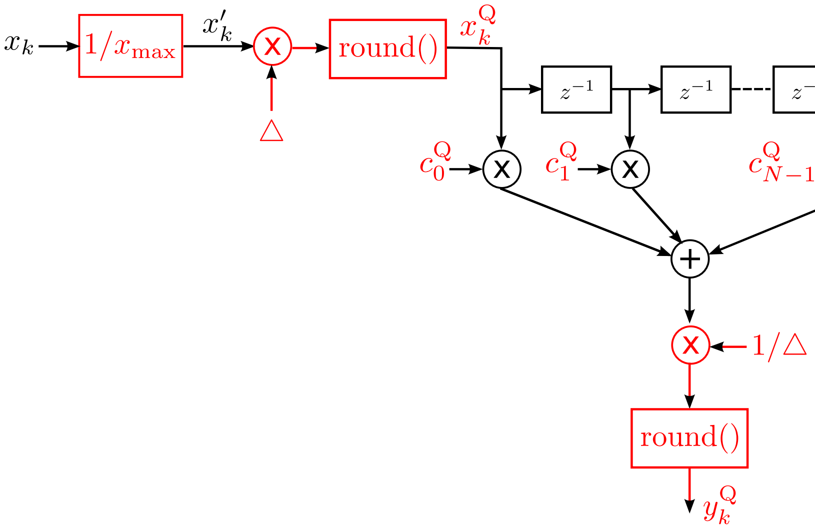

Figure 4.2: Fixed-point implementation of a FIR filter.

given by

$$y_k^{\mathrm{Q}} = \mathrm{round}[(\mathbf{c}^{\mathrm{Q}})^{\mathsf{T}}\mathbf{x}_k^{\mathrm{Q}}/\triangle] \tag{4.7}$$

and the fixed-point implementation of the FIR filter is shown in Figure 4.2. In order to convert y_k^{Q} to an analog number, one can apply (4.5) keeping into account the adopted scale factor, by means of a quantity denoted as G, so that

$$\tilde{y}_k = y_k^{\mathrm{Q}} \cdot G/\triangle. \tag{4.8}$$

Since the input was scaled by $1/x_{\max}$, the factor G must be set to $x_{\max}$, in order to correctly perform the analog reconversion.

In (4.6) one can see that additions after multiplications occur in the filtering operation. These operations can cause overflows, since y_k^{Q} may exceed the range $[-2^{(B-1)}, 2^{(B-1)} - 1]$, i.e., the analog version of y_k^{Q} exceeds the range $[-1, 1)$. In order to understand how these overflows may occur, let us evaluate the maximum FIR output amplitude.

We have to consider which combinations of N inputs will provide the maximum absolute value of the output, for a given N-tap FIR filter. In (4.6) one can see that when all the products $c_i x_{k-i}$ are concordant in sign, the output is a large value. This occurs when $\text{sign}(c_i) = \text{sign}(x_{k-i})$, so that the input which maximizes the absolute value of the contribution can be written as $\text{sign}(c_i) \cdot |x_{k-i}|$. The discrete convolution is then

$$\begin{aligned} y_k &= \sum_{i=0}^{N-1} c_i \text{sign}(c_i) \cdot |x_{k-i}| \\ &= \sum_{i=0}^{N-1} |c_i||x_{k-i}| \end{aligned}$$

where $\text{sign}(c_i)c_i = |c_i|$. The maximum possible output is obtained in the rare case in which every $|x_{k-i}|$ assumes its maximum value, so that, since $|x_k| < x_{\text{max}}$, one has

$$|y_{\text{max}}| < \sum_{i=0}^{N-1} |c_i| x_{\text{max}}$$

and defining $C = \sum_{i=0}^{N-1} |c_i|$, one has

$$|y_{\text{max}}| < C \cdot x_{\text{max}}. \tag{4.9}$$

In order to represent the input it must be scaled by $1/x_{\text{max}}$, so that the maximum output value obtained considering the input sequence as $\{x'_k\} = \{x_k/x_{\text{max}}\}$ is

$$|y_{\text{max}}| < C.$$

One can see that if $C > 1$, the filter output cannot belong to the range $[-1, 1)$ and overflows may occur, causing a representation error.

In general, overflows can be managed or prevented [5, 47]. For example, a technique adopted to manage overflows is *saturation*, that is when an overflow is detected, the value which caused it is clipped to its maximum allowed value. If overflows are not frequent and the value slightly overcomes the range limits, that is, the clipping operation does not introduce a significant degradation of the data, saturation may be acceptable. However, overflows prevention is often preferred. We now discuss two methods to prevent overflows on the FIR output due to the discrete convolution operation.

4.3.1 Scaling FIR Coefficients

In order to keep the fixed-point FIR filter output y_k^{Q} in the proper range and avoid overflow, the maximum analog value of the output must be $|y_{\max}| < 1$, which can be obtained scaling the FIR weights down by C. The new FIR weights are $c_i' = c_i/C$ and their fixed-point version are

$$(c_i^{\mathrm{Q}})' = \mathrm{round}(c_i' \cdot \triangle).$$

The analog version of the output is then given by (4.8) with $G = C \cdot x_{\max}$.

Scaling the FIR weights ensures that the overflows are prevented in the case of particular input vectors, which would cause a large output dynamic. The main disadvantage of this method is the requirement of knowledge of the FIR weights at the time of design, in order to identify the scaling factor C. Also, scaling down the filter coefficients may results in a significant reduction of their magnitude, which results in a reduced accuracy in the fixed-point representation for fixed B.

For completeness, we note that in case of multirate FIR filter implementaion by means of polyphase decomposition [4], the correct value of C is

$$C = \max\{C_0, C_1, ..., C_{N_u-1}\}$$

in which N_u is the oversampling factor and $C_j = \sum_{i=0}^{N/N_u-1} |c_i^{(j)}|$, where $\{c_i^{(j)}\}$ are the coefficients of the j-th polyphase component. Figure 4.3 shows the polyphase components of a pulse with square root raised cosine transform [6], with rolloff equal to 0.25 for $N_u = 2$ and $N = 128$. In this case the evaluated coefficient scale factors are $C_0 = 1.05$ and $C_1 = 1.29$, so that $C = 1.29$.

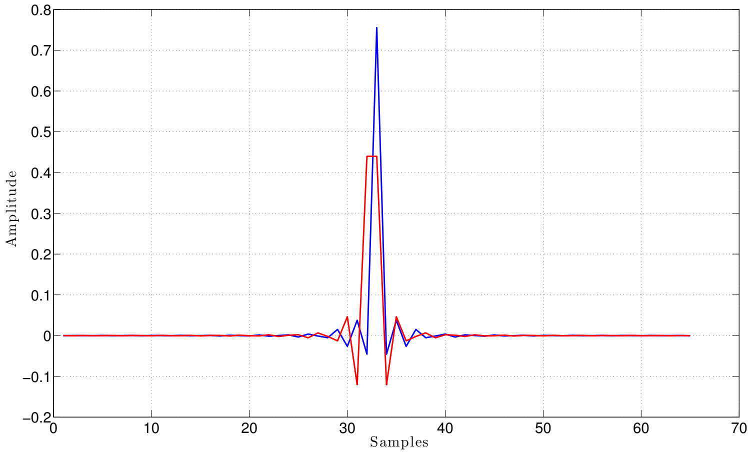

Figure 4.3: Polyphase components of a pulse with square root raised cosine transform with rolloff equal to 0.25 for $N_u = 2$ and $N = 128$.

4.3.2 FIR Coefficient Representation

Another method which would prevent overflows due to the convolution operation in the fixed-point FIR filter implementation, is to represent the coefficients with a smaller number of bits with respect to B. In this way, the accumulator is never filled with $2B$ bits. In [47] it is showed that the minimum number of bits B^{C} for the correct coefficients representation is

$$B^{\mathrm{C}} = \min\left(\left\lfloor \log_2(2^B - 1)/c_{\max} \right\rfloor, B^{\mathrm{acc}} - B - \lceil \log_2 C \rceil\right)$$

where B^{acc} is the accumulator capacity in terms of bits.

The implementation of this overflow prevention method does not require the a-priori knowledge of the FIR tap weights. However, it implies the use of different Q-formats inside the DSP for the FIR implementation.

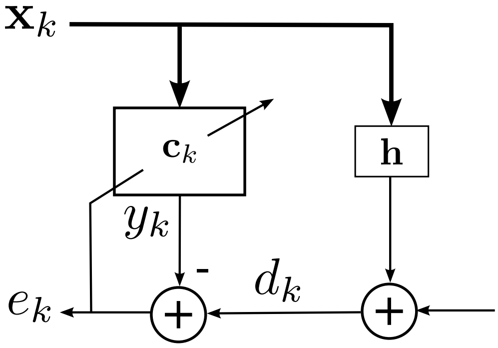

Figure 4.4: Echo canceller.

4.4 Fixed-point Implementation of LMS Algorithm

The LMS-based echo canceller discussed in Chapter 2 and depicted in Figure 4.4, can be implemented in fixed-point Q-format version. The input vector at sample instant k is $\mathbf{x}_k = (x_k, x_{k-1}, ..., x_{k-N+1})^\mathsf{T}$, the adaptive FIR tap vector is $\mathbf{c}_k = (c_0, c_1, ..., c_{N-1})^\mathsf{T}$, and the echo impulse response vector is $\mathbf{h} = (h_0, h_1, ..., h_{N-1})^\mathsf{T}$.

The LMS adaptive filter implemented in fixed-point requires the weight and input vectors $\mathbf{c}_k$ and $\mathbf{x}_k$, as well as the received signal d_k to be represented by a finite number of bits as discussed in Section 4.3. The recursive nature of the weight update algorithm causes an unlimited growth of the wordlength used for the fixed-point representation of $\mathbf{c}_k$, because of the multiplication operations involved. Of course this is unfeasible and some bits must be discarded before the weight vector is stored. A limited accuracy in the fixed-point representation, i.e., a small value of B, may introduce errors, which can cause the non-convergence of the algorithm or random fluctuations in the adaptive filter outputs.

Recalling the LMS weight update formula introduced in Chapter 2, one has

$$\mathbf{c}_{k+1} = \mathbf{c}_k + \mu \mathbf{x}_k^* e_k \tag{4.10}$$

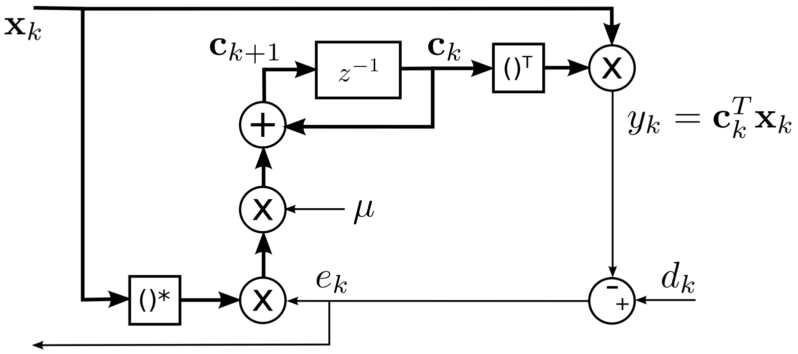

Figure 4.5: Echo canceller weight update.

where μ is the step size and $e_k = d_k - y_k$. In Figure 4.5, the echo canceller weight update process is depicted. In order to represent the echo canceller inputs x_k and d_k in Q-format, it must be $|x_k| < 1$ and $|d_k| < 1$, which can be obtained, as explained in Section 4.3, scaling properly the inputs by the factor[2] $\text{MAX} > \max\{x_{\max}, d_{\max}\}$, where $|x_k| < x_{\max}$ and $|d_k| < d_{\max}$. Assuming, for ease of presentation, $|x_k| < 1$ and $|d_k| < 1$, according to (4.4) and (4.3), the fixed-point inputs are

$$\begin{aligned} x_k^{\mathrm{Q}} &= \mathrm{round}(x_k \cdot \triangle) \\ d_k^{\mathrm{Q}} &= \mathrm{round}(d_k \cdot \triangle). \end{aligned}$$

As explained in Section 4.3, the multiplication between two fixed-point numbers doubles the result wordlength and a proper right-shift is needed. Referring to Figure 4.5, one can see that the weight update requires two product operations: the first between the conjugate of the input $\mathbf{x}_k^*$ and the error e_k, and the second between the result $\mathbf{x}_k^* e_k$ and the step size μ. Performing two multiplications and two consequent right-shifts may introduce too much degradation in the accuracy. Also, the fixed-point representation of the step size may be poor, as it may assume small values. A practical solution is to

---

[2] Note that ±MAX can be interpreted as the operating range of the ADC converter.

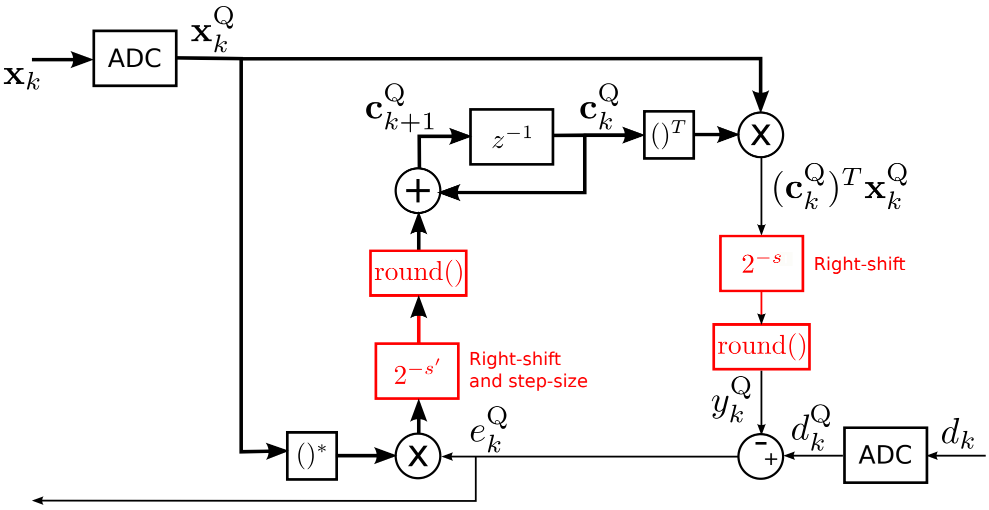

Figure 4.6: Echo canceller fixed-point implementation.

constraint the step size as a power of 2 and incorporate the relevant multiplication in the right-shift on the product between the input vector and the error signal, meaning that the shift operation not only discards the exceeding number of bits, but also performs the product by the fixed-point step size.

Figure 4.6 shows the fixed-point implementation of the echo canceller. The ADCs ideally perform the scaling by the factor MAX, if required, and the fixed-point conversions of the adaptive FIR inputs. The highlighted right-shift operations are performed as the product by a power of 2. In fact, with reference to the shift on the product $(\mathbf{c}_k^{\mathrm{Q}})^{\mathsf{T}}\mathbf{x}_k^{\mathrm{Q}}$, setting

$$s = \log_2 \triangle$$

one can see that $2^{-s} = 1/\triangle$. The fixed-point filter output is then obtained as

$$y_k^{\mathrm{Q}} = \mathrm{round}[(\mathbf{c}_k^{\mathrm{Q}})^{\mathsf{T}}\mathbf{x}_k^{\mathrm{Q}}/\triangle].$$

Defining the fixed-point step size as a power of two $\mu = 2^{-M}$, where $M > 0$

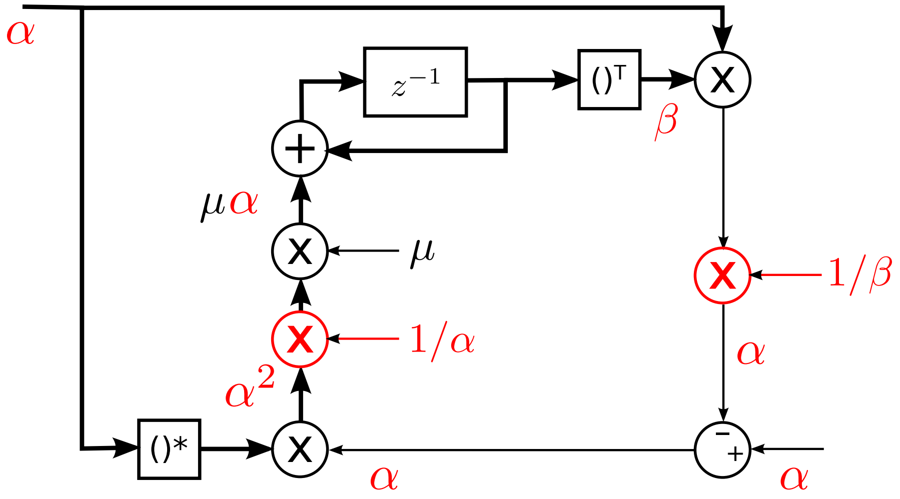

Figure 4.7: Generic scale factors in the echo canceller fixed-point implementation.

is an integer, and setting

$$s' = s + M \tag{4.11}$$

the right-shift and the product by the step size are performed on $(\mathbf{x}_k^{\mathrm{Q}})^* e_k^{\mathrm{Q}}$. The fixed-point weight update is then given by

$$\begin{aligned} \mathbf{c}_{k+1}^{\mathrm{Q}} &= \mathbf{c}_k^{\mathrm{Q}} + \mathrm{round}[(\mathbf{x}_k^{\mathrm{Q}})^* e_k^{\mathrm{Q}} \cdot 2^{-s'}] \\ &= \mathbf{c}_k^{\mathrm{Q}} + \mathrm{round}[(\mathbf{x}_k^{\mathrm{Q}})^* e_k^{\mathrm{Q}} \cdot 2^{-s} \cdot 2^{-M}] \\ &= \mathbf{c}_k^{\mathrm{Q}} + \mathrm{round}\left[\frac{(\mathbf{x}_k^{\mathrm{Q}})^* e_k^{\mathrm{Q}}}{\triangle} \cdot 2^{-M}\right]. \end{aligned} \tag{4.12}$$

4.4.1 Equivalent Step Sizes for Various Representations

In order to compare the echo canceller performance between its fixed-point implementation and the analog one, it is necessary to know the analog equivalent step size, related to the one chosen for the DSP implementation.

Let us refer to Figure 4.7, where the step size is $\mu = 2^{-M}$ and generic signal scale factor α and weight scale factor β are highlighted in the echo canceller block scheme. Note that $\alpha \neq \beta$ to account for different Q-formats for the representation of signals and filter gains, as it may be necessary for the reason discussed in Section 4.3.2. Denoting as α_A and α_B possible signal scale factors, and β_A and β_B possible weight scale factors, the corresponding step sizes μ_A and μ_B for equivalent performance are related by

$$\mu_A \alpha_A / \beta_A \quad = \quad \mu_B \alpha_B / \beta_B \tag{4.13}$$

leading to

$$\mu_A = \mu_B \frac{\alpha_B \beta_A}{\alpha_A \beta_B}. \tag{4.14}$$

For example, if the signal format chosen is Q15 and the weight format is Q7, the step size which entails a performance equivalent to that achieved in the case of Q15 format for both quantities is given by

$$\begin{aligned} \mu_A &= \mu_B \frac{\triangle_B^{\text{signal}} \triangle_A^{\text{weight}}}{\triangle_A^{\text{signal}} \triangle_B^{\text{weight}}} \\ &= \mu_B \frac{(2^{15}-1)(2^7-1)}{(2^{15}-1)(2^{15}-1)} \\ &= \mu_B \frac{(2^7-1)}{(2^{15}-1)}. \end{aligned}$$

It is important to note that, if $\alpha = \beta$, the step size does not change for different representations. In fact, from (4.14) one has

$$\begin{aligned} \mu_A &= \mu_B \frac{\alpha_B \alpha_A}{\alpha_A \alpha_B} \\ &= \mu_B. \end{aligned}$$

In order to evaluate the equivalent analog step size, note that the scheme depicted in Figure 4.7 becomes the one in Figure 4.8 in the case of analog LMS implementation, as the right-shifts are not needed and the weight vector is not scaled, i.e. $\beta = 1$. Denoting as μ_A the analog step size, α_A the signal

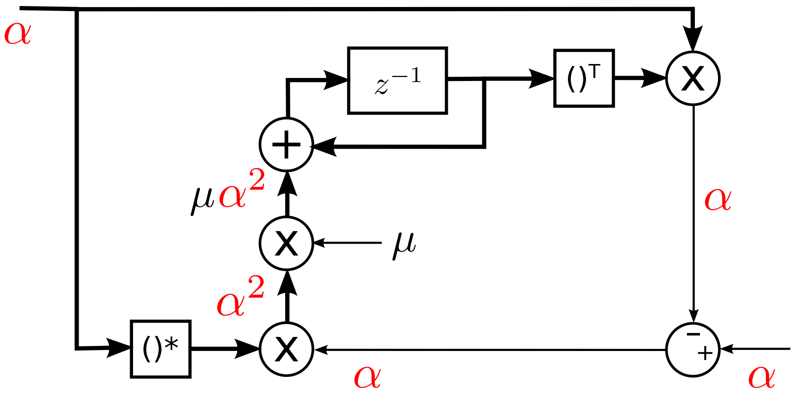

Figure 4.8: Generic scale factors in the echo canceller analog implementation.

scale factor in the analog implementation, which is equal to MAX, and α_B and β_B the scale factors for the Q-format implementation, (4.13) becomes

$$\mu_A \alpha_A^2 = \mu_B \alpha_B / \beta_B.$$

Setting $\mu_B = 2^{-M}$ and $\alpha_B = \beta_B = \triangle$, the (4.14) becomes

$$\mu_A = \frac{2^{-M}}{\text{MAX}^2}. \tag{4.15}$$

Equation (4.15) permits to convert to an analog value any given fixed-point step size, anabling the correct comparison between the performance of the echo canceller implemented in the DSP and the analog one.[3]

4.5 Fixed-point Echo Canceller Performance Analysis

We now present the performance achieved by the single-carrier and multi-carrier systems, described in Chapters 2 and 3, respectively, in which the echo

---

[3] Note that if the input signals are already normalized in the range $[-1, 1)$, that is $\text{MAX} = 1$, the analog step size is $\mu = 2^{-M}$.

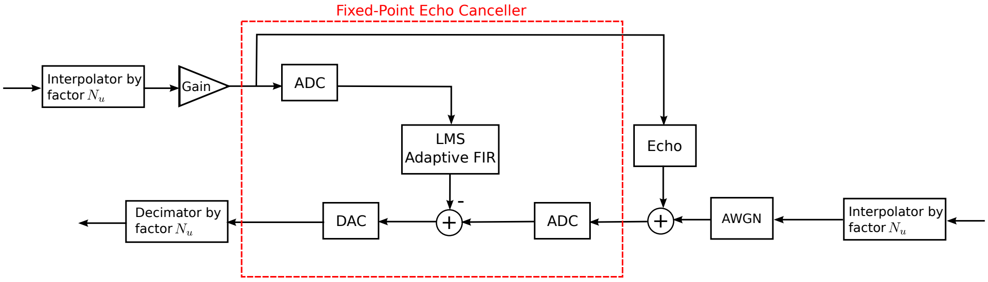

Figure 4.9: single-carrier system with fixed-point echo canceller.

cancellation is performed by a finite precision LMS filter. Problems related to the finite wordlength of DSP, which arise when the quantized weight update recursion is performed, are investigated, and possible solutions are discussed.

4.5.1 Fixed-point Echo Cancellation in single-carrier Systems

In Figure 4.9, the fixed-point echo canceller is highlighted. The blocks denoted as ADC ideally scale and quantize the input, performing the fixed point conversion (4.4), as described in Section 4.2. The block denoted as DAC, Digital to Analog Converter, ideally performs the fixed-point to analog conversion (4.8), where $G = \text{MAX}$. Note that the positions of ADCs and DAC in the scheme of Figure 4.9 do not reflect their actual positions in the real system, but represent just an expedient to clarify our discussion.

The following simulation results have been obtained for a 16-QAM modulation format, in the absence of AWGN, and for the same simulation settings described in Section 2.5. Given the echo response, the transmission length and the seeds for the generation of pseudorandom information sequences, the experimental largest sample amplitude measured at the input of the echo canceller is equal to $\simeq 101.17$, which is related to the amplitude of the QAM signal, the interfering path gain, and the amplitude gain possibly introduced by the echo channel. For this reason, we can consider the ADCs and DAC in Figure 4.9 to operate in the range $[-102, 102]$ and set the factor MAX, introduced in Section 4.4, equal to 102. This ensures the analog signals to be in the range $(-1, 1)$ before the fixed-point conversion.

Echo cancellation is performed by means of an LMS adaptive filter with N taps, whose fixed-point implementation is described in Section 4.4. The fixed-point step size $\mu_D = 2^{-M}$, where the subscript D stands for "Digital", is set for the largest value of M which provides a null Bit Error Rate (BER) in the absence of Additive White Gaussian Noise (AWGN). Our simulations show that this performance is achieved for $M = 8$. In order to compare the fixed-point LMS performance with the analog one, we use the following analog step size for equivalent performance according to (4.15)

$$\begin{aligned} \mu_A &= \frac{2^{-M}}{\mathrm{MAX}^2} \\ &= \frac{2^{-8}}{102^2} \\ &\simeq 3.7 \cdot 10^{-7} \end{aligned}$$

where the subscript A stands for "Analog".

Simulations have been performed for various values of B, i.e. various Q-formats. Given the described simulation settings, no overflows have been detected on any signal during all the simulations, so that no overflows management, nor prevention have been applied.

Figure 4.10 shows the MSE (2.24), with $\sigma_n^2 = 0$, for the analog system and for $B = 16$ and $B = 24$. The MSE analysis shows that 24 bits allow to obtain a performance comparable with that of the unquantized version, while a 16-bit wordlength causes a slowdown phenomenon as if the step size was smaller.

This behavior, observed in [48] and discussed in [49], is referred to as the LMS *stopping phenomenon*. The cause of such phenomenon lies in the quantized weight update recursion, given by (4.12). Let us express (4.12) in a more compact form, so that

$$\mathbf{c}_{k+1}^{\mathrm{Q}} = \mathbf{c}_k^{\mathrm{Q}} + \mathbf{g}_k^{\mathrm{Q}}$$

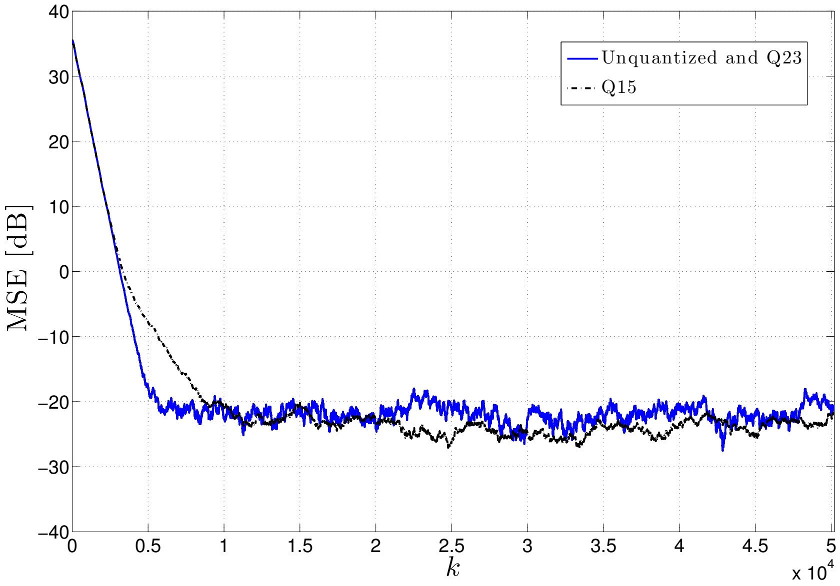

Figure 4.10: MSE for the analog system, denoted as "Unquantized", and for $B = 16$ and $B = 24$. The curves related to the unquantized version and the Q23 format are superimposed, therefore they are indicated in the legend as a unique curve.

where we have defined

$$\mathbf{g}_k^{\mathrm{Q}} = \mathrm{round}\left[\frac{(\mathbf{x}_k^{\mathrm{Q}})^* e_k^{\mathrm{Q}}}{\triangle} \cdot 2^{-M}\right]. \tag{4.16}$$

One can see that when the update quantity $\mathbf{g}_k^{\mathrm{Q}}$ is zero, the LMS is "stopped", in the sense that the algorithm does not update the weight vector. The quantity $\mathbf{g}_k^{\mathrm{Q}}$ may be zero if it is small enough to be rounded to zero for the given B. In other words, for fixed M, most of the time the quantity $\mathbf{g}_k^{\mathrm{Q}}$ may be zero for small values of B, stopping the update recursion and giving rise to the convergence slowdown observable in Figure 4.10. For example, for $M = 8$ and $B = 16$, $\mathbf{g}_k^{\mathrm{Q}}$ in (4.16) is composed of 8-bit signed values, which may result in null values, especially when e_k^{Q} is small. In fact, the significant slowdown in the convergence is more significant when the convergence is close to the steady-state, because in this situation, the value of the error e_k^{Q} is small. If $M = 8$ and $B = 32$, $\mathbf{g}_k^{\mathrm{Q}}$ is composed of 24-bit signed values, which may be very small for small e_k^{Q}, but still different from zero and representable with 24 bits.

In Figure 4.11, the trend of the quantity $||\mathbf{g}_k^{Q}||$ versus time is shown, for the unquantized implementation and for $B = 16$, 24, 32, with $M = 8$. One can see again that there is no significant difference between the unquantized implementation and the formats Q23 and Q31, while when the Q15 format is adopted, most of the time $||\mathbf{g}_k^{*}||$, i.e. the vector $\mathbf{g}_k^{\mathrm{Q}}$, is zero and the weight vector $\mathbf{c}_k^{\mathrm{Q}}$ is not updated. One can appreciate that peaks of $||\mathbf{g}_k^{Q}||$ under a certain magnitude are quantized to zero in Q15, meaning that values of the vector $\mathbf{g}_k^{\mathrm{Q}}$ are too small to be accurately represented with 16 bits. Moreover, as it is highlighted in the figure, not all of the peaks of $||\mathbf{g}_k^{Q}||$ with magnitude around the threshold under which they are not represented in Q15, are zero for $B = 16$. These non-zero peaks are caused by some values in the vector $\mathbf{g}_k^{\mathrm{Q}}$, large enough to be representable in Q15.

In [48], two major conclusions are given about the fixed-point implementation of the LMS. First, the steady-state MSE of the LMS digital implementa-

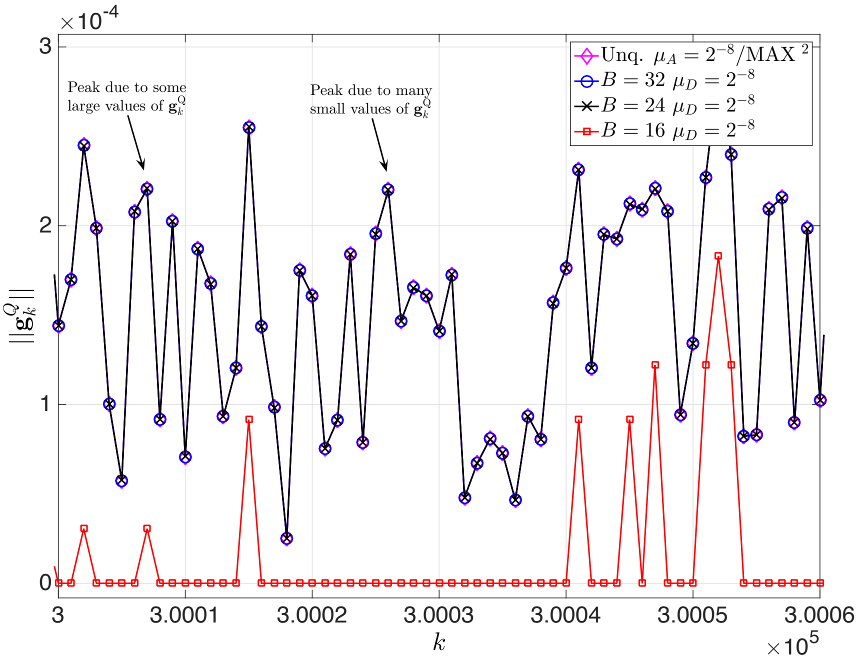

Figure 4.11: Quantity $||\mathbf{g}_k^Q||$ versus time for the unquantized implementation and for $B = 32$, 24, 16, with $M = 8$.

tion approaches the one obtained with an analog implementation for increasing values of B. Contrary to the analog case, the steady-state performance of the digital implementation does not exhibit improve monotonically with the step size, meaning that a reduction of μ_D beyond a certain value increases the steady-state MSE. The authors in [49] demonstrate that the steady-state MSE in a digital implementation eventually converges to the one obtained for infinite precision, but, because of the stopping phenomenon, the number of required iterations of the algorithm may become very large. This means that the quantization error has negligible effects on the MSE with respect to the stopping behavior. However, for small wordlength, i.e., $B \leq 8$, the convergence is not ensured with reasonable time.

As mentioned above, a major consequence of the stopping phenomenon is that reducing μ_D under a certain value, i.e., increasing M, degrades the echo cancellation performance, since the quality of the representation of $\mathbf{g}_k^{\mathrm{Q}}$ is reduced, as it is clear from (4.16). Furthermore, increasing μ_D beyond a certain value, i.e., decreasing M, deteriorates the steady-state MSE, leading to a non-zero BER in the absence of AWGN due to the algorithm instability. Therefore, the residual MSE exhibits a minimum for a certain M_0, whereas for $M < M_0$ and $M > M_0$ the performance degrades. This means that the chosen value of $M = 8$ for our simulations, not only is the first value which provides a zero BER in the absence of AWGN, but, as it will be shortly confirmed, it is also the only one, since $M = 7$ would cause significant fluctuation of the MSE around its steady-state value, and $M = 9$ would cause an excessive slowdown in convergence speed because of the stopping phenomenon.

4.5.2 Countermeasures Against the Stopping Phenomenon

In order to quantify the time percentage in which the LMS is stopped, it is possible to define the stopping rate ε as

$$\varepsilon = \frac{\sum_k I_k}{K} \cdot 100 \tag{4.17}$$

LMS Version	ε
$B = 32$, $M = 8$	$8 \cdot 10^{-4}$ %
$B = 24$, $M = 8$	$2.8 \cdot 10^{-3}$ %
$B = 16$, $M = 7$	73 %
$B = 16$, $M = 8$	81.7 %
$B = 16$, $M = 9$	99.4 %

Table 4.1: The stopping rate ε for $B = 32$, 24, 16 and for different values of M.

where K is the transmission length in symbols and I_k is an indicator function defined as

$$I_k = \begin{cases} 1 & \text{if } ||\mathbf{g}_k^Q|| = 0 \\ 0 & \text{else.} \end{cases}$$

Table 4.1 summarizes the obtained values of ε for $K = 10^6$, reflecting the presence of the stopping phenomenon when $B = 16$. Moreover, one can appreciate that for $M = 9$ the stopping phenomenon dramatically occurs, leading the LMS to be stopped for 99.4 % of the time. For $M = 7$, the LMS is stopped for a smaller time percentage, but the performance is unacceptable, as our simulations shows that the BER in the absence of AWGN is non zero.

The only really efficient countermeasure against the stopping phenomenon is the wordlength extension, i.e., adopting a larger value of B, so that $\mathbf{g}_k^{\mathrm{Q}}$ may be more finely represented and non zero almost all the time.

If the DSP has few bits at its disposal, solutions which attempt to speed up the convergence transient period can be proposed. In order to cope with the stopping phenomenon, the update algorithm has to be "kept alive" avoiding the weight update quantity $\mathbf{g}_k^{\mathrm{Q}}$ to be zero. A solution may consists in adding noise with a certain variance to the echo canceller desired input signal d_k^{Q}, in order to keep the error e_k^{Q}, and consequently $\mathbf{g}_k^{\mathrm{Q}}$, different from zero. For example, considering $B = 16$ and $M = 8$ and performing this kind of noise injection by adding quantized samples of circular Gaussian noise with variance

$\sigma_w^2 = 2.5$ to the desired signal, the stopping rate can be reduced to 30.9 %, which corresponds to a reduction of about 50 percent with respect to the original case. Note that adding independent Gaussian noise samples with $\sigma_w^2 = 2.5$ on the desired signal, is equivalent to consider an AWGN physical channel introducing noise with signal-to-noise-ratio $E_s/N_0 \simeq -3.98$ dB, for 16-QAM transmitted symbols with average power normalized to 1. Considering the gain on the interfering path of about 32.5 dB, this means that the interfering signal level is about 28.5 dB over the noise.

An alternative and more controllable low-complexity solution to cope with the convergence slowdown, consists in increasing the weight vector during the convergence transient period, modifying the weight update so that

$$\mathbf{c}_{k+1}^{\mathrm{Q}} = \mathbf{c}_k^{\mathrm{Q}} + \mathbf{g}_k^{\mathrm{Q}} + \mathrm{sign}(\mathbf{g}_k^{\mathrm{Q}}). \tag{4.18}$$

Note that, since sign(0) = 0, the stopping rate ε of the proposed solution dose not change with respect to the original version. This means that the stopping phenomenon is not reduced, but the weight update is “boosted” by the addition of a term which depends on the sign of $\mathbf{g}_k^{\mathrm{Q}}$ during the convergence period, making it possibly faster. This weight gain is applied also during the adaptation operated in the steady-state regime. The effects of the modified weight update in (4.18) are, therefore, similar to those caused by a larger step size in the standard fixed-point implementation (4.12), but our results prove that the performance degradation is not significant as they would be if M was smaller.

Figure 4.12 shows the MSE, confirming the possibility to cope with the convergence slowdown by the application of the weight gain algorithm. The curve related to the noise injection solution is not shown, as in this case the MSE converges to a value related to the additive noise variance, as it is demonstrated in Chapter 2. One can see that a larger step size, obtained for $M = 7$, allows the convergence to be faster, as it would be in the infinite precision case with a larger step size, but fluctuations around the steady state are large. The

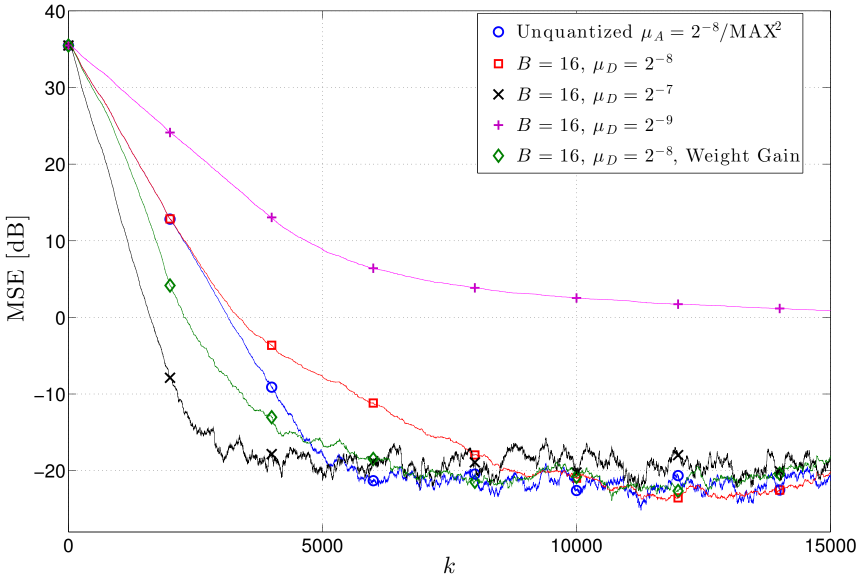

(a) Convergence

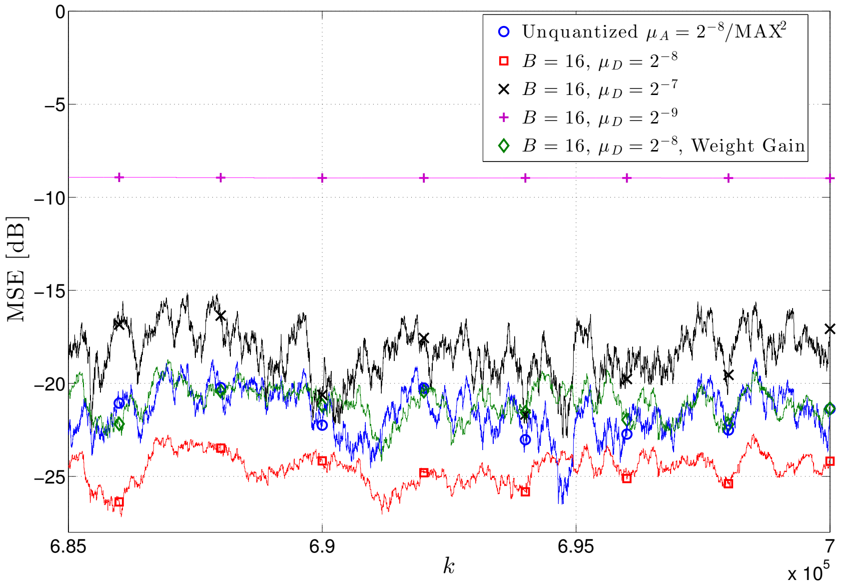

(b) steady-state

Figure 4.12: MSE for the unquantized LMS version, for $B = 16$ with different values of M and for weight gain algorithm: (a) convergence transient period and (b) steady-state regime.

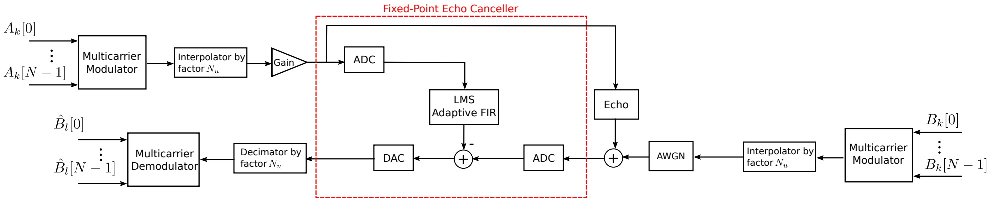

Figure 4.13: multi-carrier system with fixed-point echo canceller.

weight gain solution provides a faster convergence during the transient period and exhibits restrained fluctuations around the steady-state value of the MSE, meaning that the convergence slowdown is overcome without algorithm stability degradation. Also, one can appreciate the effects of the stopping phenomenon, for which a unique value of M which provides the minimum residual MSE exists. In fact, for $M = 7$ the steady-state MSE increases, with respect to the one obtained for the original finite precision LMS with $M = 8$, because of the algorithm instability, as it occurs in the unquantized case. For $M = 9$ the steady-state MSE significantly increases because of the weight update stopping preventing the algorithm to reach its optimal solution in a finite number of iterations.

4.5.3 Fixed-point Echo Cancellation in multi-carrier Systems

Echo cancellation for a multi-carrier system with Orthogonal Frequency Division Multiplexing (OFDM) modulation was reviewed in Chapter 3. The discrete-time scheme is depicted in Figure 4.13, where the fixed-point echo canceller, described in Section 4.5.1, is highlighted.

The frequency-domain transmitted symbols at the input of the multi-carrier modulator $A_k[n]$ and $B_k[n]$ are modulated by means of a 16-QAM format. The number of subcarriers is set to 256 and no cyclic-prefix is added for the present discussion. In fact, our simulations show that the presence of cyclic-prefix does not affect the fixed-point echo cancellation performance, as well as the analog one. The other simulation settings are the same as those discussed in Section 3.4.

The main difference with the single-carrier system is the amplitude of the signals at the ADCs input. The crest factor of OFDM modulated signal is much higher than that of a QAM modulated signal [33, 50].

This amplitude difference influences on the parameter MAX, i.e., on the ADCs and DAC operating range. The experimental largest sample amplitude measured at the input of the echo canceller is now equal to $\simeq 152.09$, which is related to the amplitude of the OFDM signal, the interfering path gain, and the amplitude gain possibly introduced by the echo channel. For this reason, MAX is set to 153, which is larger than that adopted in Section 4.5.1, equal to 102. It is then clear that the preliminary scaling operation, performed by the ADCs on the echo canceller input, is critical, since small numbers become smaller if scaled down by a larger factor. This means that the accuracy provided by a certain Q-format for the single-carrier system, may be insufficient for the multi-carrier system.

We set $M = 8$, since this value, also for the multi-carrier system, is the only one which allows to obtain a null BER in the absence of AWGN. In order to make the correct performance comparison with the unquantized system, according to (4.15) the analog step size is

$$\begin{aligned} \mu_A &= \frac{2^{-M}}{\mathrm{MAX}^2} \\ &= \frac{2^{-8}}{153^2} \\ &\simeq 1.6 \cdot 10^{-7} \end{aligned}$$

which is slightly different from the one obtained in Section 4.5.1, but is in the same order of magnitude.

Figure 4.14 shows the MSE for the analog system, for $B = 16$ and $B = 24$, and for the weight gain algorithm. One can see that the Q23 format is sufficient to provide a performance comparable with that of the unquantized system, as it happens for the single-carrier system. Also, the Q15 format heavily suffers from the stopping phenomenon and the application of the weight gain dis-

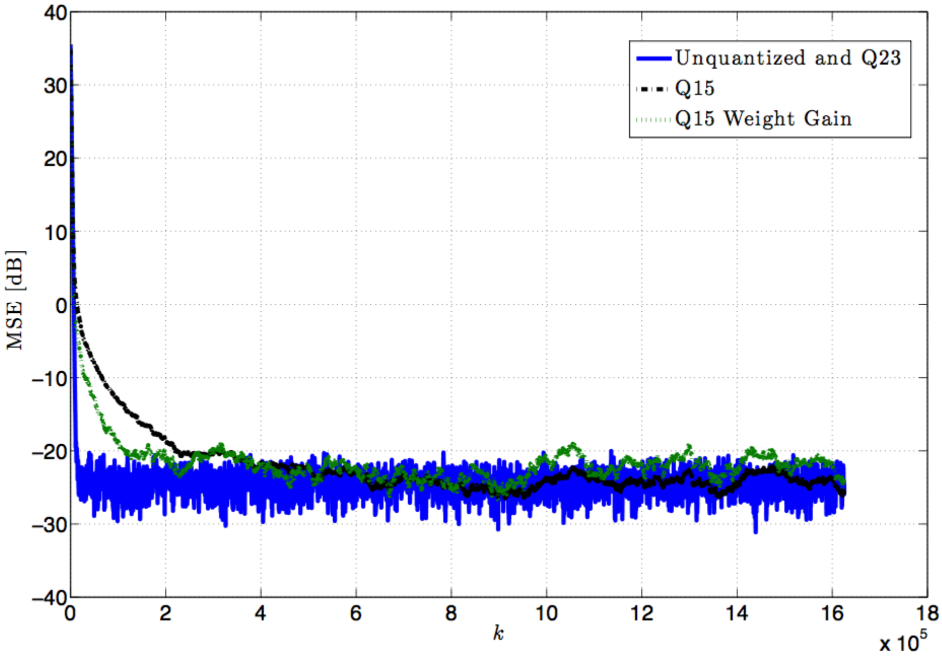

Figure 4.14: MSE for the unquantized system, for $B = 16$ and $B = 24$, and for the weight gain algorithm. The curves related to the unquantized version and the Q23 format are superimposed, therefore they are indicated in the legend as a unique curve.

cussed in Section 4.5.2 does not improve the convergence speed as it does in the single-carrier system. It can be concluded that for the multi-carrier system, Q23 may be the preferable DSP format in order to obtain an echo cancellation performance comparable with that of the unquantized system.

4.6 Conclusions

In this chapter, we discussed the fixed-point implementation of the LMS-based echo canceller, providing a general framework. We then carried on the MSE analysis for single-carrier and multi-carrier communication systems. The analysis showed that quantized implementations of the LMS algorithm can suffer from the stopping phenomenon for small wordlength, which causes a convergence slowdown. This effect cannot be coped with by a larger step size and significantly deteriorates the steady-state value of the MSE. Moreover, because of the stopping phenomenon, step sizes smaller than a certain value do not provide a smaller residual MSE, since they reduce the representation quality of the weight correction quantity.

The stopping phenomenon can be dealt with by modifying the LMS algorithm, in order to increase the weight vector magnitude during the adaptation. This solution appears to be efficient and slightly invasive. However, the best countermeasure against the stopping phenomenon is the extension of the DSP wordlength.

The Q23 format, i.e., 24-bit wordlength, entails a performance comparable with that of the unquantized system for both single-carrier and multi-carrier systems. Furthermore, multi-carrier systems appear to be more sensitive to problems related to a small wordlength, such as 16 bits, which may be insufficient.

Chapter 5

Weight Reset LMS

5.1 Introduction

As it is clear from the discussion carried out in Chapter 2, the reliability of the communication link in state-of-the-art Power Line Communications (PLC) modems, in which digital echo cancelers are employed, is related to the stability of the channel conditions. In fact, a sudden channel variation may trigger a transient convergence period, during which the echo canceler and the channel equalizer adaptively converge to a new steady-state setting. Channel variations in PLC environments are typically due to switching events and maintenance operations on the line, which may cause abrupt line impedance variations [51].

We face the problem of the convergence period reduction and propose a novel modification of the Least Mean Square (LMS) algorithm, described in Chapter 2. The modified algorithm is based on (i) fast detection of the channel variation and (ii) subsequent optimized reinitialization of the filter weights. We show that this weight reset can be interpreted in terms of optimized positioning over a multidimensional sphere in the space spanned by the filter weight vector. We first evaluate the benefits, in terms of convergence time reduction, using the LMS algorithm. We then investigate the application of weight reset to the Variable-Step LMS (VSLMS) algorithm, outlined in Section 2.2.2. Fi-

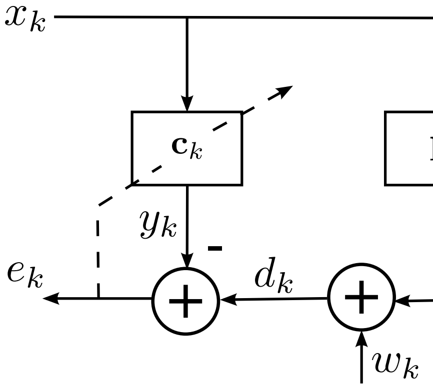

Figure 5.1: Discrete-time system model for channel identification.

nally, we apply the proposed algorithm to the realistic scenario of LMS-based echo cancellation in the single-carrier PLC system described in the previous chapters, also considering the presence of impulse noise.

This chapter is organized as follows. In Section 5.2, we review the LMS algorithm, introduce the novel weight reset strategy and discuss the extension to the VSLMS algorithm. In Section 5.3, we demonstrate the performance of the proposed strategy, considering both LMS and VSLMS algorithms for channel identification. In Section 5.4, the application of the weight reset algorithm to the case of echo cancellation in a PLC modem in the presence of abrupt channel variations and impulse noise is discussed. Concluding remarks are given in Section 5.5.

5.2 Weight Reset LMS Algorithm

We now review the LMS algorithm formulation, with reference to the simple discrete-time system model for channel identification depicted in Figure 5.1. Nonetheless, the weight reset strategy hereinafter described can be similarly employed in other applications of the LMS algorithm.

For ease of presentation, we repeat here the definitions given in the previous chapters. The transmitted sequence is denoted by $\{x_k\}$, the filter weights of the adaptive Finite Impulse Response (FIR) filter are denoted by the vector $\mathbf{c} = (c_0, c_1, ..., c_{N-1})^\intercal$, where N is the number of filter taps, $(\cdot)^\intercal$ denotes the transpose operator, and the channel response is denoted by $\mathbf{h} = (h_0, h_1, ..., h_{N-1})^\intercal$. The Additive White Gaussian Noise (AWGN) is represented by a sequence $\{w_k\}$, with zero mean, variance σ_w^2, and uncorrelated elements. The adaptive filter output is $y_k = \mathbf{c}^\intercal \mathbf{x}_k$, where $\mathbf{x}_k = (x_k, x_{k-1}, ..., x_{k-N+1})^\intercal$. The desired signal d_k is then obtained as $\mathbf{h}^\intercal \mathbf{x}_k + w_k$ and the error signal is defined as $e_k = d_k - y_k$.

The cost function to be minimized by the LMS algorithm is the MSE between the sequences $\{d_k\}$ and $\{y_k\}$, so that

$$\mathcal{E}(\mathbf{c}) = \mathbb{E}\{|d_k - y_k|^2\} \tag{5.1}$$

which, after standard manipulations, can be formulated as a quadratic form [20, 52].

The LMS weight update recursion [20] can be formulated as a stochastic gradient descent:

$$\mathbf{c}_{k+1} = \mathbf{c}_k + \mu \mathbf{x}_k^* e_k \tag{5.2}$$

where the subscript k, associated with the epoch, has been added to the weight vector $\mathbf{c}$ and μ is the step size parameter, whose value must be set as a compromise between stability around the optimal solution and convergence speed.

The weight vector $\mathbf{c}_k$ identifies a point in the N-dimensional complex space, which, because of the stochastic nature of the LMS algorithm, slightly fluctuates around the optimal solution $\mathbf{c}^{\text{opt}} = \mathbf{h}$. Note that the optimal LMS solution is not influenced by the AWGN in this channel identification problems, as discussed in Chapter 2. Hence, the weight update LMS algorithm converges to the same optimal solution, even in the presence of AWGN and regardless of the value of σ_w^2.

When a channel variation occurs, a convergence transient period is triggered, whose duration depends on the distance between the current weight vector, identified by the initial channel response $\mathbf{h}$, and its final value, which is identified by the new channel response $\mathbf{h}'$. The basic idea of the proposed weight reset strategy is that, when a channel variation is detected, a group of reinitialization vectors can be generated, some of which will likely be close to the final LMS optimal weights. The consequent sudden reset of the FIR tap weights to the vector closest to the final filter weight vector, may reduce the overall transient period.

The management of abrupt channel variations by the proposed algorithm, referred to as Weight Reset LMS (WRL), can be roughly summarized in terms of the following steps:

A) channel variation detection;

B) generation of a set of reinitialization points starting from the current weight vector and run of a number of parallel instances of the LMS algorithm;

C) after a properly set period, selection of the optimal reinitialization point as the one which may provide the shortest convergence time and stop of the remaining LMS instances.

We now detail these steps.

5.2.1 Channel Variation Detection

When a channel variation occurs, the LMS algorithm must adapt the weight vector. This causes a variation of the weight vector energy, defined at the k-th epoch as

$$E_k = ||\mathbf{c}_k||^2 \tag{5.3}$$

where $||\cdot||$ denotes the Euclidean norm. During the convergence transient period, the value of E_k will be subject to a variation, since the tap weights are adaptively changing. This behavior suggests that the channel variation can be detected by monitoring, time-wise, the trend of E_k. A channel variation is declared if the interval Δk, in terms of number of samples, needed to reduce or increase E_k by a fraction η of its current steady-state value E^*, is smaller

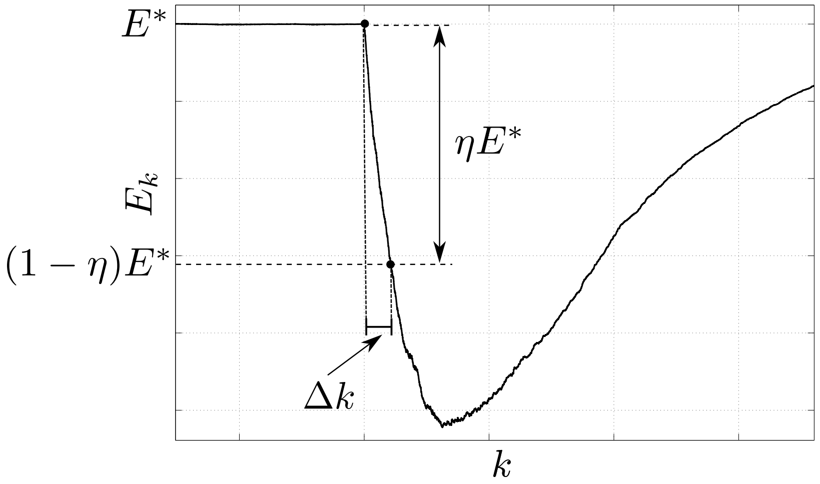

Figure 5.2: Pictorial representation of the instantaneous energy of the weight vector during an abrupt channel variation and the relevant interval Δk.

than a proper threshold k_{th}. In other words, an abrupt channel variation is identified by a non-negligible weight energy variation in a sufficiently short time interval. In Figure 5.2, the behavior of E_k, as a function of k, is shown during an illustrative abrupt channel variation at an arbitrary instant: the interval Δk is highlighted. Note that E^* can be estimated as the average value of E_k over a proper time window.

The value of the threshold interval k_{th} can be properly set by trial and error and can be considered as a parameter of the WRL algorithm which controls its "sensitivity," allowing to avoid the weight reset if not necessary. In fact, if the channel variation is mild, in the sense that the initial channel impulse response is close to that of the final one, the application of a weight reset may not provide a performance improvement as a small variation of E_k would be entailed. The smaller the threshold k_{th}, the lower the sensitivity of the WRL algorithm. It is, therefore, clear that the choice of k_{th} depends on the WRL application scenario.

5.2.2 Generation of Reinitialization Vectors

Before a channel variation, the current weight vector at the k-th epoch identifies an N-dimensional sphere of radius equal to $\sqrt{E_k}$, so that the reinitialization vectors can be chosen among a group of properly distributed points on the surface of this sphere. The basic principle to uniformly generate a group of points, starting from a given one (the weight vector initial position), is that every point must be equally spaced and at maximum distance from the neighboring ones. For simplicity, we also impose that the energy of the new reinitialization vectors is equal to the energy of the initial one. This corresponds to leaving the weight vector energy unchanged, as the channel energy variation is a-priori unknown. Future possible extensions of the weight reset strategy may involve a proper set of the reinitialization weight vector energy values, in order to roughly match that of the new channel response.

For ease of visualization and description, let us refer to the real 3-dimensional space $\mathbb{R}^3$: in this case, the initial point, denoted as $\mathbf{a} = (a_1, a_2, a_3)^\intercal$, corresponds to a 3-dimensional vector with real components. A simple method to generate points uniformly spaced, starting from $\mathbf{a}$, over the surface of the 3-dimensional sphere of radius $||\mathbf{a}||$, may be the identification of the intersections of the sphere with three orthogonal lines. Note that, besides the first point $\mathbf{a}$, the other intersections identify 5 points. This is equivalent to identifying the other 5 vertices of a regular Euclidean octahedron inscribed in the sphere of radius $||\mathbf{a}||$. The extension of this method to the real n-dimensional space $\mathbb{R}^n$ leads to the identification of $2n$ vertices of a hyper-octahedron, including the initial one. In the typical scenario of interest in digital communications, the extension to n-dimensional complex vertices in $\mathbb{C}^n$ leads to the identification of $4n$ vertices, as described in detail in the following paragraph (point 3).

We propose the following algorithm for the identification of the set of reinitialization points, starting from an initial position. Given a complex vertex $\mathbf{a}$, the other $4n - 1$ vertices of a hyper-octahedron in $\mathbb{C}^n$ can be determined by the following steps.

1. Define the matrix $\mathbf{P}$, of size $n \times n-1$, with $n-1$ column vectors $\mathbf{p}_j = (p_{1j}, p_{2j}, ..., p_{nj})^\intercal$ for $j = 1, ..., n-1$:

$$\begin{aligned} \mathbf{P} &= \begin{bmatrix} \mathbf{p}_1 & \mathbf{p}_2 & \cdots & \mathbf{p}_{n-1} \end{bmatrix} \\ &= \begin{bmatrix} p_{11} & p_{12} & \cdots & p_{1(n-1)} \\ p_{21} & p_{22} & \cdots & p_{2(n-1)} \\ \vdots & \vdots & \ddots & \vdots \\ p_{n1} & p_{n2} & \cdots & p_{n(n-1)} \end{bmatrix} \end{aligned} \tag{5.4}$$

where

$$p_{ij} = \begin{cases} a_i & \text{for } i = 1, ..., j \\ -\dfrac{\sum_{k=0}^{i-1} |a_k|^2}{a_i^*} & \text{for } i = j+1 \\ 0 & \text{else.} \end{cases} \tag{5.5}$$

This result can be easily obtained by imposing the orthogonality condition between two complex vectors ($\mathbf{z}, \mathbf{w} \in \mathbb{C}^n$ are orthogonal iff $\mathbf{z}^H \mathbf{w} = 0$).

2. Normalize every vector $\mathbf{p}_j$ ($j = 1, ..., n-1$) by the Euclidean norm of the initial vertex $\mathbf{a}$, that is, define the following matrix (in terms of its columns):

$$\mathbf{O} = \left[\frac{\mathbf{p}_1}{||\mathbf{p}_1||} ||\mathbf{a}|| \;\; \frac{\mathbf{p}_2}{||\mathbf{p}_2||} ||\mathbf{a}|| \;\; \cdots \;\; \frac{\mathbf{p}_{n-1}}{||\mathbf{p}_{n-1}||} ||\mathbf{a}|| \right].$$

3. The product of vector $\mathbf{p}_j$ by any of the four roots of the unit [53] $\{1, \jmath, -1, -\jmath\}$, being $\jmath$ the imaginary unit, preserves orthogonality. Therefore, the $4n$ vertices of the complex n-dimensional hyper-octahedron can be identified by the matrix $\mathbf{V}$, defined as

$$\mathbf{V} = [\; \mathbf{a} \;\; \mathbf{O} \;\; \jmath\mathbf{a} \;\; \jmath\mathbf{O} \;\; -\mathbf{a} \;\; -\mathbf{O} \;\; -\jmath\mathbf{a} \;\; -\jmath\mathbf{O} \;]. \tag{5.6}$$

The columns of $\mathbf{V}$ correspond, therefore, to the $4n$ vertices uniformly

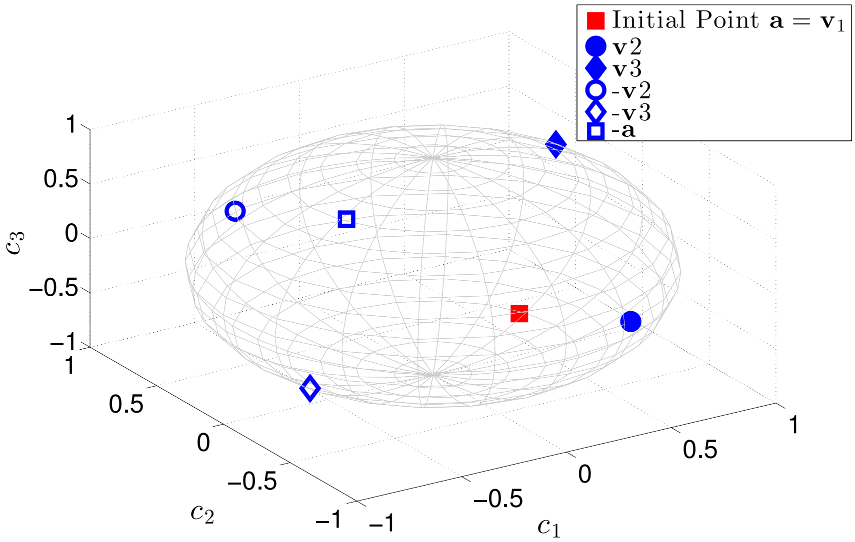

Figure 5.3: Vertices in $\mathbb{R}^3$ of the octahedron inscribed in the sphere with unit radius, given by the square-norm of the initial point $\mathbf{a} = (0.539, 0.199, -0.818)^\intercal$.

distributed over the n-dimensional hyper-sphere in $\mathbb{C}^n$.

As a visual example in $\mathbb{R}^3$, consider the initial vector $\mathbf{a} = (0.539, 0.199, -0.818)^\intercal$, with $||\mathbf{a}|| = 1$. In Figure 5.3, the $2n = 6$ vertices of the octahedron, obtained applying the aforementioned algorithm are shown, where $\mathbf{v}_j$ denotes the j-th column of $\mathbf{V}$ in (5.6).

5.2.3 Reinitialization Vector Selection

If $\mathbf{c}_k \in \mathbb{C}^N$, the weight vector lies on a hyper-sphere in $\mathbb{C}^N$, so that the matrix $\mathbf{V}$ given in (5.6) contains $4N$ reinitialization points. Once the channel variation has been detected as described in Subsection 5.2.1, $4N$ reinitialization points are generated, starting from the current weight vector. Then, $4N$ independent instances of the LMS algorithm can be run, each initialized with one of the column vectors of $\mathbf{V}$. Note that, since $\mathbf{V}$ contains also the initial weight vector, one of the instances corresponds to the standard LMS adaptation. We assume the parallel instances of the LMS algorithm to be run for L samples, so that the selection of the optimal point is performed L steps after the channel variation detection. The proper selection of L will be shortly discussed.

Since the optimal reinitialization point is the nearest to the final weight vector, it is also the one which, on the average, provides the minimum value of square error $|e_k|^2$. We now propose a method to select the optimal reinitialization point based on the evaluation of a proper mean square error signal, which is readily available for each instance of the LMS algorithm, averaged over a time window of proper length. In particular, we set this length to L samples, i.e., the duration of the parallel LMS run.

Considering a channel variation occurring at time instant $\tilde{k}$, after L steps the following matrix $\mathbf{S}$ is available[1]

$$\mathbf{S} = [\mathbf{s}_{\tilde{k}}, \mathbf{s}_{\tilde{k}+1}, ..., \mathbf{s}_{\tilde{k}+L}]$$

where $\mathbf{s}_{\tilde{k}} = (|e_{\tilde{k}}^{(1)}|^2, |e_{\tilde{k}}^{(2)}|^2, ..., |e_{\tilde{k}}^{(4N)}|^2)^\intercal$, being $|e_{\tilde{k}}^{(i)}|^2$, $i = 1, ..., 4N$, the square error signal associated with the i-th reinitialization point at epoch $\tilde{k}$. The average of these vectors, over a window of length L, is given by

$$\mathbf{m} = \frac{1}{L}\mathbf{S}\mathbf{u} \tag{5.7}$$

where $\mathbf{u}$ is a column vector of length L and unit entries. Therefore, the vector $\mathbf{m} = \{m_i\}_{i=1}^{4N}$ contains the estimates of the mean square error values associated with all potential reinitialization points, i.e.,

$$m_i = \frac{1}{L}\sum_{j=1}^{L}\left|e_{\tilde{k}+j}^{(i)}\right|^2 \quad i = 1, 2, ..., 4N. \tag{5.8}$$

The index of the optimal reinitialization point is identified by the smallest

---

[1] Although the matrix $\mathbf{S}$ depends on the time instant $\tilde{k}$, this dependence is not explicit for ease of presentation and because it is eventually irrelevant, as the matrix is computed only once, starting from the channel variation detection instant $\tilde{k}$.

element of $\mathbf{m}$, i.e.,

$$\hat{\imath} = \underset{i=1,2,\ldots,4N}{\operatorname{argmin}} \; m_i. \tag{5.9}$$

The optimal reinitialization point is then identified as the $\hat{\imath}$-th column of $\mathbf{V}$, i.e., $\mathbf{v}_{\hat{\imath}}$.

It is now of interest to analyze the time L needed for the optimal reinitialization point selection. It may be intuitively expected that the choice of the value of L depends on the number of the filter taps N, as the LMS convergence speed is also related to the length of $\mathbf{c}_k$: in other words, the larger N, the slower the adaptation process. To ensure the convergence of all of the elements of the vector $\mathbf{m}$ in (5.7), the larger N, the larger the value of L should be. The optimized value of L can be set by trial and error. As an example, referring to the channel identification scenario introduced in Section 5.2, Figures 5.4 and 5.5 show the elements of $\mathbf{m}$, given in (5.7), as functions of L, obtained for abrupt channel variations between random complex channel responses, for $N = 5$ and $N = 10$, respectively. In both Figures 5.4 and 5.5, subfigures (a) and (b) show the results obtained for two different channel variations. One can see that, after a certain period, the average square errors related to every reinitialization point (20 for $N = 5$ and 40 for $N = 10$) converge and the optimal reinitialization point can be selected. According to Figure 5.4, $L = 30$ and $L = 50$ appear to be suitable for $N = 5$ and $N = 10$, respectively. In particular, the closest point corresponds to the minimum value of $\mathbf{m}$ and is selected as the optimal reinitialization point. Moreover, one can note that, as expected, some of the reinitialization points provide large average square errors, as they are evidently the farthest points over the hyper-sphere, with respect to the final point, while the closest one provides small average square error. In every figure, the curve associated with the optimal reinitialization point is highlighted as a dashed line.

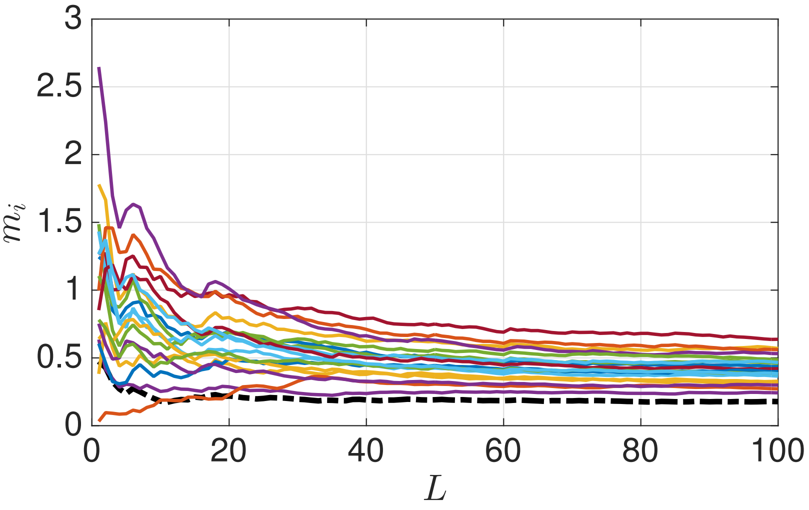

(a)

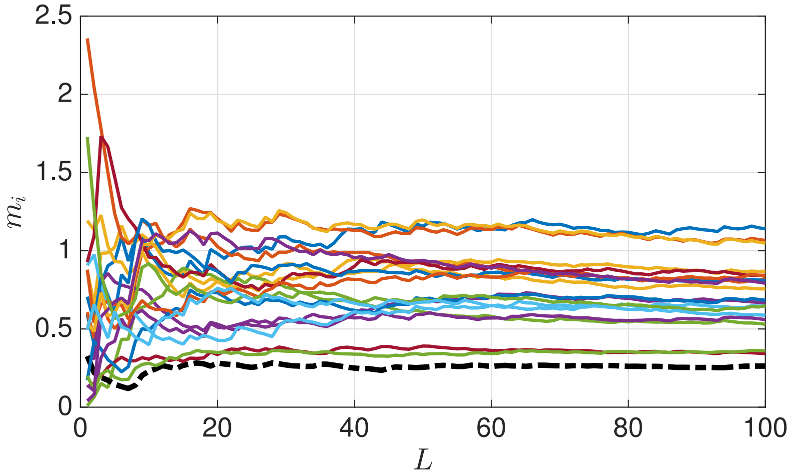

(b)

Figure 5.4: Values of $\{m_i\}$ as functions of L (each curve corresponds to an element m_i, $i = 1, ..., 4N$): $N = 5$.

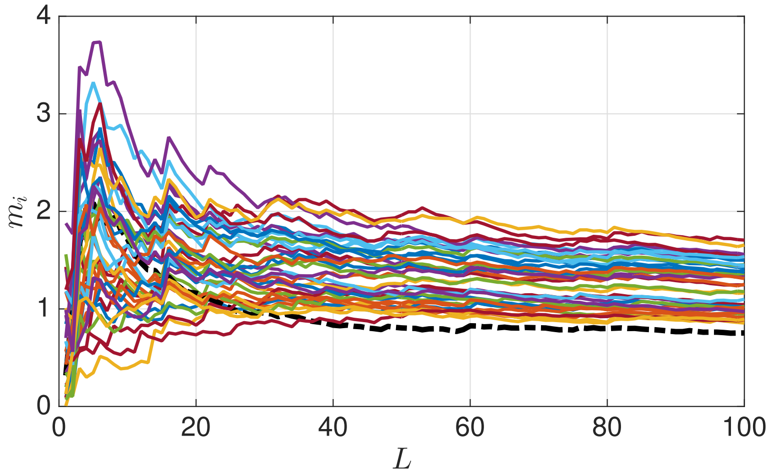

(a)

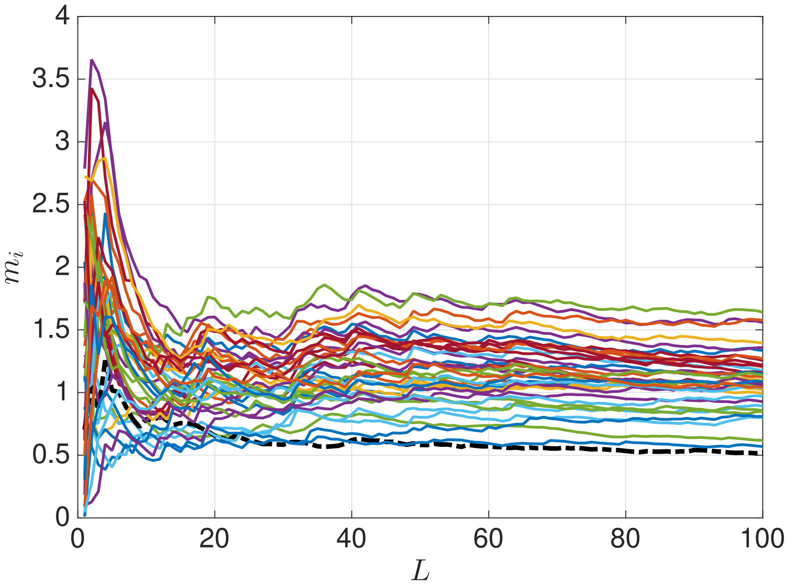

(b)

Figure 5.5: Values of $\{m_i\}$ as functions of L (each curve corresponds to an element m_i, $i = 1, ..., 4N$): $N = 10$

5.2.4 Geometric Interpretation

We now discuss the effectiveness of the proposed reinitialization strategy from a geometric viewpoint. Define a random variable as the Euclidean distance between the final weight vector and the current one. For the LMS algorithm, we define

$$D^{\mathrm{LMS}} = ||\mathbf{h}' - \mathbf{h}|| \tag{5.10}$$

where the current weight vector $\mathbf{h}$ and the new one $\mathbf{h}'$ are used. In the case of the WRL algorithm, a random variable is defined as the Euclidean distance between $\mathbf{h}'$ and the chosen reinitialization point $\mathbf{v}_{\hat{\imath}}$, according to (5.6) and (5.9), as it corresponds to the weight vector from which the WRL starts the adaptation after L steps, so that

$$D^{\mathrm{WRL}} = ||\mathbf{h}' - \mathbf{v}_{\hat{\imath}}||. \tag{5.11}$$

In order to evaluate the ultimate performance of the weight reset strategy, one can idealize the generation of the reinitialization vector, considering an infinite number of points over the hyper-sphere in $\mathbb{C}^n$. This would lead to the selection of the projection of $\mathbf{h}'$ on the hyper-sphere, i.e., the point $\mathbf{h}'||\mathbf{h}||/||\mathbf{h}'||$, so that a similar random variable, for the case of the ideal WRL (IWRL), is defined as follows:

$$D^{\mathrm{IWRL}} = \left\| \mathbf{h}' - \mathbf{h}' \frac{||\mathbf{h}||}{||\mathbf{h}'||} \right\|. \tag{5.12}$$

In Figure 5.6, a pictorial representation of the realizations of (5.10), (5.11), and (5.12) is shown for a simplified $\mathbb{R}^2$ scenario.

In order to quantify the potential benefits, in terms of distance reduction entailed by the proposed approach, one can numerically evaluate, via simulation, the Probability Density Function (PDF) of these random variables. An estimation of the PDF can be performed by the method of relative frequencies [16], evaluating (5.10), (5.11), and (5.12), considering a fixed initial channel impulse response $\mathbf{h} \in \mathbb{C}^N$ and a large number of randomly generated final channel impulse responses $\mathbf{h}' \in \mathbb{C}^N$. The elements of the initial vector $\mathbf{h}$

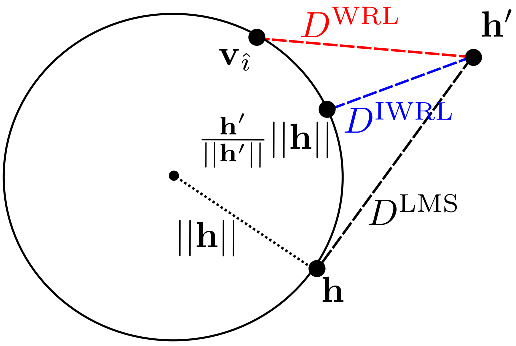

Figure 5.6: Pictorial representation of the distances D^{LMS}, D^{WRL}, and D^{IWRL} in $\mathbb{R}^2$.

and of the vectors $\mathbf{h}'$ are randomly generated according to a circular complex normal distribution with zero mean and unit variance.

The numerical analysis is carried out considering 10^5 vectors $\mathbf{h}'$ and $N = 4$, as the value of N does not affect the qualitative results. Hence, the WRL algorithm generates $4N = 16$ complex reinitialization points.

In Figure 5.7, the estimated PDFs of D^{LMS}, D^{WRL}, and D^{IWRL} (with $4N = 16$) are shown. It can be noticed that the distance is significantly reduced by the WRL algorithm, as shown by the distribution which is centered around lower values of d. Moreover, one can note that the generation of 16 reinitialization points is a good compromise between complexity of point generation and performance, as the distribution of D^{WRL} is much closer to that of D^{IWRL} than that of the original LMS algorithm.

5.2.5 Weight Reset VSLMS Algorithm

The adaptation speed of the LMS algorithm is related to the choice of the step size parameter μ. For this reason, previous works on the LMS convergence period reduction [54, 55] focused on the automatic tuning of μ, based on the use of the VSLMS algorithm.

The VSLMS algorithm is suitable for application scenarios in which a fast

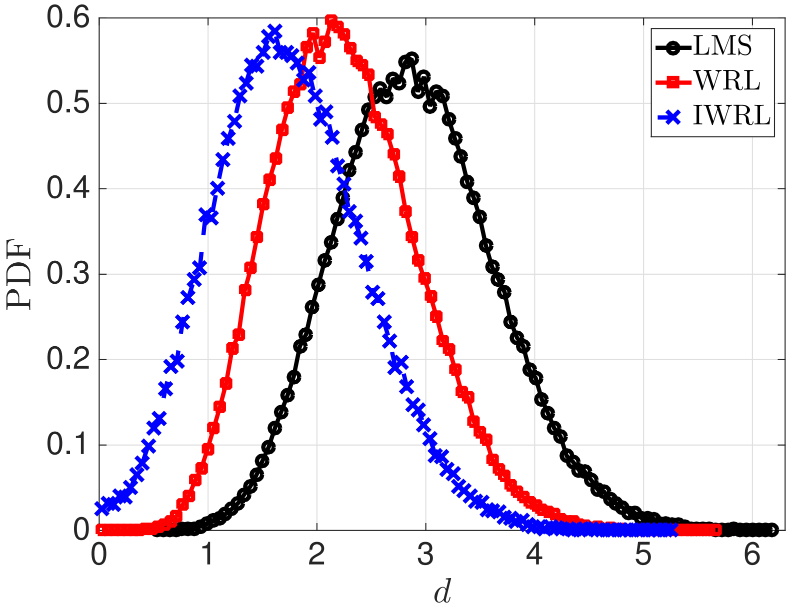

Figure 5.7: Estimated PDFs of the Euclidean distance D^{LMS}, D^{WRL}, and D^{IWRL} (with $4N = 16$).

algorithm convergence is required as it is based on the automatic adaptation of the step size parameter, with respect to the dynamics of the error signal, as it is discussed in Section 2.2.2. This means that it may significantly reduce the convergence period. Therefore, we are interested in investigating the possible improvement entailed by the weight reset strategy.

The application of the weight reset strategy to the VSLMS implementations described in Subsection 2.2.2 is straightforward. An important expedient, which allows to improve the performance of the Weight Reset VSLMS (WRVSL), is to fix the step size to its maximum allowed value $\mu^{\max}$ for the duration L of the parallel runs of the adaptation recursions, so that adaptation is as fast as possible after the detection of a channel variation and before the selection of the optimal reinitialization point.

5.3 Performance Analysis

First of all, we present a convergence analysis based on the MSE, without applying the weight reset strategy, for the different VSLMS implementations outlined in 2.2.2, in order to determine the most suitable version, in terms of stability and performance, for the considered scenario.

We assume that the inputs $\{x_k\}$ are i.i.d. symbols from a 4-QAM constellation with unit power. The variance of the noise samples $\{w_k\}$ is set to 0.01, so that the signal-to-noise ratio is equal to 20 dB. The channel is characterized by an impulse response in $\mathbb{C}^5$, i.e., $N = 5$ complex taps. We consider a channel variation, at instant $\tilde{k} = 2.5 \cdot 10^4$ (in terms of number of samples), between the following sample channel responses:

$$\mathbf{h} = \begin{pmatrix} 0.37 + \jmath 0.18 \\ 0.49 - \jmath 0.06 \\ 0.24 + \jmath 0.55 \\ 0.06 + \jmath 0.3 \\ 0.12 + \jmath 0.3 \end{pmatrix} \quad \mathbf{h}' = \begin{pmatrix} -0.14 + \jmath 0.3 \\ 0.12 + \jmath 0.55 \\ -0.59 + \jmath 0.15 \\ -0.32 + \jmath 0.1 \\ -0.21 - \jmath 0.009 \end{pmatrix} .$$

The value of ρ in (2.11), set by trial and error, is equal to $5 \cdot 10^{-2}$ and the value of $\mu^{\min}$ is set to 10^{-4}. Figure 5.8 shows the MSE $\mathcal{E}(\mathbf{c})$ in dB, as a function of time for different values of $\mu^{\max}$ and for the following weight update recursions: Classical (2.10), Signed-Regressor (2.12), and Sign-Sign (2.13). One can see that, for both $\mu^{\max} = 10^{-1}$ and $\mu^{\max} = 10^{-2}$, the performance the Sign-Sign version of the VSLMS algorithm is the less stable of the three considered implementations. In Figure 5.8 a, one can note that the performance of the Classical and Signed-Regressor implementations is comparable, while in Figure 5.8b, one can see that the Signed-Regressor version is faster, suggesting that, for this scenario, it may be the preferable implementation, as it allows a fast convergence during the transient period and firmly maintains a stable steady-state value, after the convergence. Moreover, as it is expected, when $\mu^{\max} = 10^{-1}$, the performance is improved, as during the convergence period the step size can assume large values, speeding up the convergence process.

Figure 5.9, shows the trend of μ_k, as a function of time, for various weight update recursions and for $\mu^{\max} = 10^{-1}, 10^{-2}$. The trend of μ_k confirms the previous analysis based on the MSE. In Figure 5.9a, it can be noted that, after the abrupt channel variation, the upper limit of the step size $\mu^{\max} = 10^{-1}$ is never reached by μ_k, while this happens when $\mu^{\max} = 10^{-2}$, as visible in Figure 5.9b. Note that these results depend on the choice of ρ, which specifies the sensitivity of the algorithm to variations of the dynamics of e_k.

According to the obtained results, we compare the WRL algorithm with the WRVSL algorithm, for the Signed-Regressor version, as it appears to be the most stable of the analyzed cases.

Since $N = 5$, the complex reinitialization points generated by the algorithm are $4N = 20$. The weight reset is triggered when E_k in (5.3) reduces or increases by 5% with respect to its steady-state value (i.e., $\eta = 0.05$). The sensitivity parameter k_{th}, discussed in Subsection 5.2.1, is set by trial and error to 100 samples. The choice of parameter L depends on the number of the weight vector elements N, as discussed in Subsection 5.2.3, so that we set $L = 30$. The LMS update step size μ is set to 0.001. The VSLMS step size bounds are

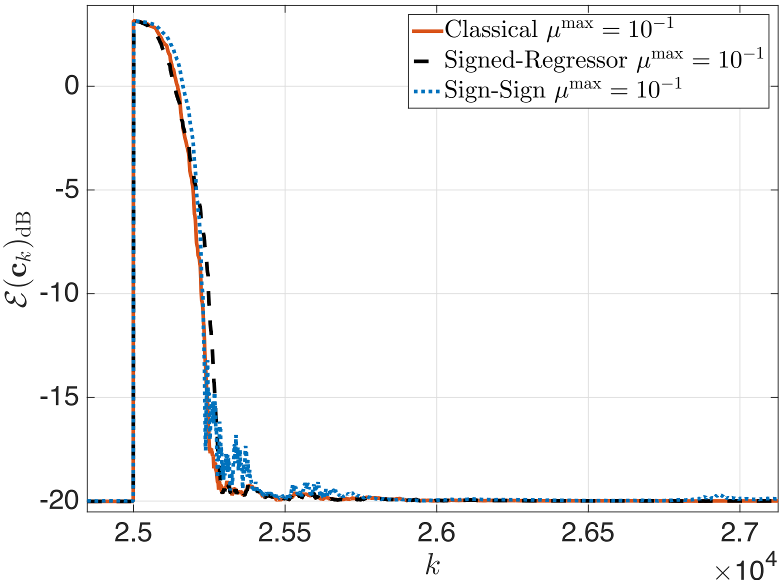

(a)

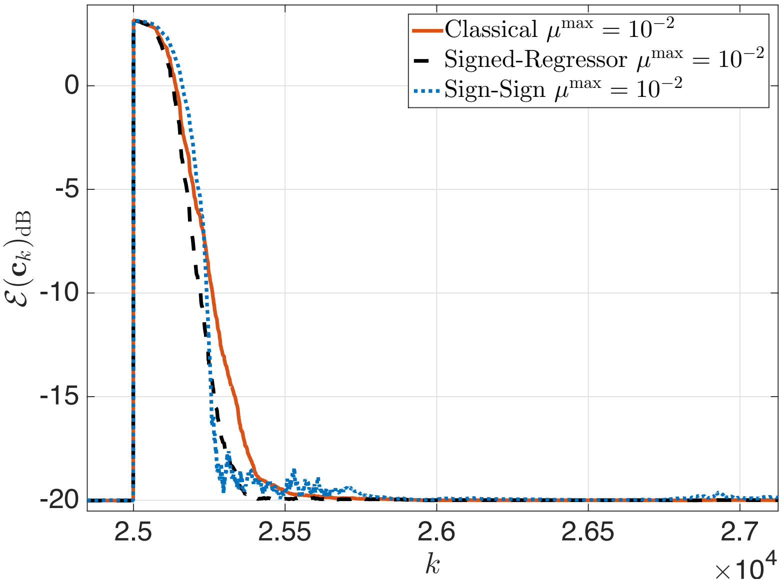

(b)

Figure 5.8: $\mathcal{E}(\mathbf{c})$ in dB, as a function of the time for different weight update recursion: (a) $\mu^{\max} = 10^{-1}$ and (b) $\mu^{\max} = 10^{-2}$.

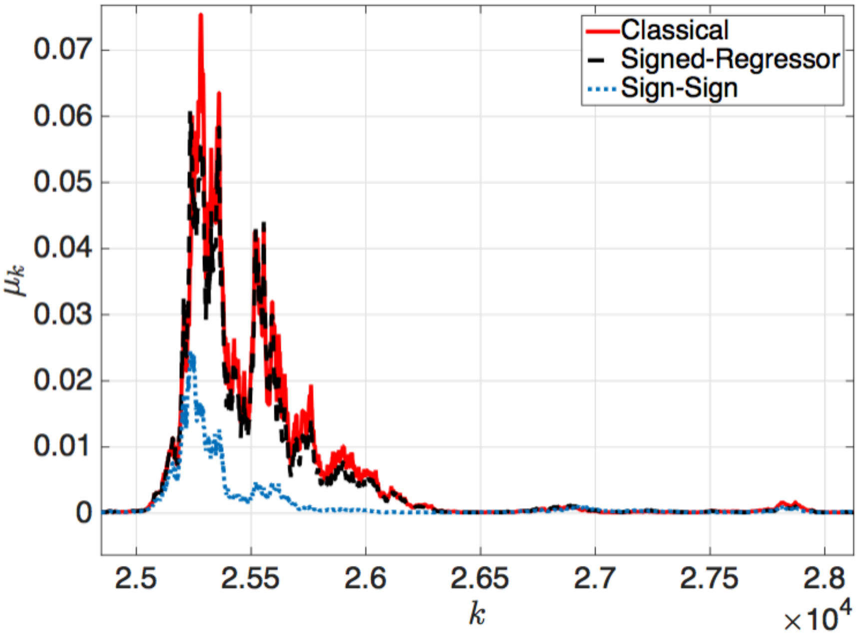

(a)

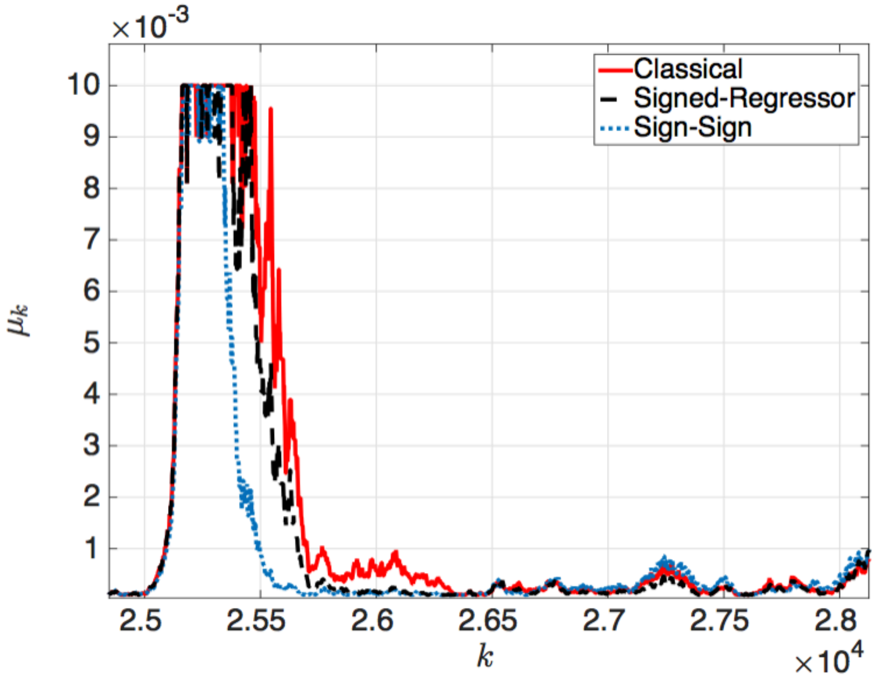

(b)

Figure 5.9: μ_k, as a function of time, for different weight update recursion: (a) $\mu^{\max} = 10^{-1}$ and (b) $\mu^{\max} = 10^{-2}$.

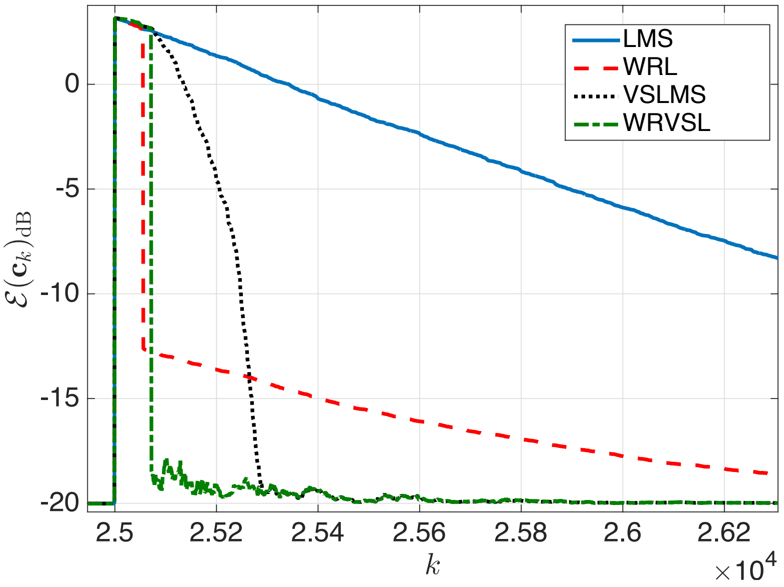

Figure 5.10: $\mathcal{E}(\mathbf{c}_k)$, as a function of time, for a channel variation at instant $\tilde{k} = 2.5 \cdot 10^4$ and the algorithms LMS, WRL, VSLMS, ans WRVSL.

set to $\mu^{\max} = 10^{-1}$ and $\mu^{\min} = 10^{-4}$ and the parameter ρ is set to $5 \cdot 10^{-2}$.

We consider the channel identification system and the previously defined channel responses $\mathbf{h}$ and $\mathbf{h}'$, and set $\mu^{\max} = 10^{-1}$. According to the results of Section 5.2.3, we set $L = 30$. Figure 5.10 shows the MSE as a function of time for the LMS and VSLMS algorithms and their Weight Reset versions. The step size of the LMS and WRL algorithms is set to $\mu = 10^{-3}$. One can note that the WRL algorithm allows a significant reduction of the convergence transient period. Defining the time needed by the MSE in dB to converge to 98% of its new steady-state value, the convergence period reduction, with respect to the LMS algorithm, is about 46%. The VSLMS significantly outperforms LMS. However, the weight reset strategy improves the performance of the WRVSL algorithm as well, in particular, the convergence period reduction is about 48%. These results demonstrate that the application of the weight reset strategy to both LMS and VSLMS algorithms may significantly reduce the

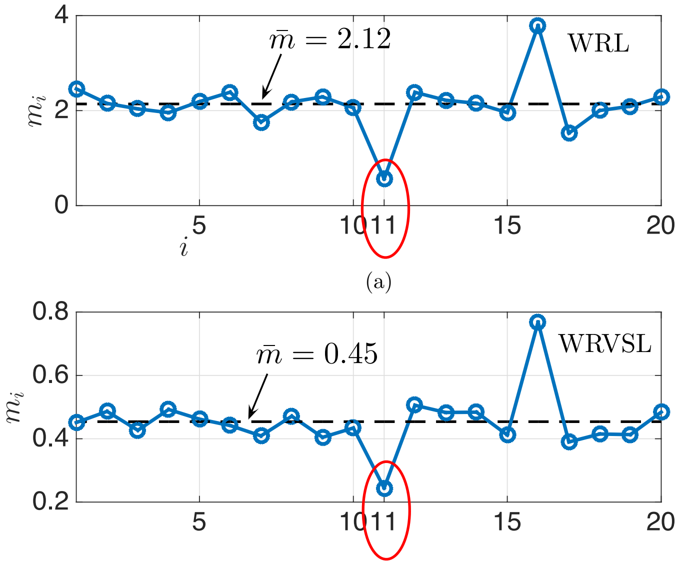

(a)

(b)

Figure 5.11: Elements of $\mathbf{m}$ at epoch $\tilde{k}+L$ (selection of reinitialization point): (a) WRL and (b) WRVSL. The average value $\bar{\mathbf{m}}$ is highlighted in both case.

relative transient period caused by a channel variation. It is interesting to note that the weight reset is triggered at different time epochs for the WRL and WRVSL algorithms. This is expected, as the channel variation, based on the detection of an energy variation, is detected at different instants, as the adaptation speed, controlled by different step sizes, is different for the WRL and WRVSL algorithms.

Figure 5.11 shows the elements of the vector $\mathbf{m}$, given in (5.7), for both the WRL and WRVSL algorithms, after $L = 30$ steps, i.e., at the moment of the reinitialization point selection. One can see that for both algorithms $\hat{\imath}$, is equal to 11, i.e., the smallest element of $\mathbf{m}$ is obtained for the 11-th column of the matrix $\mathbf{V}$. This is expected, as the reinitialization point closest to the final one is the same in both cases. It is also interesting to note that, although the two curves in Figure 5.11a and Figure 5.11b are similar, the arithmetic average of the elements $\{m_i\}$, i.e., $\bar{m} = \sum_{i=1}^{4N} m_i/(4N)$, after L steps is smaller for the WRVSL. In particular, $\bar{m} = 2.12$ for WRL and $\bar{m} = 0.45$ for WRVSL. This is expected, as after L steps the WRVSL algorithm, set with its maximum step size, can bring the weight vector associated with every reinitialization point closer to the final point, while WRL, set with a fixed (smaller) step size shows a slower convergence.

5.3.1 Hybrid Weight Reset LMS

Although the VSLMS proved to be effective in coping with abrupt channel variations, as mentioned, the setting of its parameter ρ, $\mu^{\min}$, and $\mu^{\max}$ may not be straightforward. The application of the more powerful WRVSL requires the additional setting of the parameter L and the sensitivity parameter k_{th}.

In order to reduce the complexity of a suitable setting of the WRVSL algorithm, we propose a hybrid implementation of the WRL algorithm, based on the idea that the convergence transient period can be reduced with both the application of the weight reset and the temporary increment of the step size value, during the run of the parallel LMS instances. This hybrid WRL weight recursion can be formulated as follows:

$$\mathbf{c}_{k+1} = \begin{cases} \mathbf{c}_k + \lambda\mu\mathbf{x}_k^* e_k & \text{if } \tilde{k} + \Delta k < k < \tilde{k} + \Delta k + L \\ \mathbf{c}_k + \mu\mathbf{x}_k^* e_k & \text{else} \end{cases}$$

where $\tilde{k} + \Delta k$ is the epoch at which the channel variation is detected, being Δk the interval needed for the detection, and $\lambda \geq 1$ is the ratio between the temporary step size $\lambda\mu$ and the step size μ. In other words, the WRL algorithm acts as the WRVSL algorithm only during the convergence period allowing only two values of the step size, namely μ and $\lambda\mu$. We observed that $\lambda = 10^2$ is sufficient to improve the algorithm performance.

In Figure 5.12, the performance of the Hybrid WRL algorithm is shown for $\lambda = 10^2$ and compared with that of the previously described algorithms. One can note that the Hybrid WRL performance is comparable with that of

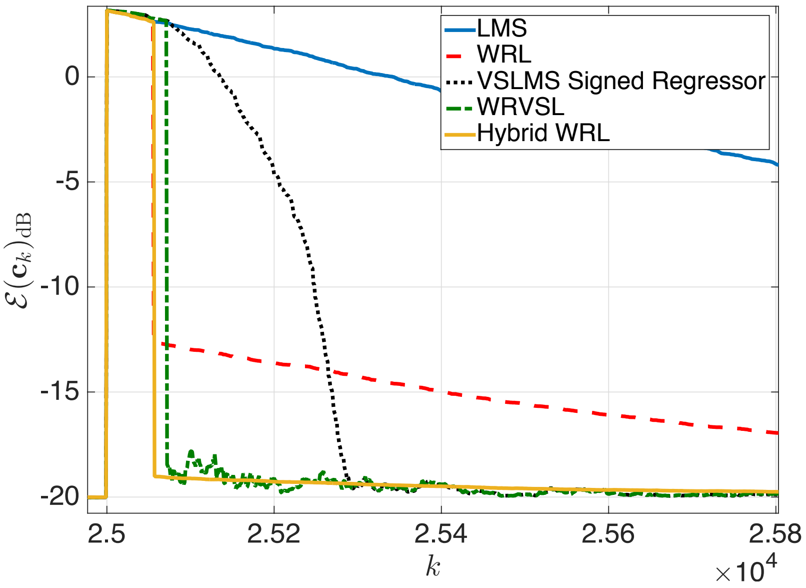

Figure 5.12: $\mathcal{E}(\mathbf{c}_k)$, as a function of time, for a channel variation at instant $\tilde{k} = 2.5 \cdot 10^4$ and various adaptation algorithm.

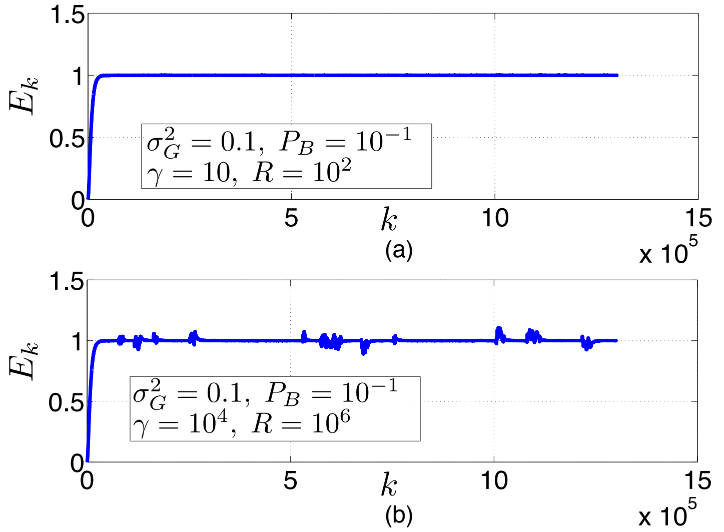

Figure 5.13: E_k as a function of k for different impulse noise processes: (a) realistic impulse noise and (b) unrealistic (very strong) impulse noise.

the WRVSL algorithm.

5.4 Weight Reset for Echo Cancellation in a PLC Modem

We now consider the application of the proposed weight reset strategy to the case of the echo cancellation in a PLC modem.

First of all, we take into account the presence of the impulse noise, discussed in Section 1.3, without considering an abrupt channel variation. Figure 5.13 a shows E_k, given by (5.3), as a function of the sample index k, for $\sigma_G^2 = 0.1$, $P_B = 10^{-1}$, $\gamma = 10$, and $R = 100$, in the case of a generic echo response with unit energy. It can be observed that, after the initial transient period needed for convergence (whose duration depends on μ), E_k approaches 1. The selected value of P_B represents a worst case, while the values of γ and R are more realistic [10]. One can note that the impulse noise does not affect the stability of the weight vector energy at its steady-state value, even in the presence of realistic impulsive events. This means that, as expected, the weight update process is not compromised. Not only, but it is important to notice that the impulse noise would not hinder the detection of an echo channel variation, as it does not entail a significant variation of E_k.

Despite the optimal solution is not influenced by the noise, whether AWGN or impulse noise, its stability can be compromised by a very strong impulsive event. In order to observe this phenomenon, we simulated a very long and strong impulse with $P_B = 10^{-1}$, $R = 10^6$, and $\gamma = 10^4$, for $\sigma_G^2 = 0.1$. This case is considered in Figure 5.13b, where E_k is shown as a function of k. One can note that these “huge” impulsive events affect the weight update. However, once an impulsive event ends, the algorithm converges back to its optimal solution at a speed equal to that of the initial transient period. We also remark that only the large value of R affects the weight vector update, while the burst length, which depends on γ, does not. Given these results, we can hereinafter neglect the impulse noise and assume, without loss of generality, that the physical channel from the remote terminal is ideal.

We now consider a channel variation between the echo channel responses, of duration $N = 22$, $\mathbf{h}$ and $\mathbf{h}'$, shown in Figure 5.14, representing the baseband equivalents of echo responses obtained by field measurements, performed by Selta on a 110 km high-voltage power line at 380 kV. The weight reset is triggered when E_k is subject to a variation of 5% with respect to its steady-state value and the WRL sensitivity parameter is $k_{\text{th}} = 50$. We found $L = 100$ to be suitable for $N = 22$, in this scenario. In Figure 5.15, the MSE (5.1) is shown as a function of time (sample epoch), for both LMS and WRL algorithms. As one can see, also in a realistic scenario the WRL algorithm proves effective, as it allows a reduction of the convergence period about 52% with respect to the standard LMS algorithm.

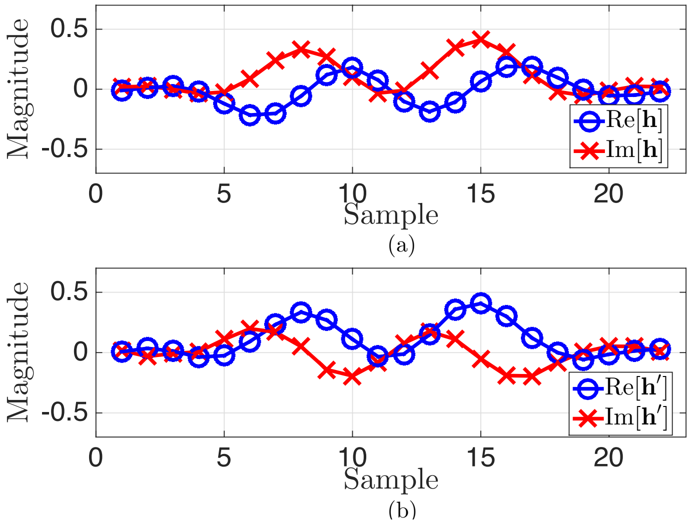

Figure 5.14: Baseband equivalent of field measurements on a high-voltage power line of echo impulse responses: (a) $\mathbf{h}$ and (b) $\mathbf{h}'$.

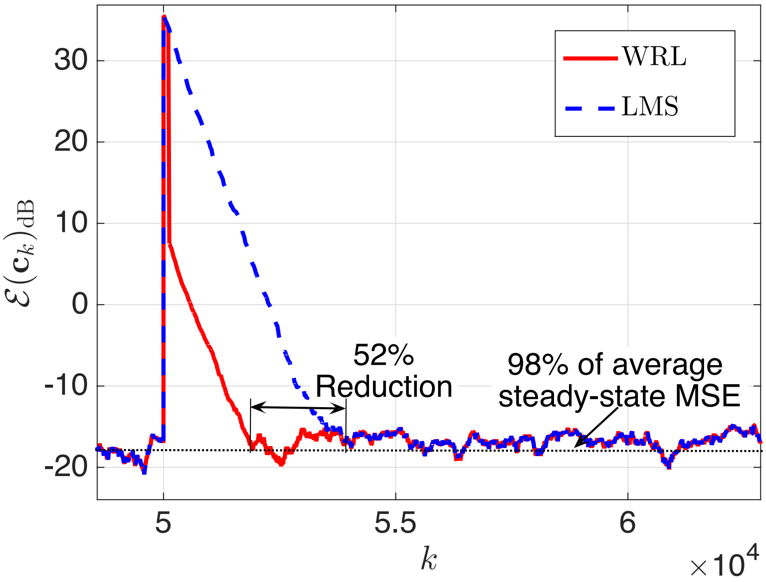

Figure 5.15: $\mathcal{E}(\mathbf{c}_k)$ as a function of time in the case of an echo channel variation at instant $\tilde{k} = 5 \cdot 10^4$.

5.5 Conclusions

In this chapter we proposed a weight reset method to shorten the transient convergence period of the LMS algorithm in the presence of abrupt channel variations. We applied this method to both the LMS and VSLMS algorithms, for the problem of channel identification, demonstrating its effectiveness and performance advantages in terms of convergence time reduction. In particular, the application of the proposed strategy to the VSLMS algorithm further improves the convergence speed, already sped up by the adaptation of the step size by the VSLMS algorithm itself.

Since the setting of the WRVSL algorithm is not straightforward for every scenario, we also proposed a simple hybrid WRL algorithm, based on the temporary increment of the step size, after the channel variation detection and before the convergence. The results prove that this hybrid WRL is also suitable for coping with abrupt channel variations.

We also presented the results of the application of weight reset in an echo cancellation scenario of a PLC modem, taking into account field measures and the presence of impulse noise. In this realistic scenario, the proposed weight reset LMS confirmed its effectiveness in significantly reducing the convergence time.

Part II

Coding Schemes in PLC Systems

Chapter 6

LDPC coded Modulations

6.1 Introduction

In Power Line Communications (PLC) systems the design of low latency and high spectral efficiency coding scheme is requested. Low-density parity-check (LDPC) codes [56, 57] have been considered as channel coding solution for PLC systems [58, 59], especially for their capability to limit the influence of the power line noise [12, 60]. In particular, LDPC coding-based solutions, oriented to the improvement of the energy efficiency of the digital transmission systems, are of interest. Moreover, a suitable LDPC coded scheme has to cope with overall encoding and decoding latency constraints of PLC systems. To this end, LDPC codes with short codeword lengths are appealing and, among them, coding schemes based on the use of the LDPC codes adopted in IEEE 802.16e standard (WiMAX) [61, 62], whose maximum supported codeword length is $n = 2304$ bits.

The structure of WiMAX LDPC codes can be described by the use of the so-called exponent matrix to specify the code parity check matrix, so that these LDPC codes not only allow a low-latency encoding/decoding process, but entail also a limited memory consumption for the storage of the parity check matrix in the digital signal processor. The LDPC codes of the WiMAX

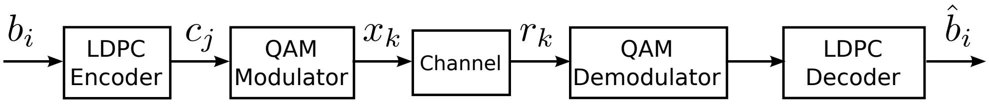

Figure 6.1: General System Model.

standard support four rates (1/2, 2/3, 3/4, and 5/6), and 19 codeword sizes, from $n = 576$ bits up to $n = 2304$ bits. This suggests that the coding schemes here presented may be suitable also for enabling adaptive modulation and coding techniques, based on the selection of different rates and codeword lengths for dealing with different channel conditions.

In this chapter, we describe the WiMAX LDPC codes structure and present different modulation and coding schemes, focusing on high-rate and small codeword size codes, expedient to maximize the spectral efficiency and minimize the introduced latency.

The chapter is organized as follows. In Section 6.2, we review the structure of the WiMAX LDPC codes. In Section 6.3, the discussion of the coded modulation schemes based on the use of the LDPC codes is provided. In Section 6.4, a performance analysis of the proposed schemes is presented. Moreover, we discuss their spectral efficiency and computational latency cost and analyze their effectiveness in a PLC scenario, considering also the presence of impulse noise, modeled as described in Section 1.3. Finally, concluding remarks are given in Section 6.5.

6.2 WiMAX LDPC Codes

The reference system model is depicted in Figure 6.1. The information bit sequence $\{b_i\}$ is encoded by means of an LDPC code into the sequence $\{c_j\}$, which is then mapped to the sequence $\{x_k\}$ of M-ary QAM symbols. In particular, the symbol x_k is generated starting from the following coded bit block:

$$\{c_j\}_{j=(k-1)\log_2 M+1}^{k\log_2(M)}.$$

Iterative decoding on the received sequence $\{r_k\}$ is performed at the receiver [63]. We hereinafter assume that the iterative process stops if all parity checks are satisfied or if the iteration number has reached 50.

The LDPC encoder maps blocks of information bits of length k into blocks of length n, so that the code rate is

$$R_c = k/n.$$

The parity check matrix $\mathbf{H}$ of the LDPC code has size $m \times n$, where m is the number of parity check bits in the code, so that the number of systematic bits is $k = n - m$. The structure of a WiMAX LDPC code is defined in terms of the exponent matrix $\mathbf{E}$ of size $m_b \times n_b$, where n_b is set to 24 and m_b depends on the code rate. The matrix $\mathbf{H}$ is obtained as the expansion from the exponent matrix $\mathbf{E}$, whose elements are $e_{ij} \in \{-1, 0, 1, ..., k_{\max}\}$, with $k_{\max}$ being a proper integer, as follows:

$$\mathbf{H}_{(n-k)\times n} = \begin{bmatrix} \mathbf{\Pi}^{e_{11}} & \cdots & \mathbf{\Pi}^{e_{1n_b}} \\ \vdots & \ddots & \vdots \\ \mathbf{\Pi}^{e_{m_b 1}} & \cdots & \mathbf{\Pi}^{e_{m_b n_b}} \end{bmatrix}$$

where $\mathbf{\Pi}$ is the permutation matrix, of size $z \times z$, z being the so-called expansion factor set to $n/24$, defined by a circular left-shift by one position on the $z \times z$ identity matrix, i.e.,

$$\mathbf{\Pi} = \begin{bmatrix} 0 & 0 & \cdots & 0 & 1 \\ 1 & 0 & \cdots & 0 & 0 \\ 0 & 1 & \cdots & 0 & 0 \\ \vdots & \vdots & \ddots & \vdots & \vdots \\ 0 & 0 & \cdots & 1 & 0 \end{bmatrix}.$$

In particular, $\mathbf{\Pi}^0 = \mathbf{I}$ and, by convention, $\mathbf{\Pi}^{-1}$ is the null matrix.

Because of this particular structure, one can see that the size of the matrix $\mathbf{H}$ is specified by $m = z \cdot m_b$ and $n = z \cdot n_b$. This matrix consists of $m_b \cdot n_b$

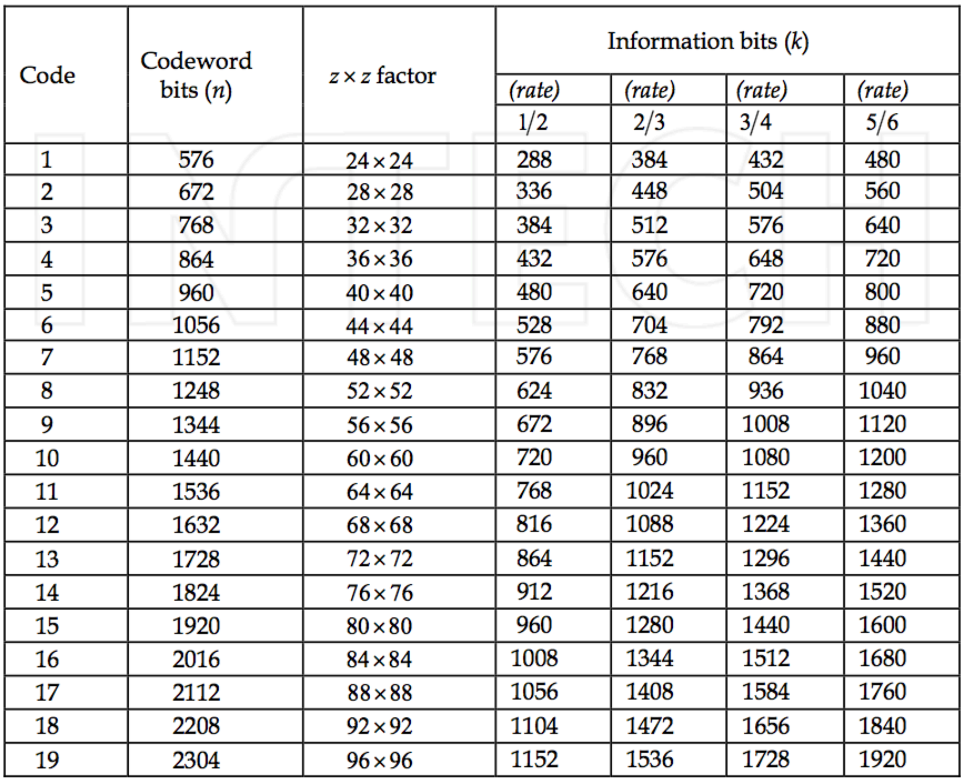

Code	Codeword bits (n)	$z \times z$ factor	Information bits (k)			
			(rate) 1/2	*(rate)* 2/3	*(rate)* 3/4	*(rate)* 5/6
1	576	24×24	288	384	432	480
2	672	28×28	336	448	504	560
3	768	32×32	384	512	576	640
4	864	36×36	432	576	648	720
5	960	40×40	480	640	720	800
6	1056	44×44	528	704	792	880
7	1152	48×48	576	768	864	960
8	1248	52×52	624	832	936	1040
9	1344	56×56	672	896	1008	1120
10	1440	60×60	720	960	1080	1200
11	1536	64×64	768	1024	1152	1280
12	1632	68×68	816	1088	1224	1360
13	1728	72×72	864	1152	1296	1440
14	1824	76×76	912	1216	1368	1520
15	1920	80×80	960	1280	1440	1600
16	2016	84×84	1008	1344	1512	1680
17	2112	88×88	1056	1408	1584	1760
18	2208	92×92	1104	1472	1656	1840
19	2304	96×96	1152	1536	1728	1920

Table 6.1: Properties of WiMAX LDPC codes, reproduced from [64].

blocks of size $z \times z$, which can be null matrices or circularly shifted versions of $\mathbf{\Pi}$, with shift order stored in the corresponding element of $\mathbf{E}$. This means that the parity check matrices of WiMAX LDPC codes can be completely defined by the code length n, the systematic bit sequence length k, and the exponent matrix $\mathbf{E}$. The exponent matrices related to the four supported WiMAX code rates are listed[1] in [61]. The properties of the WiMAX LDPC codes are collected in Table 6.1.

Figure 6.2 shows the parity check matrix $\mathbf{H}$ for $n = 576$, which is the smallest allowed codeword length, considering two values of R_c: (a) 1/2 and

---

[1] In [61], two alternative exponent matrices for code rates 2/3 and 3/4 are also listed, which may be preferred for certain hardware implementations.

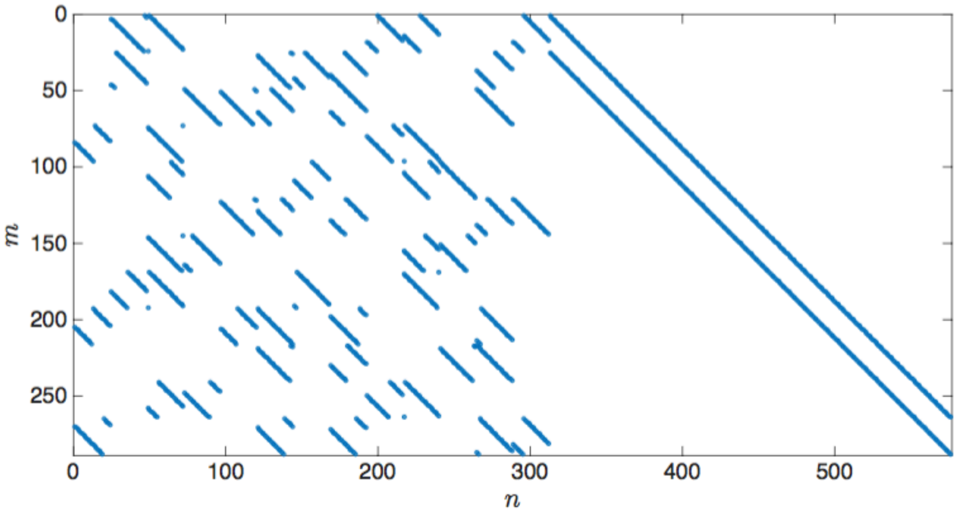

(a) $R_c = 1/2$

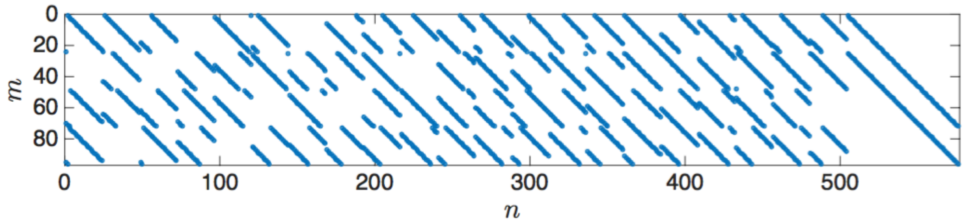

(b) $R_c = 5/6$

Figure 6.2: Parity check matrices for the code labeled as "1" in Table 6.1: $n = 576$ and code rates 1/2 (a) and 5/6 (b).

(b) 5/6. Each figure represents a matrix, in which dots identify the presence of a 1.

6.3 LDPC Coded Modulations

We now discuss a coding scheme based on MultiLevel Coding (MLC) [65], which allows to improve the system performance, approaching the channel capacity. According to this scheme, a portion of the information bits is coded by the LDPC code, while the other part is uncoded. An M-QAM symbol is composed by $b_c + b_f = \log_2 M$ bits, where we denote by b_c the number of coded bits $\{c_k\}$ and by b_f the number of uncoded ("free") bits $\{f_k\}$. Note that

$$b_f = \log_2 M - b_c.$$

The spectral efficiency of a system which employs an M-ary modulation is defined as $\eta = R_c \log_2 M$ (in the uncoded case, one has $R_c = 1$). For the proposed multilevel scheme, the spectral efficiency is defined as

$$\eta = R_c b_c + b_f \tag{6.1}$$

since only b_c bits are coded.

The used multilevel coding scheme enables multistage decoding based on the idea that, once the b_c bits have been decoded, they specify a subset of the M-ary constellation with M_f points, where $M_f = \log_2 b_f$. In other words, we employ a set partitioning [65, 66] on the M-ary constellation. As explained in [65], the bit mapping onto the constellation must be set properly, in order to maximize the minimum intra-subset Euclidean distance.

As a representative results for the proposed multilevel coding schemes, we consider $M = 64$. In this case, one has

$$b_f = 6 - b_c. \tag{6.2}$$

The results can be easily extended to other constellation sizes. In the following, we refer to a generic mapping scheme for multilevel coding as MLC(b_c, b_f), highlighting the difference between the proposed schemes in terms of coded and free bit.

6.3.1 A Multilevel Coding Scheme

We herein discuss the case with $b_c = 3$ and $b_f = 3$, so that the coded bits identify 8 subsets composed of $M_f = 8$ points. In this case, we consider the symbol sequence to be obtained from a sequence of one free bit every one coded bit. We have observed, however, that the positions of the free bits do not influence the scheme performance.

We choose the 8-QAM subset mapping so that the Euclidean distance of the symbols is maximized. Figure 6.3 shows the rectangular 8-QAM mapping and our custom mapping, chosen among several possibilities. We consider the constellation normalized so that the average symbol power is 1. While the rectangular mapping is Gray, the custom one is not, but its Euclidean distance is larger. The improved performance of the custom mapping is shown in Figure 6.4, where the Bit Error Rate (BER) over an Additive White Gaussian Noise (AWGN) channel is drawn for the uncoded system.

The 64-QAM constellation mapping for the MLC$(3, 3)$ is shown in Figure 6.5, where it is emphasized the subset labeled as "100", identified by the second, fourth, and sixth bits, which are the coded ones. The subset identifies one of the 8-point subsets.

The encoding and decoding schemes are shown in Figure 6.6, where the length of the bit frame, which depends on the codeword length n, is highlighted in the case of the WiMAX LDPC code with $R_c = 5/6$ which supports $n = 2304$ and, therefore, $k = R_c n = 1920$. According to the labeling of the WiMAX LDPC codes in [64], reported in Table 6.1, where the 19 WiMAX LDPC codes are numbered in increasing order (from the one which supports the shortest codeword), the code chosen here is the number 19, so that we herein refer to it as the LDPC code 19. According to the sizes of n and k, the bit frame $\{b_i\}$

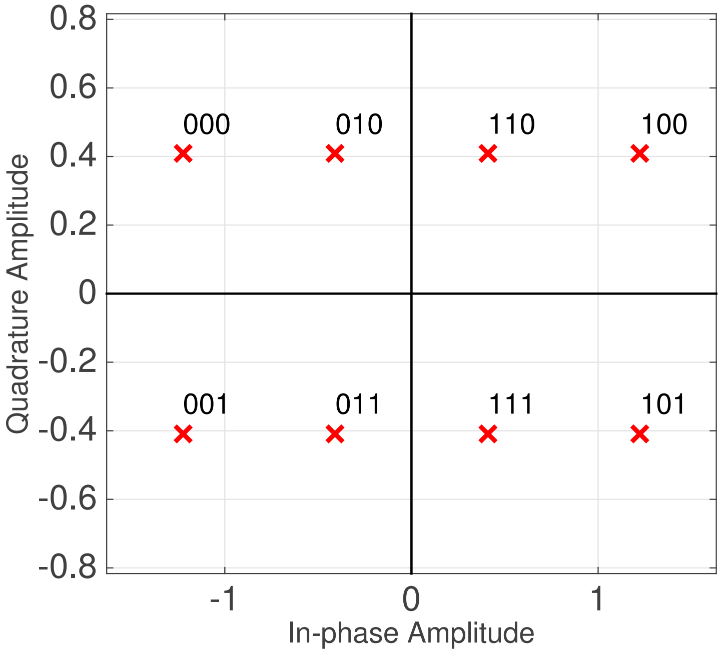

(a)

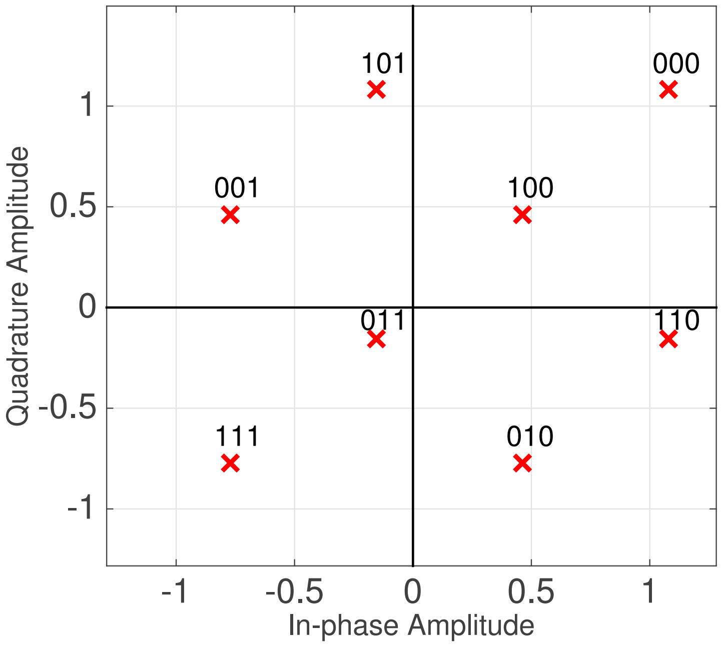

(b)

Figure 6.3: 8-QAM constellation mapping: Rectangular (a), Custom (b).

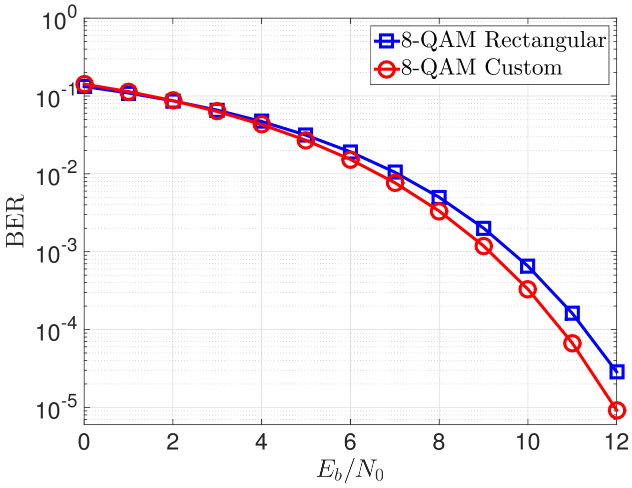

Figure 6.4: BER for the rectangular and custom mapping of 8-QAM over an AWGN channel for the uncoded system.

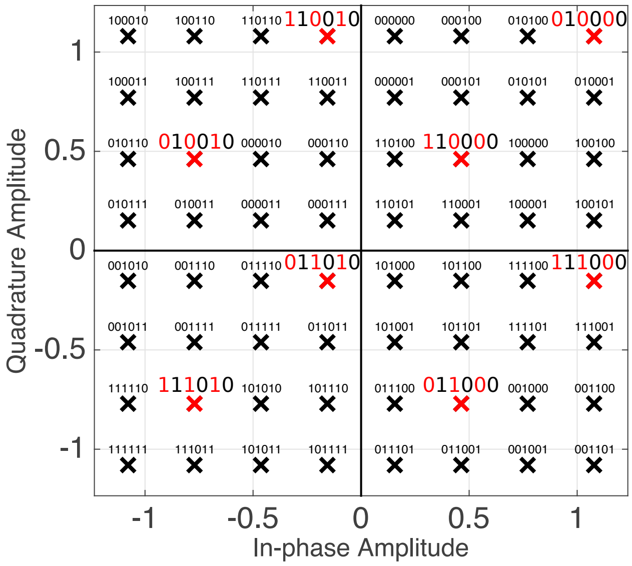

Figure 6.5: 64-QAM mapping for MLC(3, 3).

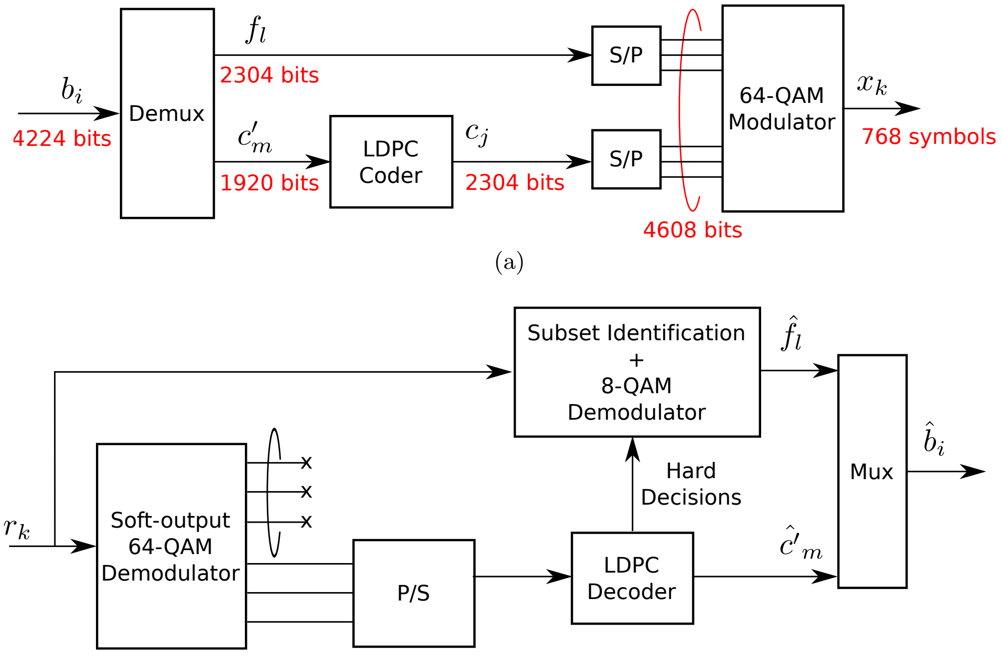

(a)

(b)

Figure 6.6: MLC$(3, 3)$ transmitter and receiver, with WiMAX LDPC code 19: $n = 2304$ and $R_c = 5/6$.

to be sent to the transmitter must have length equal to 4224, which is split into 2304 free bits $\{f_l\}$ and $k = 1920$ bits $\{c'_m\}$ to be coded into $n = 2304$ bits $\{c_j\}$. The total amount of 4608 bits is mapped onto 768 symbols by the 64-QAM modulator.

The latency delay due to the encoding/decoding process is related to the symbol frame generated according to n. In particular, the overall latency is defined as the time needed to generate the frame of symbols at the transmitter plus the time needed to collect the same frame at the receiver. For example, in the case shown in Figure 6.6, the overall latency is $768 + 768 = 1536$ symbols.

After demodulation, the bits associated with the positions of the free bits are discarded, while b_c bits are decoded, providing the decisions $\{\hat{c'}_i\}$ on the coded information bits. The soft decisions [67] provided by the demodulator are passed to the decoder. The hard decision on the decoded bits are then passed to the subset identification block, so that the 8-QAM symbols within the selected subset are demodulated, providing the decisions on the free bits $\{\hat{f}_l\}$. The sequences $\{\hat{f}_l\}$ and $\{\hat{c}_m\}$ are multiplexed, delivering the bit information sequence $\{\hat{b}_i\}$.

6.3.2 BER Balance Analysis

We now present a performance analysis for the described coding scheme and for a similarly designed one, denoted as MLC$(4, 2)$, in which $b_c = 4$ and $b_f = 2$. We use codes with high rate (to achieve the highest spectral efficiency) and short length (to minimize latency) and we show the BER results, in terms of free and code bits, as a function of the energy-per-bit to noise ratio E_b/N_0.

Denoting by BER_f and BER_c the BER measured for the free and code bits, respectively, the overall BER of the system is then given by the weighted mean of the two BERs, based on the numbers of free and code bits b_f and b_c per symbol, so that

$$\mathrm{BER}_{tot} = \frac{1}{b}\left(b_f \mathrm{BER}_f + b_c \mathrm{BER}_c\right). \tag{6.3}$$

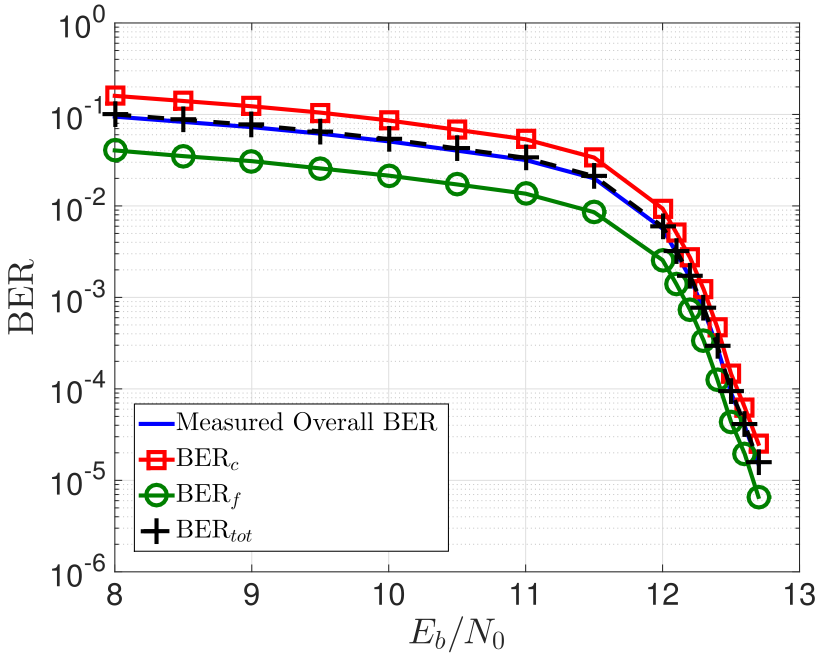

Figure 6.7: Multilevel coding BER analysis for MLC$(3, 3)$. WiMAX code 19, $n = 2304$ and $R_c = 5/6$.

In Figure 6.7, the results for MLC$(3, 3)$, for the code 19 ($n = 2304$) with $R_c = 5/6$, are shown. In this case, BER_c and BER_f are equally weighted by $1/2$. Figure 6.8 shows the results for MLC$(4, 2)$ for the code 19 ($n = 2304$) with $R_c = 5/6$. Clearly, BER_f, which represents here the lower bound for the BER, is worse in the case of MLC$(3, 3)$ than that of the case of MLC$(4, 2)$, because of the reduced distance among points in the subset constellations. The overall BER is degraded by BER_c, which heavily impacts on BER_{tot} as it is weighted in (6.3) by $b_c/b = 2/3$. Moreover, the measured BER is in agreement with BER_{tot}.

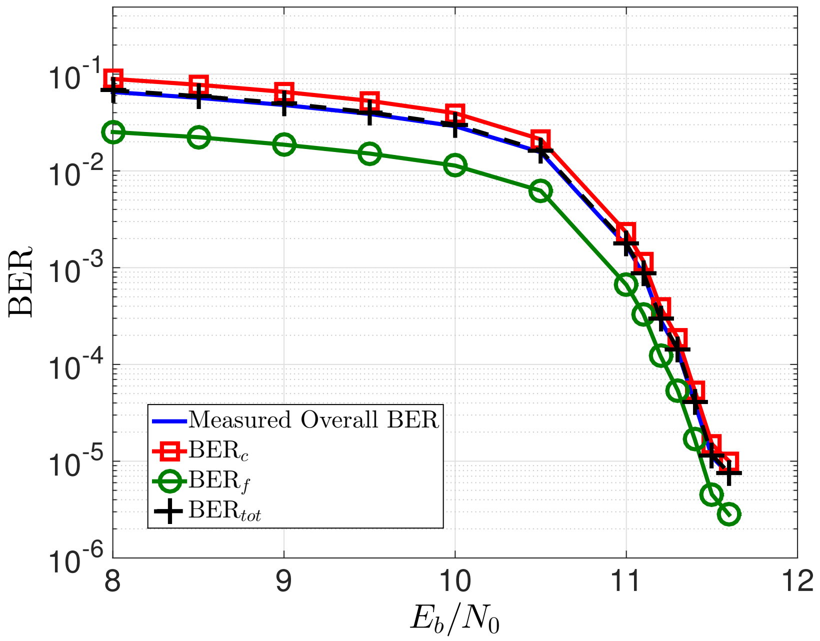

Figure 6.8: Multilevel coding BER analysis for MLC$(4,2)$. WiMAX code 19, $n = 2304$ and $R_c = 5/6$.

6.4 Performance Analysis

We now present the results obtained for the proposed coding schemes. We first consider the physical channel to be an AWGN channel and, then, we investigate the ability of the proposed LDPC coded modulation to cope with impulse noise.

We consider a high code rate R_c, in order to obtain the larger spectral efficiency η in (6.1). In particular, we wish η to be close as close as possible to the obtainable spectral efficiency in the case of uncoded system, i.e., $\eta = \log_2 M$, which, in this case is $\eta = \log_2 64 = 6$ per channel use.

We choose the higher supported code rate for WiMAX standard LDPC codes, i.e., $R_c = 5/6$, so that, according to (6.1), the spectral efficiencies of the coded systems presented in Section 6.3 are:

$$\eta = \begin{cases} \frac{5}{6}6 = 5 & \text{for MLC}(6,0) \\ \frac{5}{6}4 + 2 \simeq 5.3 & \text{for MLC}(4,2) \\ \frac{5}{6}3 + 3 = 5.5 & \text{for MLC}(3,3). \end{cases} \tag{6.4}$$

Note that MLC$(6,0)$ refers to the coding scheme, described in Section 6.2, in which multilevel coding is not implemented, i.e., all the bits are coded.

6.4.1 AWGN Channel

The received signal, according to the general model shown in Figure 6.1, is $r_k = x_k + w_k$, where w_k are the independent and identically distributed (i.i.d.) samples of AWGN, with variance σ_w^2. The BER, as a function of E_b/N_0, measured for the various considered coding schemes and different LDPC codes, is shown in Figure 6.9. The best performance is achieved by the MLC$(6,0)$ coding scheme with WiMAX LDPC code 19 and $R_c = 5/6$, but in the absence of multilevel coding, the spectral efficiency is reduced by one bit because of the code redundancy. The coding scheme MLC$(4,2)$, with WiMAX LDPC codes of various length and $R_c = 5/6$, allows to improve the spectral efficiency by

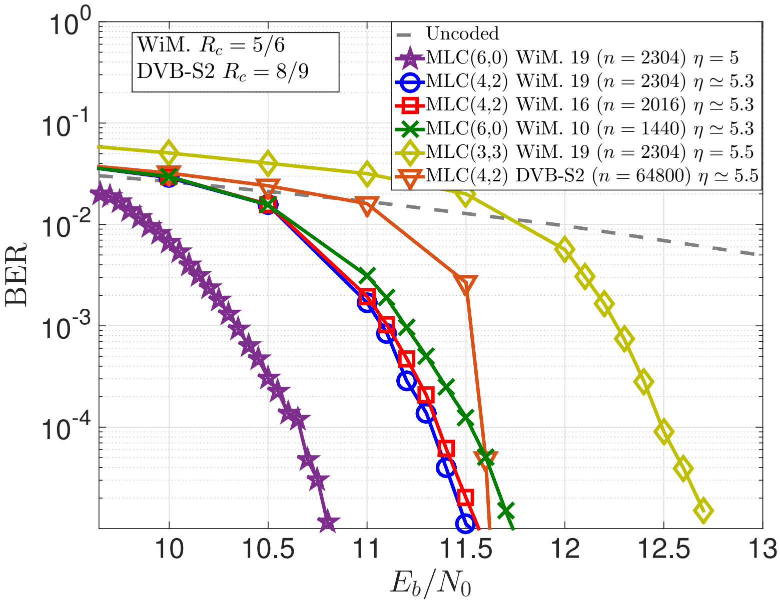

Figure 6.9: BER, as a function of E_b/N_0, for different LDPC codes and coding schemes.

Coding Scheme and code	64-QAM symb/codeword	Overall Latency [symbols]
MLC$(6,0)$ WiM. 19 ($n = 2304$)	384	768
MLC$(4,2)$ WiM. 19 ($n = 2304$)	576	1152
MLC$(4,2)$ WiM. 16 ($n = 2016$)	504	1008
MLC$(4,2)$ WiM. 10 ($n = 1440$)	360	720
MLC$(3,3)$ WiM. 19 ($n = 2304$)	768	1536
MLC$(6,0)$ DVB-S2 $n = 64800$	16200	32400

Table 6.2: Latency introduced in the systems for different LDPC codes and coding schemes.

about 0.3 bits per channel use at an energy cost of about 0.8 dB at BER $= 10^{-5}$. One can note that, clearly, codes with longer codeword length n perform better. The coding scheme MLC$(3,3)$ with code 19 and $R_c = 5/6$ allows the spectral efficiency to increase up to 5.5 bits per channel use, but the energy loss is more than 1.5 dB with respect to the scheme MLC$(4,2)$.

As a comparison with longer codes, we show the results obtained with the LDPC code used in Digital Video Broadcasting - Second Generation (DVB-S2) standard [68] with $R_c = 8/9$, which, for coding scheme MLC$(4,2)$, allows $\eta \simeq 5.5$. The DVB-S2 LDPC code outperforms the others, but the codeword is fixed to 64800 bits, meaning that the latency is very high. In particular, in Table 6.2 the latency introduced by the various schemes is shown, in terms of symbols per codeword. As mentioned in Section 6.3, the overall latency, due to the encoding and decoding process, is defined as the time needed to generate the frame of symbols of a codeword at the transmitter, plus the time needed to collect the same frame at the receiver. We consider an overall latency constraint of 2048 symbols, as it may be adequate for a high voltage PLC system of main interest in this work. One can observe that all of the considered schemes are compliant with the latency constraint, except for the case of the DVB-S2 code, which, because of the long codeword, introduces unacceptable latency.

We now discuss the ability of the proposed schemes to approach the channel

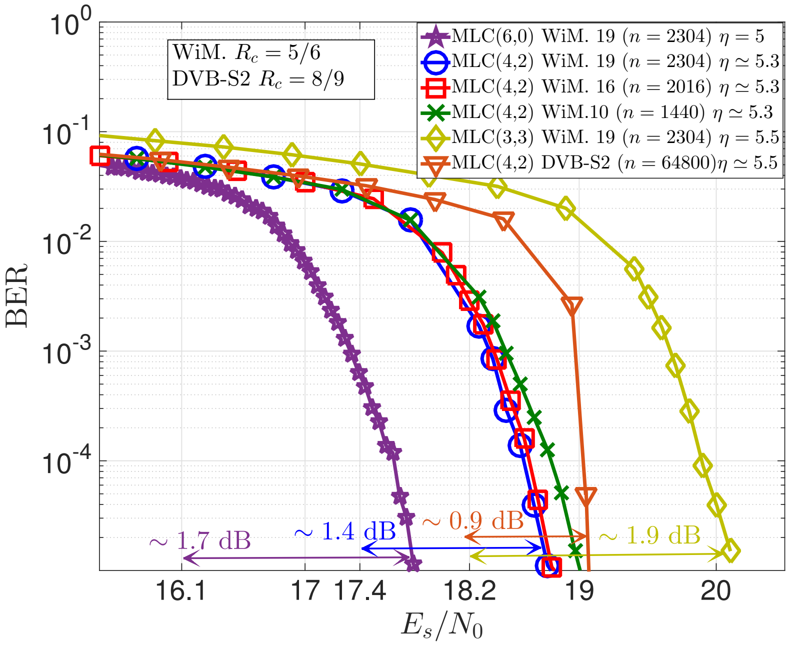

Figure 6.10: BER, as a function of E_s/N_0, for different codes and coding schemes. The distances from the channel capacity at BER $= 10^{-5}$ are highlighted.

capacity. Figure 6.10 shows the BER curves of Figure 6.9, as functions of the energy-per-symbol to noise ratio E_s/N_0, where

$$E_s = \eta E_b.$$

In the figure, it is highlighted the distance, at BER $= 10^{-5}$, from the channel capacity of 64-QAM. This is also shown in Figure 6.11, where the Information Rate (IR) [69] is drawn as a function of E_s/N_0, for 64-QAM transmission over AWGN channel.

One can see that MLC$(6,0)$ exhibits the worst performance in terms of both energy and spectral efficiencies, as $\eta = 5$ and the loss at BER $= 10^{-5}$, with respect to the capacity, is about 1.7 dB. Multilevel encoding allows a bet-

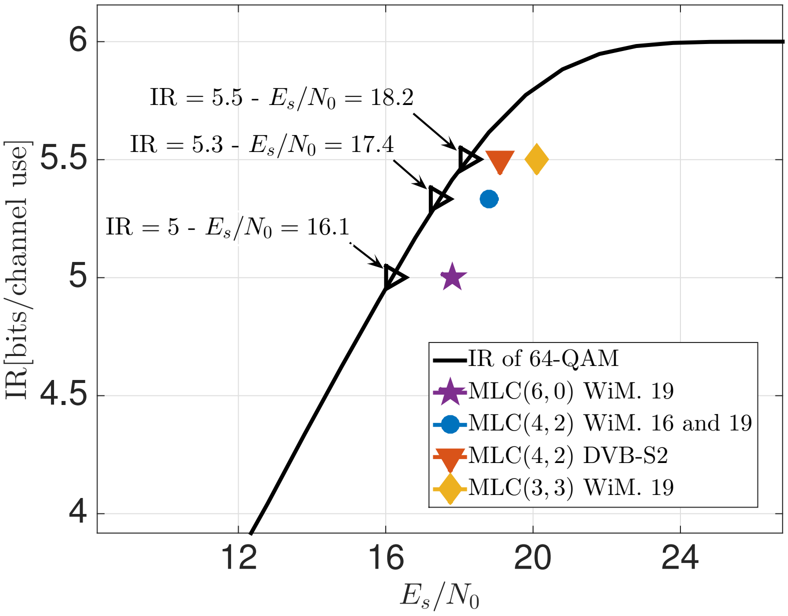

Figure 6.11: Information rate, as a function of E_s/N_0, for 64-QAM. The spectral efficiencies (6.4) and the values of E_s/N_0 at a BER of 10^{-5} for various schemes are highlighted.

ter performance: in particular, the best trade-off between spectral and energy efficiency is obtained with MLC$(4,2)$ and WiMAX LDPC 19, which exhibits a loss of about 1.4 dB, with respect to the capacity, at BER $= 10^{-5}$, supporting $\eta \simeq 5.3$. The scheme MLC$(3,3)$ allows the best spectral efficiency $\eta = 5.5$, but exhibits a loss of about 1.9 dB. One can see that MLC$(4,2)$ with DVB-S2 LDPC and $R_c = 8/9$ reduces the loss to about 0.9 dB, but, as discussed before, the introduced latency is unacceptable. Moreover, we recall that the comparison is not really fair, as the code length is much longer than that of WiMAX LDPC codes.

6.4.2 Impulse Noise Channel

We now consider the presence of impulse noise on the physical channel, as described in Section 1.3. According to the general model shown in Figure 6.1, in this case the received observable is $r_k = x_k + i_k$, in which the impulse noise sequence $\{i_k\}$ is composed by samples of Gaussian random variables, with zero mean and variance depending on the channel state.

In order to mitigate the impulse noise effects on the decoding process, we consider the presence of an amplitude clipper, with threshold L, at the receiver [70]. So that, denoting as r'_k the clipped received signal, one has

$$r'_k = \begin{cases} r_k & \text{if } |r_k| \leq L \\ L\dfrac{r_k}{|r_k|} & \text{if } |r_k| > L. \end{cases}$$

In Figure 6.12, the BER is shown as a function of E_b/N_0, for the coding schemes MLC$(6,0)$ and MLC$(4,2)$ with the WiMAX LDPC code 19 and $R_c = 5/6$, with $R = 10, 100$, $P_i = 10^{-4}$, and $\gamma = 10$. Note that this choice of P_i, for the sample case of the scheme MLC$(4,2)$, in which a codeword is composed of 576 64-QAM symbols, models an average occurrence of one impulsive event approximately every 20 transmitted codewords. The value of L is set to 1.8 by trial and error, with respect to the signal normalized with mean square value equal to 1. One can see that, for the scheme MLC$(4,2)$, the presence

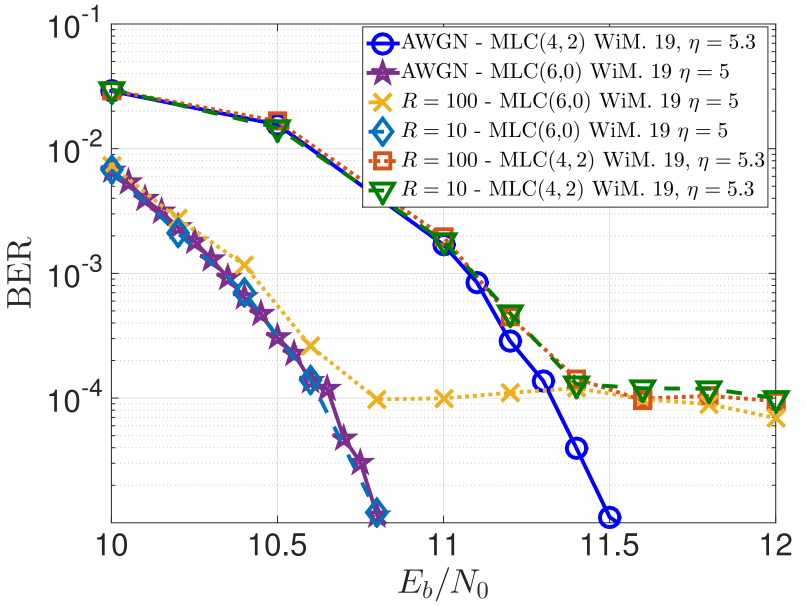

Figure 6.12: BER, as a function of E_b/N_0, for the coding schemes MLC$(6, 0)$ and MLC$(4, 2)$ with the WiMAX LDPC code 19 and $R_c = 5/6$, and for $R = 10, 100$, $P_i = 10^{-4}$, and $\gamma = 10$.

of impulse noise causes an error floor at a BER about 10^{-4} for both $R = 10$ and 100. This demonstrates that, although the amplitude clipper activates less frequently in the case of $R = 10$, the impulsive events impact on the decoding of the free bits, not protected by the code. For the scheme MLC$(6, 0)$, instead, only strong bursts of noise ($R = 100$), degrade the performance, while for moderate impulses ($R = 10$) the coding scheme performs as in the AWGN case.

6.5 Conclusions

We analyzed the performance of LDPC coded modulation schemes based on multilevel coding techniques. We used the IEEE 802.16e standard LDPC codes, motivating our choice with their capability to achieve high spectral efficiency with low latency on the encoding/decoding process. Our results show that the proposed schemes allow a good trade-off between spectral and energy efficiencies, remaining compliant with a typical PLC scenario latency constraint. We investigated the performance of the proposed coding schemes also in the presence of impulse noise.

Conclusions and Future Works

In this dissertation, the design of a PLC modem has been investigated, with particular attention on the echo canceller device and the channel coding scheme. A general model of a full-duplex PLC communication system has been reviewed, introducing realistic features, provided by Selta. In order to characterize the PLC channel, we have introduced the impulse noise, typical in this scenario, modeling it by bursty impulse noise model. This choice is related to the fact that the impulsive events on the power line are not memoryless, so that a better characterization of the impulse noise can be achieved by this model.

We have discussed the implementation of the LMS algorithm for the echo cancellation in a single-carrier PLC modem and reviewed some of its variants. We have derived the LMS cost function, the MSE, for the considered scenario of the baseband echo cancellation at sampling frequency. We have presented a performance analysis, based on the MSE and the SER, showing that the AWGN, as well as the impulse noise, do not affect the echo canceller adaptation process and that the suitable length of the adaptive filter is the length of the echo channel impulse response itself.

We have extended the analysis to a multi-carrier PLC modem, reviewing the time-domain echo cancellation and comparing its performance with that of the single-carrier one. The analysis has shown that the echo cancellation can be performed in the same manner for both systems.

A fixed-point version of the LMS algorithm has been investigated, to analyze its behavior for a real-world implementation. The MSE analysis has highlighted that a poor representation of the fixed-point numbers, i.e., a small wordlength, impacts the LMS convergence performance, causing the stop of the adaptation process. We have analyzed the problem, proposing some modifications of the classical LMS algorithm to cope with the *stopping phenomenon* in the case of reduced wordlength. While for the single-carrier system a 16 bits wordlength may be sufficient for the fixed-point representations, in the case of the multi-carrier system, 24 bits are required, because of the increased signal dynamics.

We have observed that abrupt echo channel variations, occurring, for example, during maintenance operations, may impact the reliability of the communication. For this reason we have further investigated the convergence performance of the LMS algorithm when the channel conditions abruptly vary. The analysis has led to the formulation of an LMS-based modified algorithm, the WRL algorithm, based on the sudden detection of the channel variations and a suitable reinitialization of the adaptive filter weights. The algorithm proved effective in reducing the convergence period. The extension of the proposed strategy to the VSLMS algorithm (suitable for scenarios in which a fast recovery from abrupt channel variations is required) and its effectiveness, proved that the weight reset strategy may be applied to various scenarios and a number of LMS-based algorithms, as well.

Innovative coding schemes, possibly suitable for PLC systems, have been analyzed, in order to handle the requirement of high spectral efficiency and low encoding/decoding latency. We have proposed different coding schemes, based on multilevel coding techniques, adopting the short and effective LDPC codes of the WiMAX standard. The multilevel coding schemes have proven to be compliant with the latency requirement considered and effective in achieving high-spectral efficiencies.

The research activity described in this thesis may be further deepen. Although, the formulation of the WRL algorithm has been refined during the PhD research activity and is suitable for most scenarios, many possibilities for performance improvement and complexity reduction can be investigated. In particular, it is possible to apply the weight reset to a selected section of the weight vector, aiming to reduce the computational complexity of the algorithm, related to the length of the weight vector. Also, information about the new vector position, after the channel conditions variation, may be suddenly retrieved from the observation of the weight vector energy.

For what concerns the research activity on the channel coding schemes, currently an interesting alternative to LDPC codes appears to be the polar codes [71, 72, 73]. In particular, this class of codes, which exploit of the so-called polarization of the channel, may be suitable for multilevel coding implementation, as discussed in [74, 75], and represent an attractive future research field.

Bibliography

[1] H. Ferreira, L. Lampe, J. Newbury, and T. Swart, *Power Line Communications: Theory and Applications for Narrowband and Broadband Communications over Power Lines.* John Wiley & Sons; New York, NY, USA, 2010.

[2] X. Fang, S. Misra, G. Xue, and D. Yang, "Smart grid: The new and improved power grid: A survey," *IEEE Communications Surveys & Tutorials*, vol. 14, no. 4, pp. 944–980, December 2012.

[3] W. Xu and W. Wang, "Power electronic signaling technology: A new class of power electronics applications," *IEEE Trans. Smart Grid*, vol. 1, no. 3, pp. 332–339, September 2010.

[4] A. V. Oppenheim, R. W. Schafer, J. R. Buck *et al.*, *Discrete-time signal processing.* Prentice-Hall, 1999.

[5] E. C. Ifeachor and B. W. Jervis, *Digital Signal Processing: a Practical Approach.* Pearson Education, 2002.

[6] A. B. Carlson, *Communication Systems: An Introduction to Signals and Noise in Electrical Communication.* McGraw-Hill, 1986.

[7] J. Carr, S. Winder, and S. Bigelow, *Understanding Telephone Electronics.* Elsevier Science Publishers; Amsterdam, Netherlands, 2001.

[8] L. W. Couch, M. Kulkarni, and U. S. Acharya, *Digital and Analog Communication Systems.* Prentice-Hall, 1997, vol. 6.

[9] R. Barry, E. A. Lee, and D. G. Messerschmitt, *Digital Communications.* Springer, 2004.

[10] M. Zimmermann and K. Dostert, “Analysis and modeling of impulsive noise in broad-band powerline communications,” *IEEE Trans. Electron. Compatib.*, vol. 44, no. 1, pp. 249–258, February 2002.

[11] M. Ghosh, “Analysis of the effect of impulse noise on multicarrier and single carrier QAM systems,” *IEEE Trans. Commun.*, vol. 44, no. 2, pp. 145–147, February 1996.

[12] R. Pighi, M. Franceschini, G. Ferrari, and R. Raheli, “Fundamental performance limits of communications systems impaired by impulse noise,” *IEEE Trans. Commun.*, vol. 57, no. 1, pp. 171–182, January 2009.

[13] D. Middleton, “Statistical-physical models of electromagnetic interference,” *IEEE Trans. Electron. Compatib.*, vol. 19, no. 3, pp. 106–127, August 1977.

[14] D. Fertonani and G. Colavolpe, “On reliable communications over channels impaired by bursty impulse noise,” *IEEE Trans. Commun.*, vol. 57, no. 7, pp. 2024–2030, July 2009.

[15] M. Mushkin and I. Bar-David, “Capacity and coding for the Gilbert-Elliott channels,” *IEEE Trans. Inform. Theory*, vol. 35, no. 6, pp. 1277–1290, November 1989.

[16] A. Papoulis and S. U. Pillai, *Probability, Random Variables, and Stochastic Processes.* McGraw-Hill; New York, 2002.

[17] B. Widrow and S. D. Stearns, *Adaptive Signal Processing.* Prentice-Hall, 1985.

[18] R. Raheli and G. Colavolpe, *Trasmissione Numerica.* Monte Università Parma, 2004.

[19] B. Farhang-Boroujeny, *Adaptive filters: theory and applications.* John Wiley & Sons; New York, NY, USA, 1998.

[20] S. S. Haykin, B. Widrow, and J. Wiley, *Least-mean-square adaptive filters.* John Wiley & Sons; New York, NY, USA, 2003.

[21] S. Haykin, *Adaptive filter theory.* Prentice-Hall, 2000.

[22] N. Benvenuto and G. Cherubini, *Algorithms for Communications Systems and Their Applications.* John Wiley & Sons; New York, NY, USA, 2002.

[23] I. Homana, M. D. Topa, and B. S. Kirei, "Echo cancelling using adaptive algorithms," in *IEEE International Symposium for Design and Tech. of Elect. Pack.* (SIITME), September 2009, pp. 317–321.

[24] J. V. Lopez, J. C. Sanchez, and H. P. Meana, "Adaptive echo canceller using a modified LMS algorithm," in *IEEE International Conf. on Electrical and Electronics Engineering* (ICEEE), September 2005, pp. 93–96.

[25] A. Birkett and R. Goubran, "Acoustic echo cancellation using NLMS-neural network structures," in *IEEE International Conf. on Acoustics, Speech, and Signal Proc.* (ICASSP), vol. 5, May 1995, pp. 3035–3038.

[26] M. Hutson, "Acoustic echo cancellation using digital signal processing," Master's thesis, School of Information Technology and Electrical Engineering, University of Queensland, November 2003.

[27] B. Widrow, J. McCool, and M. Ball, "The complex LMS algorithm," *Proc. IEEE*, vol. 63, no. 4, pp. 719–720, April 1975.

[28] D. T. Slock, "On the convergence behavior of the LMS and the normalized LMS algorithms," *IEEE Signal Processing Letters*, vol. 41, no. 9, pp. 2811–2825, September 1993.

[29] S. C. Douglas, "A family of normalized LMS algorithms," *IEEE Signal Processing Letters*, vol. 1, no. 3, pp. 49–51, March 1994.

[30] J. M. Cioffi, "A multicarrier primer," *Amati Communications Corporation and Standford University*, vol. 4, pp. 91–157, 1991.

[31] S. Weinstein and P. Ebert, "Data transmission by frequency-division multiplexing using the discrete Fourier transform," *IEEE Trans. on Comm. Tech.*, vol. 19, no. 5, pp. 628–634, October 1971.

[32] B. Hirosaki, "An orthogonally multiplexed QAM system using the discrete Fourier transform," *IEEE Trans. Commun.*, vol. 29, no. 7, pp. 982–989, July 1981.

[33] A. R. Bahai, B. R. Saltzberg, and M. Ergen, *Multi-carrier Digital Communications: Theory and Applications of OFDM.* Springer, 2004.

[34] M. Hoch, "Comparison of PLC G3 and PRIME," in *IEEE Intern. Symp. Power Line Commun. and its App.* (ISPLC), April 2011, pp. 165–169.

[35] Y. Ma, P. So, and E. Gunawan, "Performance analysis of OFDM systems for broadband power line communications under impulsive noise and multipath effects," *IEEE Trans. Power Deliv.*, vol. 20, no. 2, pp. 674–682, April 2005.

[36] H. Meng, Y. Guan, and S. Chen, "Modeling and analysis of noise effects on broadband power-line communications," *IEEE Trans. Power Deliv.*, vol. 20, no. 2, pp. 630–637, April 2005.

[37] J. Cioffi and J. Bingham, "A data-driven multitone echo canceller," *IEEE Trans. Commun.*, vol. 42, no. 10, pp. 2853–2869, Oct 1994.

[38] D. Jones, "Frequency domain echo cancellation for discrete multitone asymmetric digital subscriber line transceivers," *IEEE Trans. Commun.*, vol. 43, no. 2/3/4, pp. 1663–1672, 1995.

[39] H. Bogucka and K. Wesolowski, "Frequency-domain echo cancellation in digital multicarrier modulation systems," *IEEE Trans. Commun.*, vol. 48, no. 2, pp. 333–342, February 2000.

[40] J.-F. Marceau and B. Champagne, "A reduced complexity multi-rate echo canceller for DMT based DSL systems," in *Proc. Canadian Conf. on Elec. and Comp. Eng.*, May 2005, pp. 1202–1207.

[41] N. Ehtiati and B. Champagne, "A general framework for mixed-domain echo cancellation in discrete multitone systems," *IEEE Trans. Commun.*, vol. 61, no. 2, pp. 769–780, February 2013.

[42] A. Bateman and I. Paterson-Stephens, *The DSP Handbook.* Prentice-Hall, 2002.

[43] R. Yates, "Fixed-point arithmetic: An introduction," Digital Signal Labs, Tech. Rep., January 2013. [Online]. Available: http://www.digitalsignallabs.com/fp.pdf

[44] D. Menard, D. Chillet, and O. Sentieys, "Floating to fixed point conversion for digital signal processors," *EURASIP J. Applied Signal Processing*, vol. 2006, pp. 1–19, July 2006.

[45] C. Marven and G. Ewers, *A simple approach to digital signal processing.* Texas Instruments, 1993.

[46] F. Pancaldi and G. M. Vitetta, "Una guida all' implementazione di algoritmi di elaborazione numerica del segnale su schede EVM TMS320C6201," University of Modena and Reggio Emilia - Department of Information Engineering, Tech. Rep., June 2005. [Online]. Available: www.ict.unimore.it/ict_docs/phd_topics/2003/pancaldi.doc

[47] R. Yates, "Practical considerations in fixed-point FIR filter implementation," Digital Signal Labs, Tech. Rep., September 2010. [Online]. Available: http://www.digitalsignallabs.com/fir.pdf

[48] R. D. Gitlin, J. Mazo, and M. Taylor, "On the design of gradient algorithms for digitally implemented adaptive filters," *IEEE Trans. Circ. Theory*, vol. 20, no. 2, pp. 125–136, March 1973.

[49] N. J. Bershad and J. C. M. Bermudez, "New insights on the transient and steady-state behavior of the quantized LMS algorithm," *IEEE Trans. Signal Processing*, vol. 44, no. 10, pp. 2623–2625, October 1996.

[50] B. Kaehs, "The crest factor in DVB-T (OFDM) transmitter systems and its influence on the dimensioning of power components," Rohde and Schwarz, Application Note 7TS02, Tech. Rep., January 2007.

[51] P. A. J. Van Rensburg and H. C. Ferreira, "Design and evaluation of a dual impedance-adapting power-line communications coupler," *IEEE Trans. Power Deliv.*, vol. 25, no. 2, pp. 667–673, October 2010.

[52] C. Tripodi, G. Ferrari, R. Pighi, and R. Raheli, "Echo cancellation in a power line modem in the presence of abrupt channel variations," in *IEEE Intern. Symp. Power Line Commun. and its App.* (ISPLC), Glasgow, Scotland, March 2014, pp. 208–213.

[53] C. R. Hadlock, *Field Theory and its Classical Problems.* Cambridge University Press; Cambridge, UK, 2000.

[54] W.-P. Ang and B. Farhang-Boroujeny, "A new class of gradient adaptive step-size LMS algorithms," *IEEE Trans. Signal Processing*, vol. 49, no. 4, pp. 805–810, April 2001.

[55] L. Lindbom, J. Rutstrom, A. Ahlén, and M. Sternad, "Automatic tuning of the step size in WLMS algorithms: Applications to EDGE," in *IEEE Vehicular Tech. Conf.* (VTC), Birmingham, AL, USA, May 2002, pp. 2229–2233.

[56] R. G. Gallager, "Low density parity check codes," *IEEE Trans. Inform. Theory*, vol. 8, no. 1, pp. 21–28, 1962.

[57] M. Franceschini, G. Ferrari, and R. Raheli, *LDPC Coded Modulations.* Springer-Verlag, 2009.

[58] N. Andreadou, C. Assimakopoulos, and F.-N. Pavlidou, "Performance evaluation of LDPC codes on PLC channel compared to other coding schemes," in *IEEE Intern. Symp. Power Line Commun. and its App.* (ISPLC), March 2007, pp. 296–301.

[59] Q. Zhang, F. Yang, J. Song, B. Zhao, and L. Geng, "An effective H-ARQ scheme for LDPC-coded broadband power line communication system," in *IEEE Intern. Symp. Power Line Commun. and its App.* (ISPLC), March 2012, pp. 165–169.

[60] T. Wada, "A study on performance of LDPC codes on power line communications," in *Proc. IEEE International Conf. on Commun.* (ICC), vol. 1, June 2004, pp. 109–113.

[61] "Approved draft IEEE standard for local and metropolitan area networks corrigendum to IEEE standard for local and metropolitan area networks-part 16: Air interface for fixed broadband wireless access systems (incorporated into IEEE Std 802.16e-2005 and IEEE Std 802.16-2004/Cor 1-2005 E)," 2005, Par. 8.4.9.2.5 Annex H pp. 626–630.

[62] S. Gupta and B. Virmani, "LDPC for Wi-Fi and WiMAX technologies," in *Proc. Emerging Trends in Electronic and Photonic Devices Systems*, December 2009, pp. 262–265.

[63] J. Zhang and M. Fossorier, "Shuffled iterative decoding," *IEEE Trans. Commun.*, vol. 53, no. 2, pp. 209–213, February 2005.

[64] G. Falcao, V. Silva, J. Marinho, and L. Sousa, "LDPC decoders for the WiMAX (IEEE 802.16e) based in multicore architectures," 2009. [Online]. Available: www.intechopen.com

[65] U. Wachsmann, R. Fischer, and J. Huber, “Multilevel codes: theoretical concepts and practical design rules,” *IEEE Trans. Inform. Theory*, vol. 45, no. 5, pp. 1361–1391, Jul 1999.

[66] G. Ungerboeck, “Channel coding with multilevel/phase signals,” *IEEE Trans. Inform. Theory*, vol. 28, no. 1, pp. 55–67, January 1982.

[67] J. Proakis and M. Saledi, *Digital Communications.* McGraw-Hill, 2007.

[68] “Digital Video Broadcasting (DVB); Second generation framing structure, channel coding and modulation systems for Broadcasting, Interactive Services, News Gathering and other broadband satellite applications; Part 1: DVB-S2,” pp. 24–25, 2014, Par. 5.3.2.

[69] T. Cover and J. Thomas, *Elements of Information Theory.* John Wiley & Sons; New York, NY, USA, 2006.

[70] G. Ndo, P. Siohan, and M. Hamon, “Adaptive noise mitigation in impulsive environment: Application to power-line communications,” *IEEE Trans. Power Deliv.*, vol. 25, no. 2, pp. 647–656, April 2010.

[71] E. Arikan, “Channel polarization: A method for constructing capacity-achieving codes for symmetric binary-input memoryless channels,” *IEEE Trans. Inform. Theory*, vol. 55, no. 7, pp. 3051–3073, July 2009.

[72] I. Tal and A. Vardy, “How to construct polar codes,” *IEEE Trans. Inform. Theory*, vol. 59, no. 10, pp. 6562–6582, October 2013.

[73] ——, “List decoding of polar codes,” *IEEE Trans. Inform. Theory*, vol. 61, no. 5, pp. 2213–2226, May 2015.

[74] P. Trifonov, “Efficient design and decoding of polar codes,” *IEEE Trans. Commun.*, vol. 60, no. 11, pp. 3221–3227, November 2012.

[75] M. Seidl, A. Schenk, C. Stierstorfer, and J. Huber, “Multilevel polar-coded modulation,” in *Proc. IEEE Symposium on Information Theory* (ISIT), July 2013, pp. 1302–1306.

Acknowledgments

I wish to express my sincere thanks to my mentor, Prof. Riccardo Raheli, whose invaluable guidance and immense knowledge have supported me, making this research work successful. Every day, during this PhD course, I have learnt something precious from him.

I would like to thank my tireless tutor, Prof. Gianluigi Ferrari, for his constant encouragement and friendly willingness. His expertise and insightful suggestions have been essential for this research activity.

My deep gratitude goes also to Selta S.p.A., which has funded these research years, giving me the possibility to accomplish the PhD degree. In particular, I wish to thank the PLC & Special Product Manger, Riccardo Pighi, PhD, his valuable competence, passion and dedication have always been inspiring for me.